Convection in planetary atmospheres: Titan's haze, Saturn's storm and Jupiter's water

Thesis by

Cheng Li

In Partial Fulfillment of the Requirements for

the Degree of

Doctor of Philosophy

CALIFORNIA INSTITUTE OF TECHNOLOGY

Pasadena, California

2017

(Defended May 23, 2016)

Cheng Li
ORCID: 0000-0002-8280-3119

Acknowledgements

Studying planetary science at Caltech for five years has been a remarkable experience to me. It expanded my horizon from the Earth to the whole Solar system. Many people have helped and supported me in the course of my graduate study.

First of all, I own the most sincere gratitude to my thesis advisor, Andy Ingersoll. This thesis is not possible without Andy's unconditionally support. I thank Andy for showing me how to understand complicated phenomena in a simple way that can be explained to high school students. He led me by the hand through the maze of dynamics. I thank Andy for encouraging me to pursue my interest but still reminding me of "not reinventing the wheel". I enjoy every Thanksgiving dinner I had with Andy's family. Andy is not only an advisor to me but also a friend whom I can talk about anything with.

Andy is a friend and Yuk Yung is a parent. Yuk stepped into the career path of all Chinese students and supported them in various aspects. I'm grateful to be in Yuk's army for one and a half years and I cherish all Monday Cassini meetings, Tuesday Yuk lunch seminars, Wednesday group meetings and Sunday meetings.

I had a conversation with Heather Knutson in the second year after my Ph.D. qualification exam. She told me not to focus on publishing numerous papers during graduate school, but to have my tools ready by the time of graduation. I thank for her incisive advice and I'm working on the pathway that Heather pointed out.

Earth is the planet with the greatest plethora of observations. I thank Simona Bordoni for her classes and reading groups that expanded my horizons concerning the Earth's hydrological cycle and climate. Simona taught me the very basics about atmospheric dynamics and thermodynamics, which are the theoretical foundations of my research.

I also want to thank Dave Stevenson, Geoffrey Black, Andy Thompson, Paul Wennberg, Tapio Schneider, Rob Clayton, Mike Gurnis, John Eiler, Paul Asimow for their classes and Mike Janssen for introducing me to the Juno project.

I am fortunate to be surrounded by the brilliant officemates. I had a good time talking with Mike Line about retrievals, with Aaron Wolf about statistics, with Alejandro Soto about GCMs, with Miki Nakajima about silicate vapor, with Zhan Su about salt in the ocean, with Pushkar Kopparla about Saturn's hexagon, with Mike Wong about the other Mike Wong in Berkeley and looking at Danielle Piskorz's mug changing from "MIT is cooler" to "Caltech is hotter".

I appreciate all the support from the planetary science option staff. Margaret Carlos and Irma Black welcomed me from my first day at Caltech and constantly provide me with financial support from travel reimbursement. I thank Mike Black for his immediate response to any question regarding "snowy". I thank Shawn Ewald for every conversations we have about Formula 1, Starcraft, the history of astronomy file formats and SPICE. They are very entertaining. I thank Run-lie Shia for treating me several times at Shanghai No. 1.

My life at Caltech won't be easy without the warm company of my friends. I thank Qiong Zhang for all joyful moments we spent starting from Peking University and all the rides from

and to LAX. I thank Da Yang for the conversation about tropical meteorology. I thank Lu Pan and Wen Chen for sharing the stories in the community as well as good restaurants. I thank Peter Gao and Henry Ngo for staying till 2 am in the morning at South Mudd. I thank Cong Wang for always saving half an orange for me. I thank Hank Yu, Jinqiang Chen, Hao Zhang and Tobias Bischoff for fighting qualify exams together; Boyu Li, Jionghui Li, Wentao Huang, Qiuyu Peng, Yang liu for dining at the Valley boulevard; Wen Yan and Caili Shen for being my roommates and washing the dinner plates; Lei Fu for playing games; Daodi Lu for showing how to correctly fill a Mongolian noodle bowl and Du Pei for his deepest insight into string theory.

I appreciate the moments that I spent with friends outside of California. I thank Shuo Wang and Fang Fang for organizing the trip to Alaska and South Dakota, and Xin Nin for sending the postcard of Mt. Rushmore. I thank all members in the Whitney Training Camp, Dezhou Guo, Yinglu Tang, Wei Mao, Sijia Dong, Jun Chen for the triumph we achieved. I thank Wendian Shi, Wendy Chen and Butter for the wonderful night watching meteor showing (Wendy's father taught me how to make sushi that day). I thank Yuan Lin for all postcards she sent to me and I thank Lucy Yin, Hao Wu. Zhimeng Zhang, Laixin Wei. They made my life colorful.

Special thanks should be expressed to Xi Zhang and Zhihong Tan. Xi Zhang is true to the name of "spiritual leader" in Yuk's army. He has such an aura that clears all difficulties in both science and life. I always went into Xi's office with tons of questions and went out with thousands of solutions. I enjoy all conversations with Zhihong Tan about clouds, models, musics, hikings and travels. Zhihong introduced me the beauty of hiking and from then on,

my life becomes different. Zhihong also informed me on the theory of moist convection on Earth, which allows me to brainstorm what should be on Jupiter.

I would like to thank my former schoolmates, Zhiyuan Lin and Longfei Jiao for the happinesses and sorrows in the department of physics, though we are now thousands of miles away. I would also like to thank my undergraduate adviser, Yongyun Hu. He enlightened me on science.

Finally, I devote my thesis to my parents, Xiuyong Li and Fengxian Li for raising and nurturing me. Their endless love and dedication shaped me into what I am today. Last, but not least, I am indebted to Zhiying Hu. We met each other in my sophomore year and we have spent lovely times in Peking University. In science, she helped to proofread all my manuscripts and pointed out typos and errors. In daily life, we spent numerous weekends watching TV series together. I feel honored to have her with me all the time even though we were apart after I chose to pursue a higher degree at Caltech. It is her love that makes my thesis possible.

Abstract

Atmospheric convection is a profound topic. Numerous books have been written on the consequences of convection. Yet, the picture of convection is still far from complete because of its high nonlinearity, multi-scale coupling and complex interactions with other systems. The theme of my dissertation is to investigate three aspects of atmospheric convection on three different planets. This dissertation is multi-disciplinary and includes scientific topics like photochemistry, dynamics and radiation, and methodologies like information retrieval, theoretical calculation and dynamic modeling.

Chapter 1 and 2 study Titan. It focuses on how to infer the strength of convection from the vertical distribution of chemical species. In a photochemical model, convection is parameterized as eddy diffusion and the strength of convection is proportional to eddy diffusivity. We developed an inversion method to retrieve the vertical profile of eddy diffusivity directly from the Cassini observations and found out a stable layer in the atmosphere which may give rise to the detached haze layer on Titan. In addition, new observation from Cassini/CIRS limb sounding came a few month later. C_3H_6 was detected for the first time in the stratosphere. Our new photochemical model with the updated eddy diffusion profile successfully explained the observed vertical distribution of C_3H_6. Chapter 2 explains the modeling result and does a systematic study on all C_3-hydrocarbons.

Chapter 3 studies Saturn. It investigates the role of convection on regulating Saturn's giant storms. Six giant storms, called Great White Spots, have erupted on Saturn since 1876 at intervals of about 30 years. The most recent one occurred on Dec. 5th, 2010 at planetographic latitude 37.7^{o}N. It produced intense lightning, created enormous cloud disturbances and wrapped around the planet in 6 months. We proposed the water-loading mechanism to explain the periodicity. Moist convection is suppressed for decades due to the larger molecular weight of water in a hydrogen-helium atmosphere. We show that this mechanism requires the deep water vapor mixing ratio to be greater than 1.0%, which implies Saturn's O/H to be at least 10 times the solar value.

Chapter 4 studies Jupiter. It proposes an inversion strategy for the upcoming Juno microwave observation based on the modeling results and the theoretical arguments developed in Chapter 3. We extend the Juno/MWR's functionality by retrieving both the deep water mixing ratio and a few dynamic parameters representing subcloud meteorology. This proposition will contribute substantially to achieving the Juno/MWR objectives and shed light on the functioning of convection on planets with deep atmospheres.

PUBLISHED CONTENT AND CONTRIBUTIONS

Li, Cheng, A. P. Ingersoll, 2015. Moist convection in hydrogen atmospheres and the frequency of Saturn's giant storms, *Nature Geoscience, 8, 398-403.*

Both authors participated in the conception of the project and analysis of the data. C.L. wrote the numerical model in the project.

Li, Cheng, X. Zhang, P. Gao, Y. L. Yung, 2015. Vertical distribution of C_3-hydrocarbons in the stratosphere of Titan, *Astrophysical Journal Letters, 803, L19.*

C.L. and Y.L.Y. participated in the conception of the project. X.Z. made significant suggestions. P.G. helped diagnose the computer program. C.L. wrote the numerical model.

Li, Cheng, X. Zhang, et al., 2014. A non-monotonic eddy diffusivity profile of Titan's atmosphere revealed by Cassini observations. *Planetary and Space Science*, 104, Part A(0), 48-58.

C.L. and Y.L.Y. participated in the conception of the project. X.Z. provided the calculation of aerosol absorption. J.A.K provided UVIS data. M.C.L. wrote the first version of Titan’s photochemical model. C.L. modified the model. R.L.S. made useful suggestions and helped diagnose the model.

TABLE OF CONTENTS

TABLE OF FIGURES

Chapter 1 A non-monotonic eddy diffusivity profile of Titan's atmosphere revealed by Cassini observations

Cheng Li[1], Xi Zhang[1], Joshua A. Kammer[1], Mao-Chang Liang[2,3], Run-lie Shia[1], Yuk L. Yung[1]

[1]Division of Geological and Planetary Science, California Institute of Technology, Pasadena, CA, 91125

[2]Research Center for Environmental Changes, Academia Sinica, Taipei, Taiwan

[3]Graduate Institute of Astronomy, National Central University, Zhongli, Taiwan

Published in modified form in *Planetary and Space Science*, 104, Part A(0), 48-58, 2014

1.1 Abstract

Recent measurements from the limb-view soundings of Cassini/CIRS and the stellar occultations from Cassini/UVIS revealed the complete vertical profiles of minor species (e.g. C_2H_2 and C_2H_4) from 100 to 1000 km in the atmosphere of Titan. In this study, we developed an inversion technique to retrieve the eddy diffusion profile using as a tracer species. The retrieved eddy profile features a low eddy diffusion zone near the altitude of the detached haze layer (~550 km), which could be a consequence of stabilization through aerosol heating. Photochemical modeling results using the retrieved eddy profile are in better agreement with the Cassini measurements than previous models. The underestimation of C_2H_4 in the stratosphere has been a long-standing problem in planetary photochemical modeling, and the new eddy diffusion profile does not solve this problem. In order to match the observations, we suggest a new expression for the rate coefficient of the key reaction, $H + C_2H_4 + M \rightarrow C_2H_5 + M$. The new reaction rate coefficient is estimated to be ~10 times lower than that used by Moses et al. (2005b)'s model, and should be validated in the laboratory and tested against the hydrocarbon chemistry of giant planets.

Key words: Titan photochemistry, Eddy diffusion profile, Chemical kinetics

1.2 Introduction

In one-dimensional photochemical models, the vertical transport of a species is often parameterized as a diffusion process. The diffusion coefficient, referred to as K_{zz} or eddy diffusivity, incorporates various scales of turbulent processes arising from nonlinear wave breaking and instabilities. Many empirical studies have estimated this parameter from the amplitude of gravity waves (Strobel, 1974). Lindzen (1981) first theoretically concluded that the eddy diffusivity was proportional to the inverse square root of background atmospheric density and his finding served as a basis for the estimation of eddy diffusion in early photochemical models (Yung et al., 1984). The macroscopic eddy mixing resulting from dynamical instabilities is much more difficult to characterize. Two primary sources of these instabilities are convective instability and shear instability. The stability parameter is the Richardson number:

$$Ri = \frac{N^2}{(\frac{\partial U}{\partial z})^2 + (\frac{\partial V}{\partial z})^2}, \tag{1.1}$$

where N^2 is the square of the Brunt-Väisälä frequency; U, V are the mean zonal and meridional winds respectively. The atmosphere is subject to convective instability if *Ri* is negative and is subject to mechanically driven turbulent flow if *Ri* is positive but less than 0.25 (Taylor, 1931). Detailed calculation of eddy diffusivities relies on sophisticated dynamical models, such as the large-eddy simulation (LES) model, and high-order closure formulations of turbulent kinetic energy (TKE), which have been elaborated in boundary layer meteorology (Stull, 1988; Wyngaard, 1992). More practical ways to estimate the eddy diffusivity are based on observations. For example, oceanographers usually inject non-

reactive tracers into the ocean and observe their evolution. Fitting the spreading of the tracer to a diffusive equation measures the eddy diffusivity.

In photochemical modeling of planetary atmospheres, such experiments are difficult to implement and high-resolution dynamical modeling coupled with chemical sources and sinks has not yet matured. Instead, modelers adopt the eddy diffusivity required to fit the measured abundance of a species whose vertical structure is controlled primarily by transport. This empirical approach not only facilitates the modeling of vertical transport but sheds light on unknown dynamical processes as well. For instance, Allen et al. (1981) found that a sudden decrease of eddy diffusivity at 92 km in Earth's mesosphere was required to produce the atomic oxygen peak. This hypothesis was later confirmed and explained by the theory of breakdown of gravity waves (Lindzen, 1981).

A significant number of photochemical models has been developed to investigate the distribution of hydrocarbons in Titan's atmosphere (Krasnopolsky, 2009; Krasnopolsky, 2010; Lara et al., 1996; Lavvas et al., 2008a; Lavvas et al., 2008b; Wilson and Atreya, 2004; Yung, 1987; Yung et al., 1984). It has been accepted wisdom that the eddy diffusivity increases monotonically from the stratosphere to the thermosphere. Though this argument is rooted in the monotonic growth of the amplitude of gravity waves, it ignores the eddy mixing resulting from convective and shear instabilities, which depend on local properties whose strength is not guaranteed to behave monotonically with respect to altitude. In fact, Titan's atmosphere exhibits strong thermal variations and wind shear. At several altitudes,

the temperature lapse rate exceeds the adiabatic lapse rate (Fulchignoni et al., 2005). Therefore, it is entirely possible that the eddy diffusivity could reach a maximum (minimum) in the interior when the lapse rate is largest (smallest) or when the wind shear is strongest (weakest).

In this work, we explore the possibility of a non-monotonic eddy diffusion profile. We develop an inversion technique that uses C_2H_2 as the tracer species for inverting the required eddy diffusion profile that agrees with the latest Cassini/CIRS, Cassini/UVIS and Cassini/INMS observations. We also discuss the revision of the rate coefficients for the chemistry of hydrocarbons given the retrieved eddy diffusion profile.

In section 1.3, we describe the strategy for choosing an appropriate tracer species. In section 1.4, we provide the inversion techniques and compare the modeling result using the retrieved eddy profile with the observations. In section 1.5, we analyze the chemical pathways and propose updates for hydrocarbon chemistry. In the section 1.6, we discuss the role of escape and heterogeneous reactions that might affect our retrieval. We also discuss a possible mechanism that gives rise to the retrieved eddy profile.

1.3 Choice of tracer species

In the chemical modeling literature of Titan's atmosphere, the choice of tracer species progresses with the available observations. When Voyager (Coustenis et al., 1989) and ground-based millimeter observations (Tanguy et al., 1990) first detected HCN, its abundance was used to constrain the eddy diffusivity in the lower atmosphere (Lara et al., 1996; Toublanc et al., 1995), for HCN was thought to possess low reactivity with other species. After the arrival of Cassini spacecraft in 2005, subsequent measurements provided new constraints on the eddy diffusion profile. (Lavvas et al., 2008a; Lavvas et al., 2008b) constructed the first comprehensive photochemical model based on Cassini measurements. In their model, the eddy diffusion profile was adjusted to fit the abundance of C_2H_6 (Vinatier et al., 2007) and ^{40}Ar (Waite Jr et al., 2005). In addition, Yelle et al. (2008a) suggested an asymptotic expression for the eddy diffusion profile based on the thermospheric profile of ^{40}Ar, CH_4 (above 1000 km) and the stratospheric abundance of C_2H_6 ($100 \sim 300$ km). This eddy diffusion profile was then widely used in recent chemical models (Hörst et al., 2008; Krasnopolsky, 2009; Vuitton et al., 2008). However, the asymptotic expression relies on a free parameter γ, which is 0.9 in Yelle et al. (2008a) but 2.0 in the model of Krasnopolsky (2009, appendix), and the modeling results produced by different choices of γ were inconsistent with the observations for some important species (e.g., C_2H_2 in the model of Krasnopolsky, 2009; C_4H_2 in Vuitton et al., 2008). The discrepancies are likely caused by the unconstrained eddy diffusion profile in the mesosphere of Titan ($500 \sim 1000$ km). Changes in the altitude of the fall-off region in the asymptotic expression, determined by γ, could have a large impact on the modeling of hydrocarbons.

Recently, more constraints have been placed on the abundance of hydrocarbons in the mesosphere of Titan ($500 \sim 1000$ km) from Cassini/UVIS stellar occultations (Kammer et al., 2011; Koskinen et al., 2011). In combination with the updated version of Cassini/CIRS limb observation (Vinatier et al., 2010a), the complete profiles of C_2H_2, C_2H_4, C_6H_6, HCN, HC_3N are revealed for the first time.

Hydrocarbons in Titan's atmosphere react under extremely low pressures that are hard to reproduce in the laboratory. Aside from the eddy diffusivity, the major uncertainties of the photochemical modeling arise from the estimation of the reaction rate coefficient. We define a metric for a species that measures the sensitivity of its abundance to the uncertainties in reaction rate coefficients by:

$$s = \sum_{j=1}^{N_r} \sum_{i=1}^{N_v} \left(\frac{\Delta x_i}{x_i} \right)_j^2, \tag{1.2}$$

where N_r is the total number of reactions; N_v is the total number of vertical levels, and $\left(\frac{\Delta x_i}{x_i} \right)_j$ denotes the fractional change of the abundance for the species, x, at vertical level i when the rate coefficient of reaction j is doubled. The summation of the square of the fractional change (S) over every altitude and reaction gives the sensitivity to reaction rate coefficients.

Figure 1.1 shows the sensitivity for hydrocarbons. CH_4 is the least sensitive to the uncertainties in reaction rate coefficients because of the dominant effect of vertical transport. The mixing ratio of CH_4 remains constant up to the homopause where eddy diffusivity equals the molecular diffusivity. The eddy diffusivity is, therefore, fixed at the homopause but remains unconstrained below. A second species must be chosen to infer the eddy diffusivity below the homopause. Most previous works use C_2H_6 as an auxiliary species to constrain the eddy diffusivity in the stratosphere. But we find that C_2H_2 is a better mixing tracer than C_2H_6.

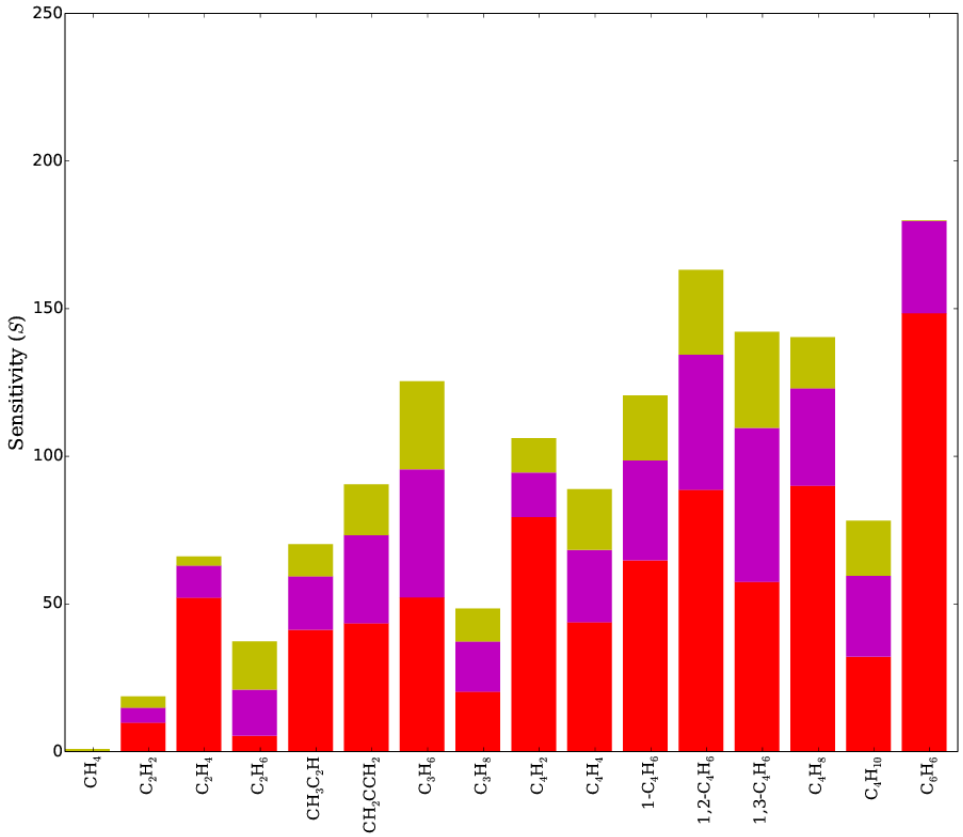

Figure 1.1 Summation of the square of fractional changes over 82 levels and 297 reactions for 18 species when the rate coefficient for each reaction is doubled. See equation (1.2) for the definition of sensitivity. For clarity, radicals are not shown in the figure because their abundances are not affected by transport due to their short chemical lifetimes. The total sensitivity is divided into three parts: red part is the contribution from 50 km to 500 km; magenta, from 500 km to 1000 km; yellow, above 1000 km.

First, unlike the spectral features of C_2H_6, those of C_2H_2 do not overlap with those of CH_4 in the Far-Ultraviolet (FUV) region. Observations from FUV stellar occultations and CIRS limb-view revealed a complete profile in the vertical. This profile exhibits a relatively constant mixing ratio below 500 km and a rapid pick-up above 500 km, indicating a transition from a transport dominated regime to a regime where the chemical production

and vertical transport are of comparable strength. The strength of eddy diffusion in such a regime can be measured through the strength of chemical reactions.

Second, the chemistry of C_2H_2 is well understood. Figure 1.2 shows the production and loss rates for C_2H_2. The major formation and loss pathways for C_2H_2 are photolytic reactions, which are more certain than the three body reaction (such as $2CH_3 + M \rightarrow C_2H_6 + M$) that is responsible for the formation of C_2H_6. The abundance of C_2H_2 exhibits less sensitivity to the uncertainties of rate coefficients than do the abundances of other hydrocarbons, excepting only CH_4 (see Figure 1.1).

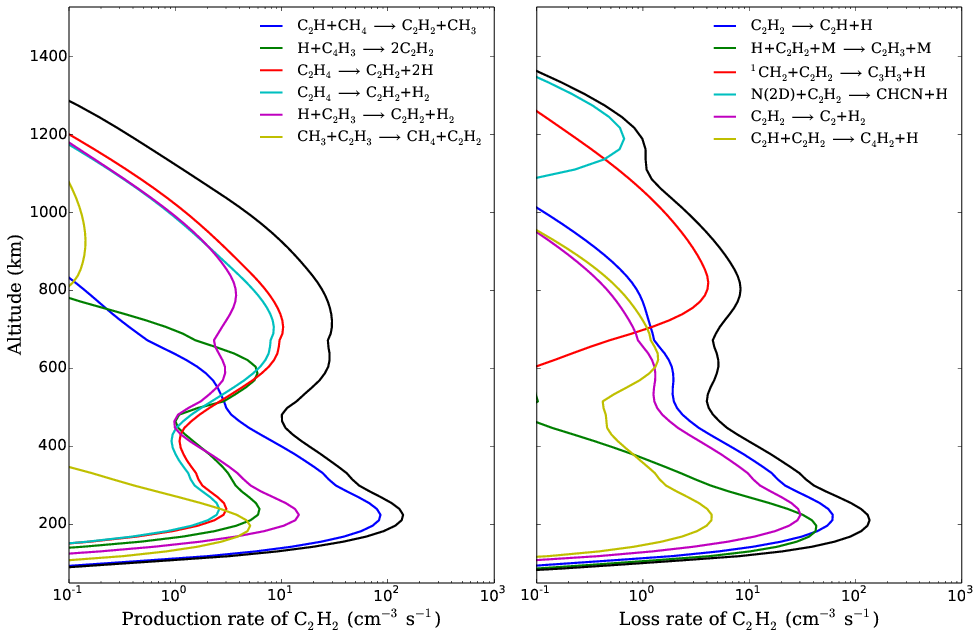

Figure 1.2 Production and loss rates of C_2H_2. Black lines show the total production (loss) rate for C_2H_2. Other colored lines show the contribution from each reaction labeled in the figure.

Third, C_2H_2 is the parent species that drives the whole reaction chain in the stratosphere via photosensitized dissociation of C_2H_2 (Yung et al., 1984). Successfully simulating the abundance of C_2H_2 is of paramount importance for modeling the related species (e.g. C_4H_2) (Lavvas et al., 2008b).

1.4 Retrieval method and results

We use the one-dimensional Caltech/JPL photochemical model (Liang et al., 2007; Yung, 1987; Yung et al., 1984; Zhang et al., 2010) for modeling Titan's atmospheric chemistry. We updated the model with the new set of chemical reactions from (Moses et al., 2005a). The background atmospheric density profile is constructed from Cassini observations. The thermospheric density profile uses the measurements from Cassini/INMS (Westlake et al., 2011a) during the T40 flyby, which is in the best agreement with the density profile inferred from Cassini/UVIS EUV occultations (Kammer et al., 2013). The stratospheric density profile uses the measurements from Cassini/HASI (Fulchignoni et al., 2005). The mesospheric density profile is then extrapolated from the thermospheric density profile, assuming constant temperature, until it connects to the stratospheric profile. CH_4 is not allowed to escape from the top of the atmosphere in the nominal model. We will discuss the case of escape in section 1.6. To speed the model up and reduce the complexity, only neutral hydrocarbons and nitriles are included in the present model since the ion reactions at the top of the atmosphere can have only a minor effect on the abundance of C_2H_2, and these effects do not influence the lower atmosphere where the retrieval of the eddy diffusion profile is performed. The optical properties of the aerosols (Michelangeli et al., 1989) are incorporated in our radiative model; in practice the most important impact of these rather dark aerosols is the extinction of UV radiation lower in the atmosphere. The particle size and density as a function of altitude are taken from Titan's microphysical model by (Lavvas et al., 2010). The aerosol density profile is scaled so that the line-of-sight aerosol optical depth above 400 km matches the UVIS measurements (Kammer et al., 2011; Kammer et al., 2013; Koskinen et al., 2011) at 190 nm. For the other UV to

visible wavelengths, we assume the cross section (σ) behaves as a power law function of the wavelength (λ), $\sigma \propto \lambda^n$. In the current model, we assume that the extinction cross section is independent of wavelength, i.e. $n = 0$. We also tested various power laws, where the power n ranges from -4 (Rayleigh limit) to 0 (flat distribution) and found that the inclusion of aerosol shielding has a profound impact on the photochemistry in the lower atmosphere of Titan, but different choices of power laws do not significantly change the results. The initial eddy diffusion profile is the same as the one used in Liang et al. (2007) below 800 km. Above 800 km, the eddy diffusivities are set to 1×10^8 cm^2 s^{-1} so as to match the observed distribution of CH_4. We call this model the nominal model. Figure 1.3 shows the density profile and compares the model results for with the observed profiles.

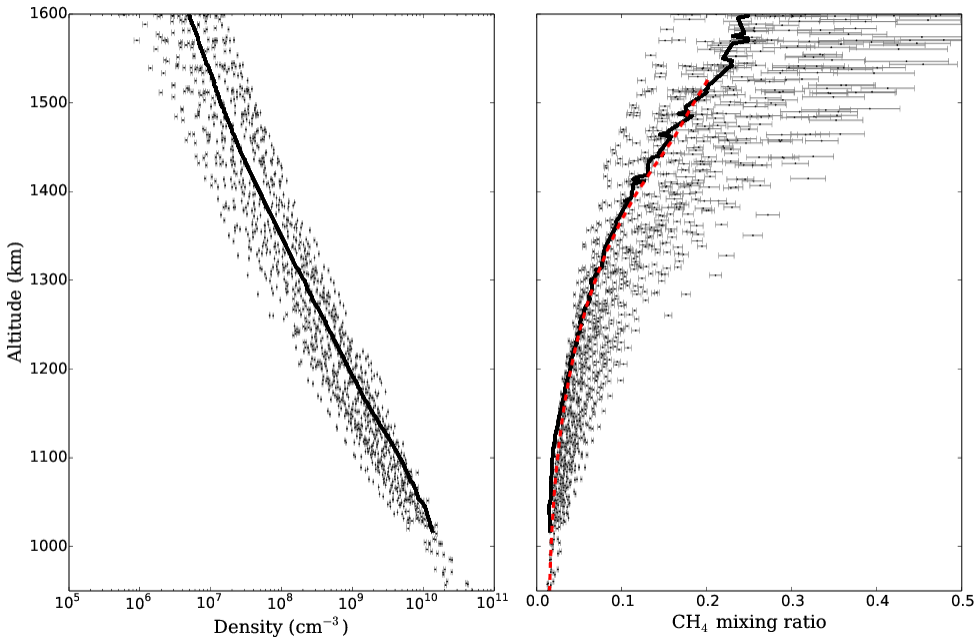

Figure 1.3 Density and CH_4 profile. Left panel: density profiles replotted from Westlake et al. (2011a). The data points are reduced by a factor of five for clarity. T40 flyby is marked in thick black line. Right panel: the nominal model result (red dashed line) along with the observed CH_4 profile from 21 flybys. The T40 flyby is also marked in thick black line.

We use the Levenberg-Marquardt algorithm (Moré, 1978), a standard non-linear least square optimization method, to retrieve the eddy diffusion profile. The cost function is the square of the difference between the model and the observations:

$$J = || \ (x^n(\beta) - x^n_{obs})^T S_{obs} (x^n(\beta) - x^n_{obs}) \ || \ , \tag{1.3}$$

where x is the log abundance; β is the eddy diffusion profile mapped by five sampling levels equally spaced between 130 and 1000 km. Eddy diffusivities at higher or lower levels are set equal to the boundary values. The mapping function is defined as:

$$\beta(z) = \frac{2Y(z_i)K_\infty}{Y(z_i) + K_\infty}, \tag{1.4}$$

where $Y(z_i)$ is a cubic spline function that fits the five sampling levels; K_∞ is the upper bound of the eddy diffusivity which is set to 1×10^8 cm^2 s^{-1}. For altitudes lower than 500 km, x^n_{obs} is the mean value of seven non-polar measurements from Cassini/CIRS limb view (Vinatier et al., 2010a); for altitudes above 500 km and below 1000 km, x^n_{obs} is the mean value of five Cassini/UVIS stellar occultation measurements (Kammer et al., 2011); S_{obs} is the observational error covariant matrix. For simplicity, off-diagonal elements are neglected and we give equal weights to both the average and the errors. The vector $x^n(\beta)$ models the concentration based on eddy diffusion profile β.

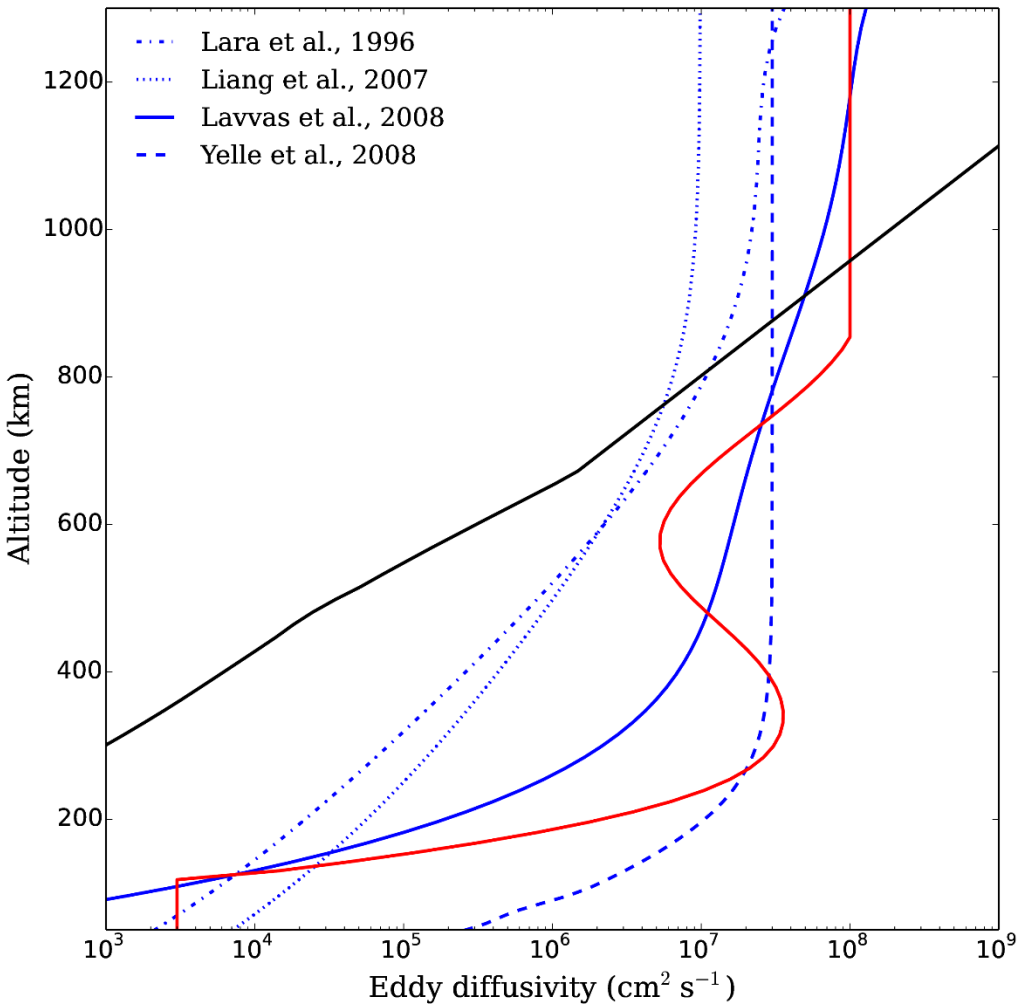

Figure 1.4 Eddy diffusion profile. The eddy diffusion profile retrieved from the abundance of C_2H_2 (red line) is plotted along with the molecular diffusion coefficients for CH_4 (black line) and the initial guess of the eddy diffusion profile (blue dotted line from Liang et al. (2007)). Eddy diffusion profiles used in previous modelings are compared in the figure.

We start from the nominal model and adjust the eddy diffusivity at sampled levels according to the Levenberg-Marquardt algorithm so as to minimize the cost function. The retrieved eddy diffusion profile is shown in Figure 1.4 (red solid line) along with profiles used in previous modeling and the molecular diffusivity of CH_4. The eddy diffusivity is small in the lower stratosphere but increases sharply by three orders of magnitude from 200 to 300 km, reaching a prominent maximum of eddy diffusivity ($\sim 4 \times 10^7$ cm^2 s^{-1}) at around 300 km. This value is approximately the same as that which Yelle et al. (2008a) uses for the asymptotic expression. From 300 to 600 km the eddy diffusivity decreases with altitude and creates a local minimum ($\sim 5 \times 10^6$ cm^2 s^{-1}) at around 600 km, implying a stable layer in Titan's mesosphere. The difference between the maximum value at 300 km and the minimum value at 600 km is about an order of magnitude, which makes it a robust feature. The decrease of eddy diffusivity is consistent with the rapid pick-up of the mixing ratio of C_2H_2. Above this local minimum, the eddy diffusivity increases again with altitude and reaches the boundary value of 1×10^8 cm^2 s^{-1} at the homopause.

Solid red lines in Figure 1.5, Figure 1.6 and Figure 1.7 show the model result using the retrieved eddy diffusion profile. The mixing ratio of C_2H_2 remains constant at $\sim 3 \times 10^{-6}$ from 100 to 500 km and rapidly increases by two orders of magnitude from 500 km to 1000 km. Most photochemical models using a monotonic eddy diffusion profile fail to capture this feature. They usually underestimate the abundance of C_2H_2 in the mesosphere (e.g. Figure 4 in Lavvas et al., 2008b; Figure 7 in Krasnopolsky, 2009). The non-monotonic eddy diffusion profile constrained by FUV stellar occultation provides the best fit to the observations.

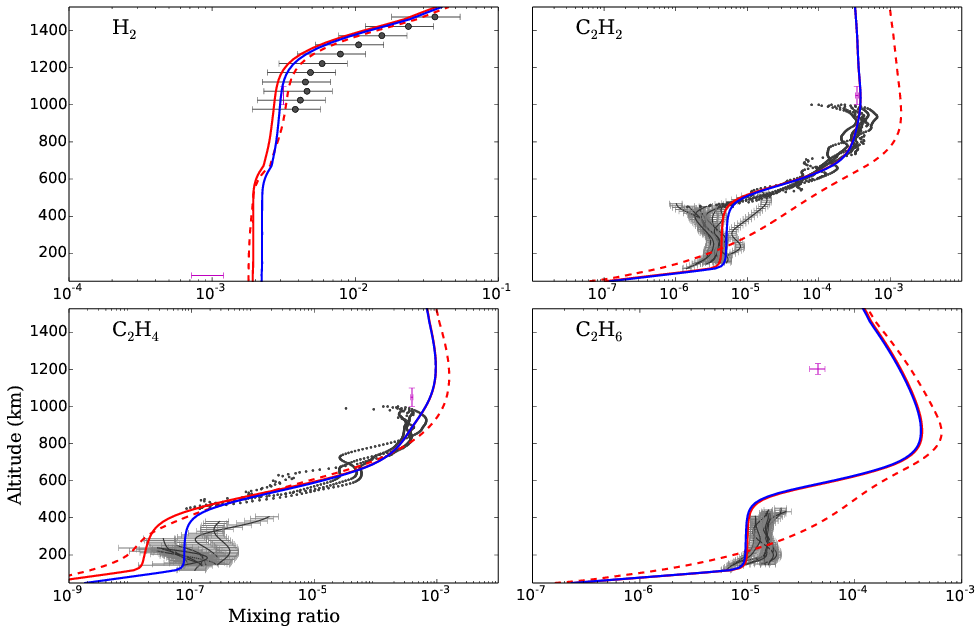

Figure 1.5 The mixing ratios of H_2 and C_2-hydrocarbons. Red dashed line is the result of the nominal model; red solid line is the result using our retrieved eddy diffusion profile; blue line is the result of using the retrieved eddy diffusion profile and with the revised rate coefficients for R113. The observations are plotted along with the model results. Black dots in the H_2 are the observations from INMS (Cui et al., 2008). The error bars indicate a factor of two (generally the spreading of density profiles). Black dots in the upper atmosphere are from FUV stellar occultation (Kammer et al., 2013). Black dots in the lower atmosphere are from CIRS limb view (Vinatier et al., 2010a). Magenta points at about 1000 km are from INMS (Magee et al., 2009).

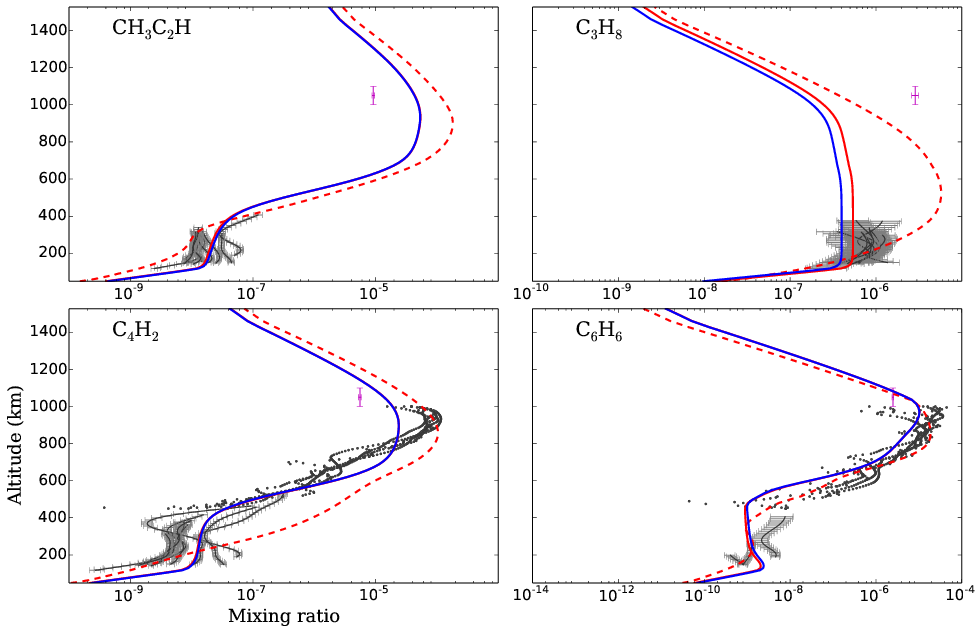

Figure 1.6 Same as Figure 1.5 for higher hydrocarbons.

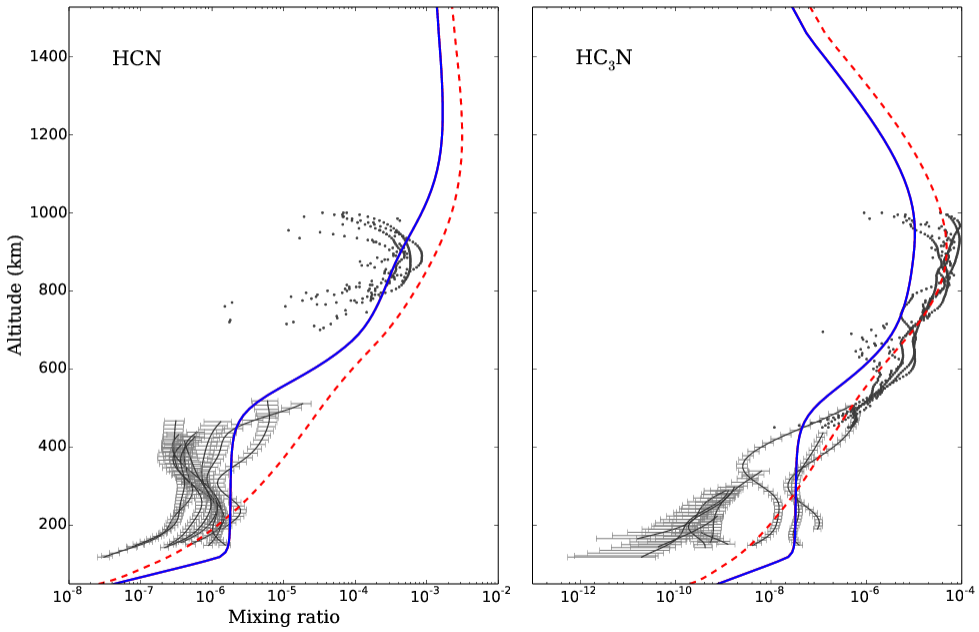

Figure 1.7 Same as Figure 1.5 for HCN and HC_3N.

The mixing profile of C_2H_4 does not change much when the new eddy diffusion profile is applied since C_2H_4 is highly reactive in Titan's atmosphere and its chemical timescale ($\sim 10^7$ s at 100 km) is short compared to the eddy diffusion timescale ($\sim 10^9$ s at 100 km). The profile of C_2H_4 can be largely explained by local chemical equilibrium and is insensitive to eddy diffusion. The stratospheric mixing ratio of C_2H_4 is about 10^{-8} while the observation from Cassini/CIRS gives a mixing ratio of 10^{-7}, 10 times bigger than the model.

For the saturated hydrocarbons, we overestimate the thermospheric abundance for C_2H_6 and underestimate that of C_3H_8 by about five times. The disagreement with the INMS results was first noticed by Lavvas et al. (2008b), yet the possible reasons for the discrepancy are still unknown. Other hydrocarbons are either short-lived species (CH_3C_2H, C_6H_6) which are not affected by modifying the eddy diffusion profile or are derived from C_2H_2 photolysis (C_4H_2). Their abundances agree with the observations as long as the abundance of C_2H_2 is in good agreement.

In the next section, we explore a revised three-body reaction rate that helps to solve the problem of C_2H_4 as well as a discussion on thermospheric abundance for saturated hydrocarbons.

1.5 Revised chemistry

The underestimation of C_2H_4 in the stratosphere has long been reported in previous modeling (Lavvas et al., 2008b; Lebonnois et al., 2001; Wilson and Atreya, 2004). In addition, it marred not only several photochemical models of Titan but also the photochemical models for giant planets (Moses et al. (2005a), Figure 14 for Jupiter, Figure 31 for Saturn and Figure 32 for Neptune; Moses and Greathouse (2005), Figure 6). Only Lara et al. (1996)'s model could produce the right amount of ethylene in the stratosphere by artificially imposing an upward flux of C_2H_4 from the ground.

Lavvas et al. (2008b) suggested that enhancement of ethylene was caused by the downwelling branch of Hadley circulation. Two major problems could be raised with this scenario. First, Cassini/CIRS observations (Vinatier et al., 2010a) show that the latitudinal concentration gradient of a species is weak outside the polar vortex ($\sim 45^{\circ}$N). Yet, inside the polar vortex, where the dynamical mixing is prohibited by a steep horizontal potential vorticity gradient (Teanby et al., 2008), the concentration is enhanced by a factor of five to 10. Therefore, the enhancement of C_2H_4 through Hadley circulation would probably be confined in the polar region and would not affect the tropics and mid-latitudes. Second, the mixing ratio of C_2H_4 exhibits a clear decrease with altitude, which could not be explained by the Hadley cell if the production zone of were only in the mesosphere. Therefore, the negative mixing gradient of C_2H_4 in lower latitudes disproves the downwelling scenario and calls for an additional source in the stratosphere. This source can be either the horizontal advection from the winter pole towards the equator (Crespin et al., 2008) or a stronger three-body recombination in the stratosphere. Since the problem is universal in

the photochemical modeling of the outer solar system, we suggest that it occurs because of the underestimation of reaction rate coefficients for three-body reactions.

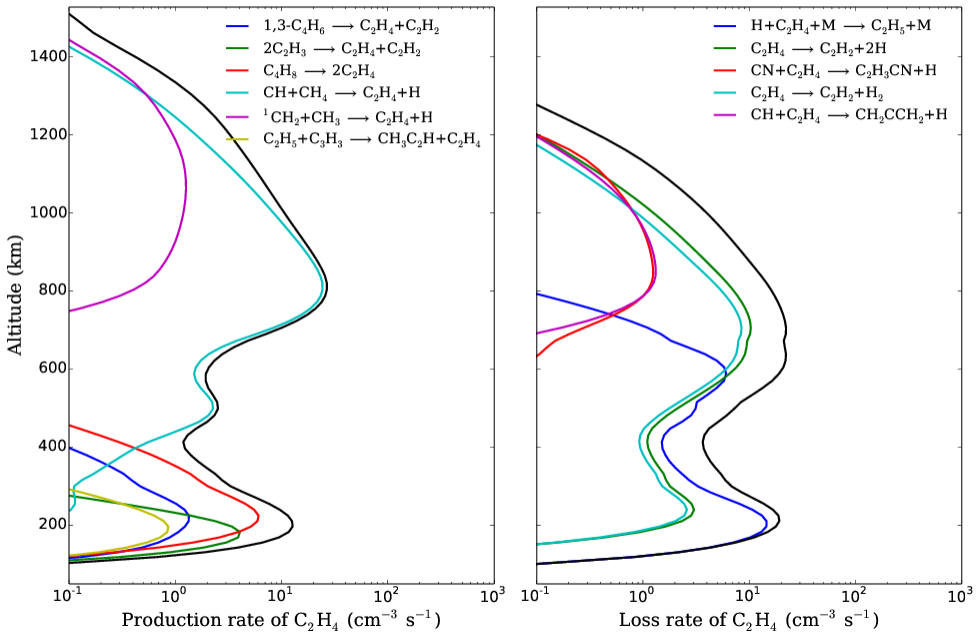

Figure 1.8 Production and loss rates of C_2H_4. Black lines show the total production (loss) rate for C_2H_4. Other colored lines show the contribution from each reaction labeled in the figure.

Figure 1.8 shows reaction rate profiles of important reactions for the production and loss of C_2H_4. These reactions account for over 80% of the total production and loss of C_2H_4. In the thermosphere and mesosphere (> 500 km), C_2H_4 forms mainly through the insertion of the CH radical into CH_4:

$$CH + CH_4 \rightarrow C_2H_4 + H\,. \qquad \text{(R164)}$$

Below 500 km, where CH_4 photolysis is self-shielded, photolysis back from higher hydrocarbons (1,3-C_4H_6, C_4H_8) and radical-radical combination (CH_3) gradually take over the production of C_2H_4.The most prominent reactions are:

$$C_4H_6 \rightarrow C_2H_4 + C_2H_2\,, \qquad \text{(R64)}$$

$$C_4H_8 \rightarrow 2C_2H_4\,, \qquad \text{(R71)}$$

$$2C_2H_3 \rightarrow C_2H_4 + C_2H_2\,. \qquad \text{(R251)}$$

A large portion of C_2H_4 loss is owing to photodissociation into C_2H_2 through the reaction:

$$C_2H_4 \rightarrow C_2H_2 + H_2/2H\,. \qquad \text{(R13,R14)}$$

In the upper stratosphere, where the atmospheric density is relatively high and photons are scarce, loss due to the three-body reaction:

$$H + C_2H_4 + M \rightarrow C_2H_5 + M\,, \qquad \text{(R113)}$$

becomes more efficient and accounts for more than 80% of the total loss rate around 200 km. In short, C_2H_4, formed by the photolytic products of CH_4 and higher hydrocarbons equilibrates its abundance through photodissociation in the mesosphere and through combination with atomic H in the stratosphere.

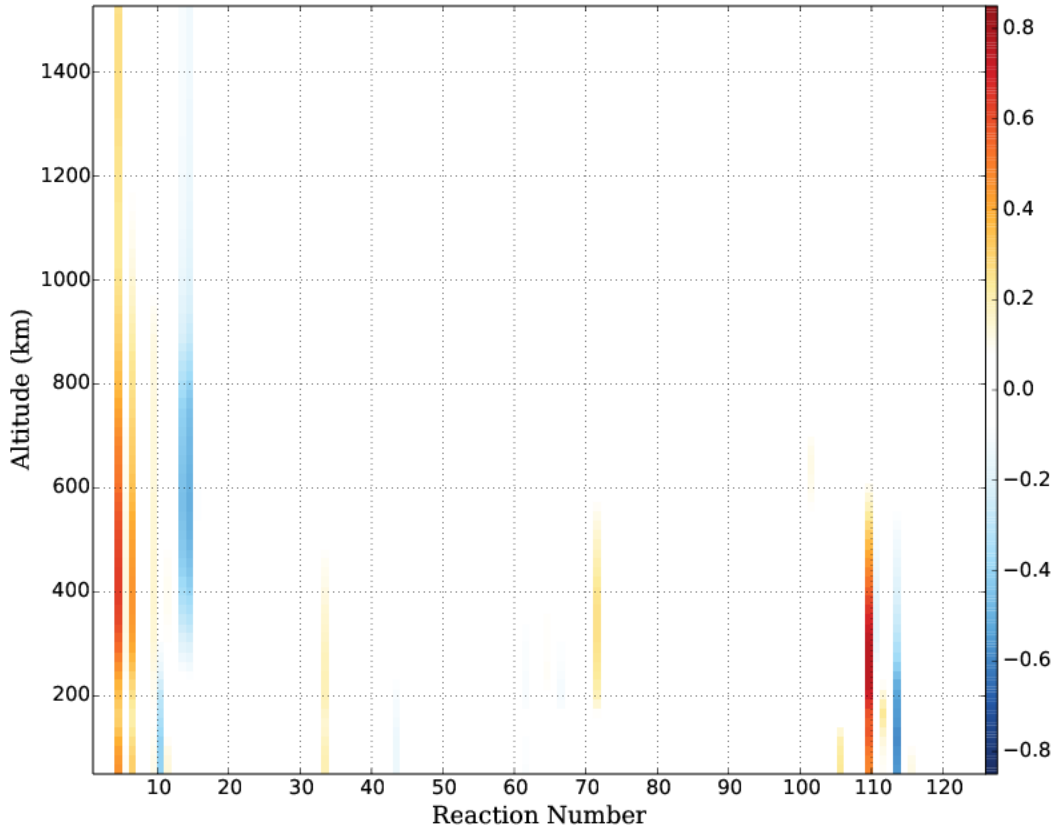

Figure 1.9 Fractional change of C_2H_4. Color shows the fractional change of C_2H_4 when each reaction rate coefficient is doubled. The abscissa is the reaction number in the model. Any reaction with a reaction number larger than 120 is not important and is omitted for clarity. The first 120 reactions are listed in Table 1.1.

We perform a linear sensitivity study to identify the key reactions that control the abundance of C_2H_4 in the stratosphere. Figure 1.9 shows the fractional change of C_2H_4 when each reaction rate coefficient is doubled. It shows that the abundances of C_2H_4 in the lower atmosphere are most sensitive to two three-body reactions:

$$H + C_2H_2 + M \rightarrow C_2H_3 + M\,, \quad \text{(R109)}$$

$$H + C_2H_4 + M \rightarrow C_2H_5 + M\,. \quad \text{(R113)}$$

R109 is important because it offers a source for one of the major production pathway (R251) for C_2H_4. The combination of R109 and R251 produces a positive feedback to convert C_2H_2 to C_2H_4 through C_2H_3. The three-body reaction, R113, is the major sink for C_2H_4 in the stratosphere. We find that the reaction rate coefficient used in (Moses et al., 2005a) model does not agree with the laboratory measurement at higher temperatures (Figure 1.10). We propose a new expression for the reaction rate coefficient for R113 to match the observations at all measured temperatures.

$$\begin{cases} k_0 = 5.4 \times 10^{-25}\, T^{-1.46}\, e^{-1300/T} \\ k_\infty = 1.8 \times 10^{-13}\, T^{0.7}\, e^{-600/T} \end{cases} \quad (1.5)$$

where k_0 is the low-pressure limiting rate constant in units of $cm^6\ s^{-1}$; k_∞ is the high-pressure limiting rate constant in units of $cm^3\ s^{-1}$. The new expression predicts a lower reaction rate coefficient (~ 10 times) at Titans temperature.

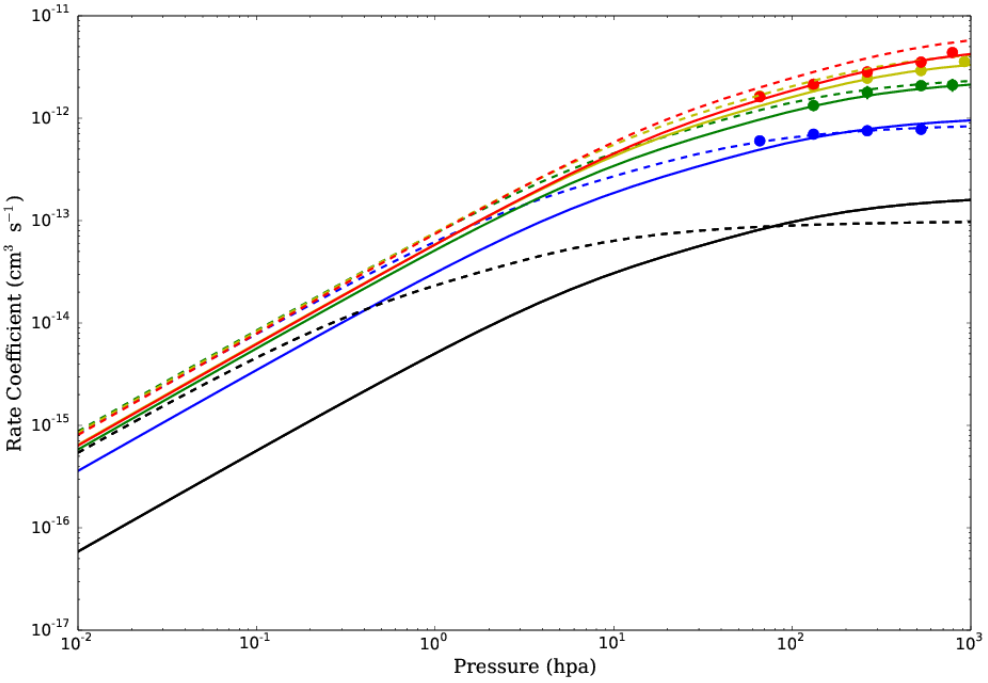

Figure 1.10 Rate coefficients for the reaction H + C_2H_4 + M → C_2H_5 + M. Colored dots with error bars are the laboratory measurements from Lightfoot and Pilling (1987). Temperatures are indicated by the color: red (604 K), yellow (511 K), green (400 K), blue (285 K), black (170 K). Dashed lines are the reaction rate coefficients used in (Moses et al., 2005a); solid lines are the new reaction rate coefficients, see equation (1.5). No laboratory measurements are available for temperatures on Titan (~170 K) and in the pressure range of the stratosphere (~0.1 hPa).

The model mixing ratios for two alkanes, C_2H_6 and C_3H_8, in the thermosphere are higher and lower, respectively, than the observations (see Figure 1.5 and Figure 1.6). Owing to the large variability of the thermospheric composition (see the spread of density profiles from different flybys in Figure 1.3), a single in situ measurement might not be representative of the average condition. If we ignore the natural variability and assume that the INMS results do manifest the average condition, the discrepancy could arise either from

the lack of ion reactions in the current model or from the uncertainties in the three-body reactions' rate coefficients.

Ion reactions do not affect the key species, C_2H_2, based on which we retrieve the eddy diffusivity. Thus, we tested the possible influence of three body reactions only. In this region the formation of these alkanes is primarily through three-body reactions:

$$2CH_3 + M \rightarrow C_2H_6 + M\,, \qquad \text{(R109)}$$

$$CH_3 + C_2H_5 + M \rightarrow C_3H_8 + M\,. \qquad \text{(R113)}$$

The region where these reactions take place on Titan is around 800 km or 8 nbar and the temperature is 170 K. There are no direct laboratory measurements for the rate coefficients of the above reactions in this pressure and temperature regime. Vuitton et al. (2012a) proposed several updates for the reaction rate coefficients based on transition state theory. We carried out a sensitivity test using the reaction rate coefficients in Vuitton et al. (2012a)'s run C. We found that the modified rate coefficient for R206 and R212 overproduced the abundance for C_3H_8. We performed another test trying to match the thermospheric abundance for C_3H_8. We found that the rate coefficient of R212 should increase by a factor of 100. We were unable to match the thermosphere abundance of C_2H_6 by simply increasing or decreasing the reaction rate of R206. We should point out these adjustments for three body reactions have minor effects on the abundance of C_2H_2. Therefore, they do not affect our results for the retrieval of the eddy diffusion profile.

For comparison, we plot the model result using modified chemistry (equation (1.5), R113) against the nominal model (blue lines versus red lines in Figure 1.5, Figure 1.6, Figure 1.7). The new model agrees better with the observations of the stratospheric abundance of C_2H_4.

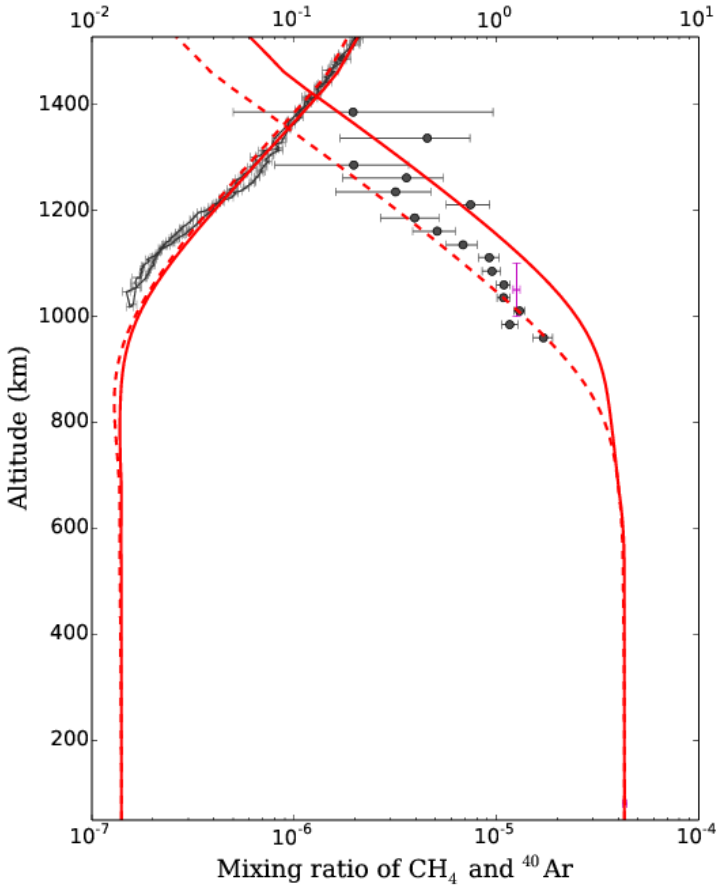

Figure 1.11 Mixing ratio of CH_4 (top axis) and ^{40}Ar (bottom axis) from the non-escaping model (solid lines) and escaping model (dashed lines). In the non-escaping model, the eddy diffusivity at the CH_4 homopause equals 1×10^8 cm^2 s^{-1}. Observations of ^{40}Ar are represented by black dots with error bars (Yelle et al., 2008a) . Observations of CH_4 are from T40 flyby (Westlake et al., 2011a).

1.6 Discussion and conclusion

CH_4 escape: In the current model, CH_4 does not escape from the top of the atmosphere because is CH_4 too heavy to escape through normal processes and no direct evidence of the escape has been found. But escape is crucial to match the abundance of ^{40}Ar and CH_4 simultaneously (Yelle et al., 2008a). It is, therefore, included in many recent photochemical models, e.g. (Lavvas et al., 2008b). To study this impact, we created a model that allows CH_4 to escape at the rate of 1.0×10^9 cm^{-2} s^{-1}. Given the escape flux, we perform the same procedure to retrieve the eddy diffusion profile. Comparisons of CH_4 and ^{40}Ar mixing ratios derived from Cassini/INMS are shown in Figure 1.11. As described in Yelle et al. (2008a), applying escaping flux has the same effect as large eddy diffusivity. The CH_4-escape model requires a low eddy diffusivity of 1.5×10^7 cm^2 s^{-1}, similar to Yelle et al. (2008a)'s result. It fits equally well to CH_4 as the non-escaping case but better fits the ^{40}Ar profile. Again, we should point out that whether CH_4 escapes or not does not affect our retrieval result, for the major feature of the eddy diffusion profile is located below the homopause.

Heterogeneous reactions: The aerosols in the atmosphere of Titan have two important effects on the chemistry other than the UV shielding: (1) recombination of H atoms on the surface of aerosols, and (2) heterogeneous removal of C_2H_2, thereby converting it from gas to aerosols.

The most important impact of aerosols on H atoms is the catalytic recombination of the atoms to form H_2. The probability of recombination was measured by Sekine et al. (2008a). Using their values and the surface area of aerosols on Titan from Lavvas et al. (2008b), we investigated the effect of the removal of H atoms on Titan via this process. The results showed that effect of H recombination on aerosols is small, in agreement with Krasnopolsky (2009). Some of the extremely cases reported by Sekine et al. (2008c) used aerosol profiles that are unrealistic compared to Lavvas et al. (2010).

Our nominal model does not include the heterogeneous reactions converting C_2H_2 to aerosols. However, we investigated a heterogeneous loss for C_2H_2 as prescribed in Liang et al. (2007). The results showed that the loss due to heterogeneous reactions is much less than the total chemical loss, as mentioned in Lavvas et al. (2008b). Therefore, the exclusion of heterogeneous reactions does not affect the retrieval result.

Possible dynamical interpretation: In this work, we retrieved the eddy diffusion profile based on the vertical distribution of C_2H_2. The location of the low eddy diffusion zone featured by the new eddy diffusion profile coincides with the altitude of the detached haze layer. We speculate about a possible dynamical interpretation of the eddy diffusion profile based on the effect of aerosol heating. Liang et al. (2007) first observed tholins, which are probably the intermediates in the formation of aerosols at 1000 km from UVIS. These particles, if produced by ion reaction at the top of the atmosphere, could be transported downward quickly and grow slowly when the eddy diffusivity is large. However, as the

particle density increases, they absorb enough solar heat to create a local temperature inversion. Liang et al. (2007) estimated a heating rate of aerosols which results in a temperature inversion of about 20 K. The temperature inversion layer stabilizes the atmosphere, creating a low eddy diffusion zone under it, and slows the downward transport of aerosols. The aerosols are retained in this layer and particles could grow more rapidly through fractal aggregation , absorbing more heat as a result. This kind of positive feedback mechanism predicts that the vertical mixing intensity would decrease in the inversion layer (at about 500 km), which is manifested by a decrease in the eddy diffusivity. This growth of fractal aerosol permitted by a slow vertical transport in a stable layer might explain the existence of the detached haze layer observed by Cassini/UVIS. A rigorous study of such a mechanism requires a coupled modeling of radiative processes, aerosol microphysics, chemical kinetics and dynamics, which is deferred to later work.

Conclusion: This work uses the latest Cassini observation to investigate the non-monotonically increasing eddy diffusion profile. The modeling results are generally in better agreement with observations than those of previous models. Chemical kinetics is examined and modified so as to match the observations of in the stratosphere. The new expression of the reaction rates agrees better with the laboratory measurements at all high temperatures and pressures. This might help to solve a similar problem for the photochemical modeling of C_2H_4 on giant planets.

1.7 Appendix

Table 1.1 Photochemical reaction list, see Moses et al. (2005a) for reaction rate coefficients and references.

No.	Reaction	No.	Reaction
R1	$H_2 \longrightarrow 2\,H$	R61	$1,3\text{-}C_4H_6 \longrightarrow C_4H_5 + H$
R2	$^3CH_2 \longrightarrow CH + H$	R62	$1,3\text{-}C_4H_6 \longrightarrow C_4H_4 + H_2$
R3	$CH_3 \longrightarrow CH + H_2$	R63	$1,3\text{-}C_4H_6 \longrightarrow C_3H_3 + CH_3$
R4	$CH_3 \longrightarrow {}^1CH_2 + H$	R64	$1,3\text{-}C_4H_6 \longrightarrow C_2H_4 + C_2H_2$
R5	$CH_4 \longrightarrow CH_3 + H$	R65	$1,3\text{-}C_4H_6 \longrightarrow 2\,C_2H_3$
R6	$CH_4 \longrightarrow {}^1CH_2 + H_2$	R66	$C_4H_8 \longrightarrow 1,3\text{-}C_4H_6 + 2\,H$
R7	$CH_4 \longrightarrow {}^1CH_2 + 2\,H$	R67	$C_4H_8 \longrightarrow C_3H_5 + CH_3$
R8	$CH_4 \longrightarrow {}^3CH_2 + 2\,H$	R68	$C_4H_8 \longrightarrow CH_3C_2H + CH_4$
R9	$CH_4 \longrightarrow CH + H + H_2$	R69	$C_4H_8 \longrightarrow CH_2CCH_2 + CH_4$
R10	$C_2H_2 \longrightarrow C_2H + H$	R70	$C_4H_8 \longrightarrow C_2H_5 + C_2H_3$
R11	$C_2H_2 \longrightarrow C_2 + H_2$	R71	$C_4H_8 \longrightarrow 2\,C_2H_4$
R12	$C_2H_3 \longrightarrow C_2H_2 + H$	R72	$C_4H_8 \longrightarrow C_2H_2 + 2\,CH_3$
R13	$C_2H_4 \longrightarrow C_2H_2 + H_2$	R73	$C_4H_{10} \longrightarrow C_4H_8 + H_2$
R14	$C_2H_4 \longrightarrow C_2H_2 + 2\,H$	R74	$C_4H_{10} \longrightarrow C_3H_8 + {}^1CH_2$
R15	$C_2H_4 \longrightarrow C_2H_3 + H$	R75	$C_4H_{10} \longrightarrow C_3H_6 + CH_4$
R16	$C_2H_5 \longrightarrow CH_3 + {}^1CH_2$	R76	$C_4H_{10} \longrightarrow C_3H_6 + CH_3 + H$
R17	$C_2H_6 \longrightarrow C_2H_4 + H_2$	R77	$C_4H_{10} \longrightarrow C_2H_6 + C_2H_4$
R18	$C_2H_6 \longrightarrow C_2H_4 + 2\,H$	R78	$C_4H_{10} \longrightarrow 2\,C_2H_5$
R19	$C_2H_6 \longrightarrow C_2H_2 + 2\,H_2$	R79	$C_4H_{10} \longrightarrow C_2H_4 + 2\,CH_3$
R20	$C_2H_6 \longrightarrow CH_4 + {}^1CH_2$	R80	$C_5H_4 \longrightarrow C_3H_2 + C_2H_2$
R21	$C_2H_6 \longrightarrow 2\,CH_3$	R81	$C_6H_2 \longrightarrow C_6H + H$
R22	$C_3H_2 \longrightarrow C_3 + H_2$	R82	$C_6H_2 \longrightarrow C_4H + C_2H$

continued on next page

Table 1.1 – continued from previous page

No.	Reaction	No.	Reaction
R23	$C_3H_3 \longrightarrow C_3H_2 + H$	R83	$C_6H_4 \longrightarrow C_6H_3 + H$
R24	$C_3H_3 \longrightarrow C_3H + H_2$	R84	$C_6H_4 \longrightarrow C_6H_2 + H_2$
R25	$CH_3C_2H \longrightarrow C_3H_3 + H$	R85	$C_6H_4 \longrightarrow C_4H_2 + C_2H_2$
R26	$CH_3C_2H \longrightarrow C_3H_2 + H_2$	R86	$C_6H_5 \longrightarrow C_6H_4 + H$
R27	$CH_3C_2H \longrightarrow {}^1CH_2 + C_2H_2$	R87	$C_6H_5 \longrightarrow C_4H_3 + C_2H_2$
R28	$CH_2CCH_2 \longrightarrow C_3H_3 + H$	R88	$C_6H_6 \longrightarrow C_6H_5 + H$
R29	$CH_2CCH_2 \longrightarrow C_3H_2 + H_2$	R89	$C_6H_6 \longrightarrow 3\,C_2H_2$
R30	$C_3H_5 \longrightarrow CH_3C_2H + H$	R90	$C_6H_6 \longrightarrow C_5H_3 + CH_3$
R31	$C_3H_5 \longrightarrow CH_2CCH_2 + H$	R91	$C_6H_6 \longrightarrow C_4H_2 + C_2H_4$
R32	$C_3H_5 \longrightarrow C_2H_2 + CH_3$	R92	$C_6H_6 \longrightarrow 2\,C_3H_3$
R33	$C_3H_6 \longrightarrow C_3H_5 + H$	R93	$LC_6H_6 \longrightarrow C_6H_5 + H$
R34	$C_3H_6 \longrightarrow CH_3C_2H + H_2$	R94	$LC_6H_6 \longrightarrow C_6H_4 + H_2$
R35	$C_3H_6 \longrightarrow CH_2CCH_2 + H_2$	R95	$LC_6H_6 \longrightarrow C_5H_3 + CH_3$
R36	$C_3H_6 \longrightarrow C_2H_4 + {}^1CH_2$	R96	$LC_6H_6 \longrightarrow C_4H_4 + C_2H_2$
R37	$C_3H_6 \longrightarrow C_2H_3 + CH_3$	R97	$LC_6H_6 \longrightarrow 2\,C_3H_3$
R38	$C_3H_6 \longrightarrow C_2H_2 + CH_4$	R98	$C_8H_2 \longrightarrow C_6H + C_2H$
R39	$C_3H_8 \longrightarrow C_3H_6 + H_2$	R99	$C_8H_2 \longrightarrow 2\,C_4H$
R40	$C_3H_8 \longrightarrow C_2H_6 + {}^1CH_2$	R100	$2\,H + M \longrightarrow H_2 + M$
R41	$C_3H_8 \longrightarrow C_2H_5 + CH_3$	R101	$H + CH \longrightarrow C + H_2$
R42	$C_3H_8 \longrightarrow C_2H_4 + CH_4$	R102	$H + {}^1CH_2 \longrightarrow CH + H_2$
R43	$C_4H_2 \longrightarrow C_4H + H$	R103	$H + {}^3CH_2 \longrightarrow CH + H_2$
R44	$C_4H_2 \longrightarrow C_2H_2 + C_2$	R104	$H + {}^3CH_2 + M \longrightarrow CH_3 + M$
R45	$C_4H_2 \longrightarrow 2\,C_2H$	R105	$H + CH_3 + M \longrightarrow CH_4 + M$

continued on next page

Table 1.1 – continued from previous page

No.	Reaction	No.	Reaction
R46	$C_4H_4 \longrightarrow C_4H_2 + H_2$	R106	$H + CH_4 \longrightarrow CH_3 + H_2$
R47	$C_4H_4 \longrightarrow 2\,C_2H_2$	R107	$H + C_2H + M \longrightarrow C_2H_2 + M$
R48	$1\text{-}C_4H_6 \longrightarrow C_4H_4 + 2\,H$	R108	$H + C_2H_2 \longrightarrow C_2H + H_2$
R49	$1\text{-}C_4H_6 \longrightarrow C_3H_3 + CH_3$	R109	$H + C_2H_2 + M \longrightarrow C_2H_3 + M$
R50	$1\text{-}C_4H_6 \longrightarrow C_2H_5 + C_2H$	R110	$H + C_2H_3 \longrightarrow C_2H_2 + H_2$
R51	$1\text{-}C_4H_6 \longrightarrow C_2H_4 + C_2H + H$	R111	$H + C_2H_3 + M \longrightarrow C_2H_4 + M$
R52	$1\text{-}C_4H_6 \longrightarrow C_2H_3 + C_2H + H_2$	R112	$H + C_2H_4 \longrightarrow C_2H_3 + H_2$
R53	$1\text{-}C_4H_6 \longrightarrow 2\,C_2H_2 + H_2$	R113	$H + C_2H_4 + M \longrightarrow C_2H_5 + M$
R54	$1,2\text{-}C_4H_6 \longrightarrow C_4H_5 + H$	R114	$H + C_2H_5 \longrightarrow 2\,CH_3$
R55	$1,2\text{-}C_4H_6 \longrightarrow C_4H_4 + 2\,H$	R115	$H + C_2H_5 \longrightarrow C_2H_4 + H_2$
R56	$1,2\text{-}C_4H_6 \longrightarrow C_3H_3 + CH_3$	R116	$H + C_2H_5 + M \longrightarrow C_2H_6 + M$
R57	$1,2\text{-}C_4H_6 \longrightarrow C_2H_4 + C_2H_2$	R117	$H + C_2H_6 \longrightarrow C_2H_5 + H_2$
R58	$1,2\text{-}C_4H_6 \longrightarrow C_2H_3 + C_2H_2 + H$	R118	$H + C_3H_2 + M \longrightarrow C_3H_3 + M$
R59	$1,2\text{-}C_4H_6 \longrightarrow C_2H_3 + C_2H + H_2$	R119	$H + C_3H_3 + M \longrightarrow CH_3C_2H + M$
R60	$1,2\text{-}C_4H_6 \longrightarrow 2\,C_2H_2 + H_2$	R120	$H + C_3H_3 + M \longrightarrow CH_2CCH_2 + M$

Chapter 2 Vertical distribution of C_3-Hydrocarbons in the stratosphere of Titan

Cheng Li[1], Xi Zhang[2], Peter Gao[1] and Yuk Yung[1]

[1]Division of Geological and Planetary Science, California Institute of Technology, Pasadena, CA, 91125

[2]Lunar and Planetary Laboratory, University of Arizona, Tucson, AZ, 85721

Published in modified form in *Astrophysical Journal Letters*, 803, L19, 2015

2.1 Abstract

Motivated by the recent detection of propene (C_3H_6) in the atmosphere of Titan, we use a one-dimensional Titan photochemical model with an updated eddy diffusion profile to systematically study the vertical profiles of the stable species in the C_3-hydrocarbon family. We find that the stratospheric volume mixing ratio of propene (C_3H_6) peaks at 150 km with a value of 5×10^{-9}, which is in good agreement with recent observations by the Composite Infrared Spectrometer (CIRS) on the Cassini spacecraft (Nixon et al., 2013). Another important species that is currently missing from the hydrocarbon family in Titan's stratosphere is allene (CH_2CCH_2), an isomer of methylacetylene (CH_3C_2H). We predict that its mixing ratio in the stratosphere is about 10^{-9}, which is on the margin of the detection limit. CH_2CCH_2 and CH_3C_2H equilibrate at a constant ratio in the stratosphere by hydrogen-exchanging reactions. By precisely measuring the ratio of CH_2CCH_2 to CH_3C_2H, the abundance of atomic hydrogen in the atmosphere can be inferred. No direct yield for the production of cyclopropane (c-C_3H_6) is available. From the discharge experiments of Navarro-González and Ramírez (1997), the abundance of cyclopropane is estimated to be 100 times less than that of C_3H_6.

Subject keywords: Titan stratosphere, Allene, Hydrocarbon, Photochemical model

2.2 Introduction

Titan's atmosphere is laden with hundreds of interacting hydrocarbon species, which group in families according to the number of carbon atoms in their hydrocarbon chains (i.e. C_1-, C_2-, C_3-hydrocarbon, etc). Many simple hydrocarbon molecules (C_1- and C_2-hydrocarbons) have been found by spectroscopic and mass spectrometric measurements in Titan's atmosphere (Coustenis et al., 2007; Coustenis et al., 2003; Magee et al., 2009; Vuitton et al., 2007). They have also been the subject of extensive investigations in previous photochemical models (Hebrard et al., 2013; Krasnopolsky, 2009; Lavvas et al., 2008a; Vuitton et al., 2012b; Wilson and Atreya, 2004; Wilson and Atreya, 2009; Yung et al., 1984). Recently, analysis of Cassini/CIRS limb-viewing observations (Nixon et al., 2013) identified a peak in the infrared spectrum of Titan's stratosphere at 912.5 cm^{-1}, which is attributed to the ν_{19} band of propene (C_3H_6). By comparing the relative emission strengths of propene and propane (C_3H_8), the stratospheric vertical profile of C_3H_6 is retrieved. This observation provides a new constraint for the photochemical modeling of Titan's atmosphere and fills a gap in the C_3-hydrocarbon family. As Nixon et al. (2013) pointed out, even though the five C_3 molecules, the two isomers of C_3H_4 (allene and methylacetylene), the two isomers of C_3H_6 (propene and cyclopropane), and propane are part of the interwoven net of hydrocarbon species in the atmosphere of Titan, allene (CH_2CCH_2) and cyclopropane (c-C_3H_6) are yet to be detected. Roe et al. (2011) tentatively identified several of the ν_{10} sub-bands of allene amongst the strong emission lines of ethane's ν_{12} band using TEXES (Texas Echelon Cross Echelle Spectrograph) at NASA/IRTF. However, due to the large uncertainties in the laboratory spectra of allene,

measuring its abundance in Titan's atmosphere by comparing laboratory and observed spectra is difficult.

In this letter, we use the Caltech/JPL photochemical model with a recently updated eddy diffusion profile (Li et al., 2014) to explain the observed vertical distribution of propene. We also perform a systematic study of C_3-hydrocarbon chemistry focusing on CH_3C_2H (methylacetylene), CH_2CCH_2 (allene), C_3H_6 (propene), and c-C_3H_6 (cyclopropane). Our photochemical model gives improved results that, for the first time, fit the abundances of all observable hydrocarbons, which is a significant advance over previous work (Hebrard et al., 2013; Krasnopolsky, 2014; Lavvas et al., 2008b; Vuitton et al., 2012b; Wilson and Atreya, 2004; Yung et al., 1984).

In section 2.3, we describe the photochemical model and compare the modeling results for C_1- and C_2-hydrocarbons to the observations. In section 2.4, we examine the vertical profile of C_3H_6 and its production/loss pathways. In section 2.5, we discuss how the relative abundance of two isomers, CH_2CCH_2 and CH_3C_2H, is a strong tracer of atomic H in the atmosphere. In section 2.6, we estimate the abundance of c-C_3H_6, another missing C_3-hydrocarbon. In section 2.7, we state our conclusions.

2.3 Photochemical model and C_2-hydrocarbons

The Caltech/JPL one-dimensional photochemical model for Titan solves the mass continuity equation from 50 to 1500 km in altitude:

$$\frac{\partial n_i}{\partial t} + \frac{\partial \psi_i}{\partial z} = P_i - L_i \,, \tag{2.1}$$

where n_i, P_i, and L_i are the number density and chemical production and loss rates of species *i*, respectively. ψ_i is the vertical flux of species *i* calculated from the equation:

$$\psi_i = -\frac{\partial n_i}{\partial z}(D_i + K_{zz}) - n_i\left(\frac{D_i}{H_i} + \frac{K_{zz}}{H_a}\right) - n_i \frac{\partial T}{\partial z}\frac{(1+\alpha_i)D_i + K_{zz}}{T}, \tag{2.2}$$

where D_i and H_i are the molecular diffusion coefficient and scale height of species *i*, respectively; H_a is the atmospheric scale height; α_i is the thermal diffusion coefficient of species *i*, *T* is the temperature, and K_{zz} is the eddy diffusion coefficient. The K_{zz} vertical profile is similar to that of (Li et al., 2014) but simplified using a log-linear interpolation of four nodal levels at $z_1 = 120$ km, $z_2 = 300$ km, $z_3 = 500$ km, $z_4 = 1000$ km:

$$\begin{aligned}
&\operatorname{Log} K_{zz}(z) \\
&= \begin{cases}
\operatorname{Log}(3\times10^3), & z < z_1 \\
\operatorname{Log}(3\times10^3)\dfrac{z_2 - z}{z_2 - z_1} + \operatorname{Log}(2\times10^7)\dfrac{z - z_1}{z_2 - z_1}, & z_1 \le z \le z_2 \\
\operatorname{Log}(2\times10^7)\dfrac{z_3 - z}{z_3 - z_2} + \operatorname{Log}(2\times10^6)\dfrac{z - z_2}{z_3 - z_2}, & z_2 \le z \le z_3 \\
\operatorname{Log}(2\times10^6)\dfrac{z_4 - z}{z_4 - z_3} + \operatorname{Log}(4\times10^8)\dfrac{z - z_3}{z_4 - z_3}, & z_3 \le z \le z_4 \\
\operatorname{Log}(4\times10^8), & z \ge z_4
\end{cases}
\end{aligned} \tag{2.3}$$

We include aerosols in our model for the absorption of UV radiation. As described in (Li et al., 2014), they are treated as pure absorbers with a flat extinction cross section

independent of wavelength. The particle size and density as a function of altitude are taken from (Lavvas et al., 2011). Their cross sections are scaled so that the line-of-sight aerosol optical depth matches the Cassini/UVIS measurements (Koskinen et al., 2011) at 400-600 km (~10^{-2}). The thermosphere density profile uses the measurements from Cassini/INMS (Westlake et al., 2011b) during the T40 flyby. The stratospheric density profile is interpolated from Cassini/HASI (Fulchignoni et al., 2005). The mesospheric density profile is extrapolated from the thermospheric density profile assuming constant temperature until it connects to the stratospheric profile. The chemical reactions are taken from (Moses et al., 2005b) with adjusted reaction rates for $H + C_2H_4 \xrightarrow{M} C_2H_5$ as recommended by (Li et al., 2014). CH_4 does not escape from the top of the atmosphere because applying an escaping flux to CH4 has the same effect as applying a larger eddy diffusivity (Yelle et al., 2008b). We incline to the second approach because it fits the ^{40}Ar profile better, see Figure 11 in (Li et al., 2014). We refer the reader to (Li et al., 2014) for more details regarding the model.

Figure 2.1 compares the vertical distributions of CH_4, C_2H_2, C_2H_4, and C_2H_6 with the recent observations from Cassini/CIRS (Vinatier et al., 2010b), Cassni/UVIS (Kammer et al., 2013; Koskinen et al., 2011), and Cassini/INMS (Magee et al., 2009). The observations show a near-constant mixing ratio for C_2H_2 and C_2H_6 in the stratosphere, above which the mixing ratios increase gradually until reaching their peak values near 1000 km. C_2H_4 is an exception to this rule. In some flybys, its mixing ratio significantly decreases with altitude. Our model does not reproduce this feature. This is probably due to two-dimensional effects, such as horizontal advection, because mean upwelling or subsidence is not included in the

one-dimensional model. However, our model profiles of CH_4 and C_2-hydrocarbons can match the mean measurements between flybys satisfactorily and serve as the basis for our study of C_3-hydrocarbons.

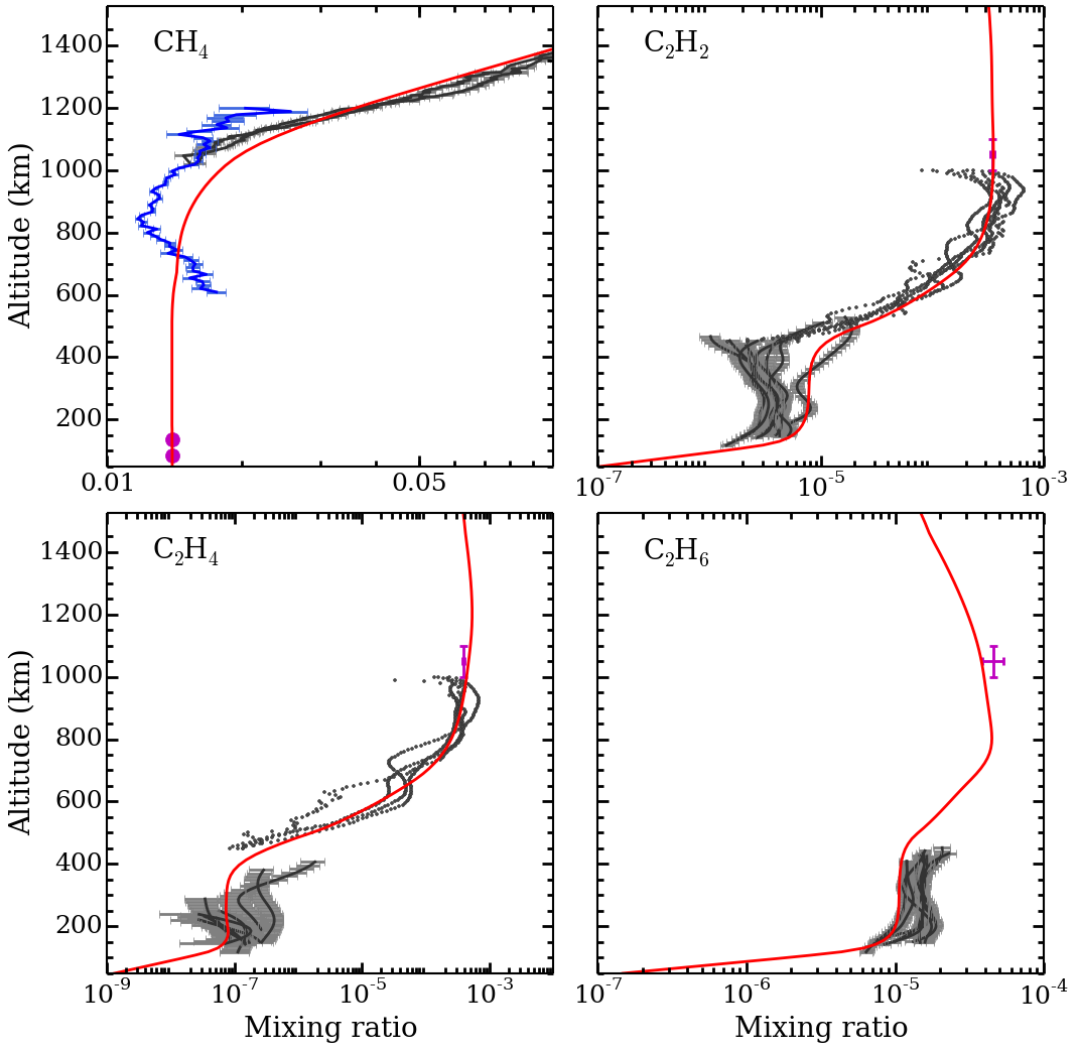

Figure 2.1 The mixing ratios of CH_4 and the C_2-hydrocarbons C_2H_2, C_2H_4, and C_2H_6. Our model results are shown in red. The observations are plotted for comparison. Dark gray lines: CH_4 from the T40 Cassini flyby (Westlake et al., 2011b); blue lines: CH_4 from Cassini/UVIS stellar occultations (Koskinen et al., 2011). For the other species, the points in the upper atmosphere (500 – 1000 km) are from Cassini/UVIS stellar occultations (Kammer et al., 2013), while those in the lower atmosphere are from Cassini/CIRS limb views (Vinatier et al., 2010b). The magenta points at ~1050 km are from Cassini/INMS (Magee et al., 2009).

2.4 Propene (C_3H_6) vertical distribution

The mixing ratios of the C_3-hydrocarbons C_3H_6, CH_2CCH_2, CH_3C_2H, and C_3H_8 are shown in Figure 2.2. The observed stratospheric mixing ratio of C_3H_6 peaks at 200 km with a value of 5×10^{-9}. Our model reproduces a similar peak value and the peaked structure at 150 km. The modeled mixing ratio of C_3H_6 at 1000 km is two times less than the observed value from Cassini/INMS. Two possible reasons might explain this discrepancy. First, the thermosphere of Titan exhibits large natural variability as observed by multiple Cassini flybys, e.g. Figure 2 of Westlake et al. (2011b). The photochemical model tends to represent a mean atmospheric condition that might deviate from individual local measurements as the Cassini/INMS. The abundances of C_3-hydrocarbons in our model more or less deviate from the Cassini/INMS measurements within a factor of two. This magnitude agrees with the spreading of thermospheric density profile among different flybys. Second, our current photochemical does not include the radiative association reaction ($H + C_3H_5 \rightarrow C_3H_6$) which may contribute to half of the production of C_3H_6 at 1000 km (Hebrard et al., 2013). We estimate the effect by doubling the reaction rate of the key reaction identified in the next paragraph and the result matches the Cassini/INMS better.

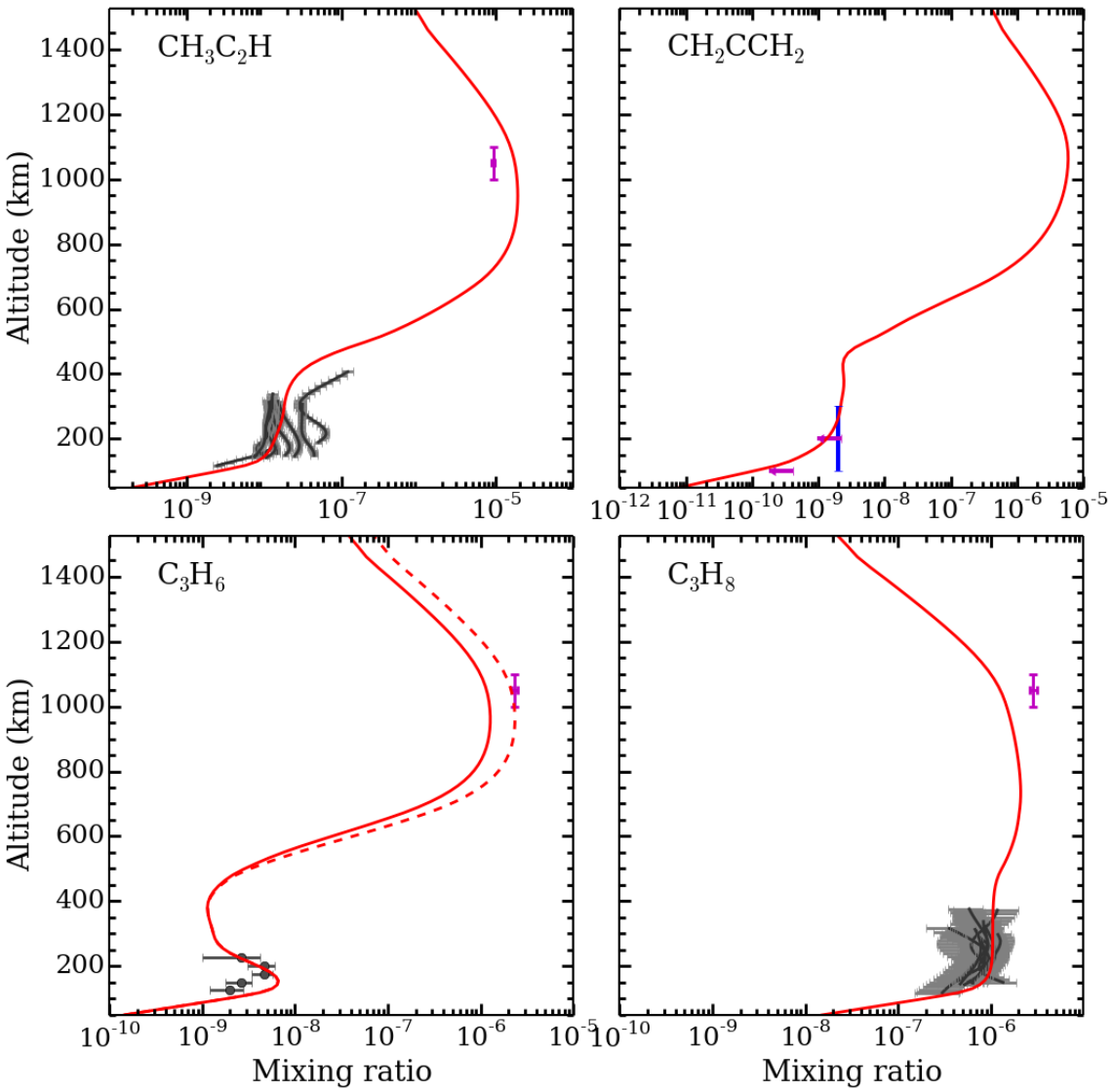

Figure 2.2 Same as Figure 2.1, but for C_3-hydrocarbons. Blue bar in CH_2CCH_2 panel indicates the upper limit by (Coustenis et al., 2003); Magenta points with arrows in CH_2CCH_2 panel indicate the upper limit by (Nixon et al., 2010). Dashed red line in C_3H_6 panel shows the profile when the reaction rate of ($CH + C_2H_6 \rightarrow C_3H_6 + H$) is doubled.

Reactions rates and errors involving the C_3-hydrocarbons have been studied extensively (Hebrard et al., 2013; Loison et al., 2015). However, a systematic analysis of formation/loss pathways for them are limited because of the formidable amount of reactions involved. In this work, we use a greedy algorithm traversing the complete reaction list to find out a subset of reactions that contribute to over 90% of the total formation and loss of a certain species over all altitudes. Reactions with larger rates are preferred to be added in the subset than ones with smaller rates. Figure 2.3 shows the production and loss pathways of C_3H_6 produced by this algorithm. In the upper atmosphere (> 600 km), the production of C_3H_6 is dominated by the insertion of CH radicals into C_2H_6 :

$$CH + C_2H_6 \rightarrow C_3H_6 + H\,, \tag{2.4}$$

where the CH radicals are produced by the photodissociation of CH_4. By contrast, Hebrard et al. (2013) includes the radiative association reaction

$$H + C_3H_5 \rightarrow C_3H_6\,, \tag{2.5}$$

which consists of 61.8% of the production of C_3H_6 at 1000 km and reaction (2.4) contributes 36.7%. Currently we do not have this reaction in our photochemical model. However we estimate its effect by doubling the reaction rate of (2.4). As a result, the abundance of C_3H_6 increases by a factor of two and matches the Cassini/INMS observations. In the intermediate altitudes (300 km ~ 600 km), where the CH radicals are rare and where the pressure is too low to drive termolecular combination, photodissociation of C_3H_8 is the dominant process in the production of C_3H_6:

$$C_3H_8 + h\nu \rightarrow C_3H_6 + H_2\,. \tag{2.6}$$

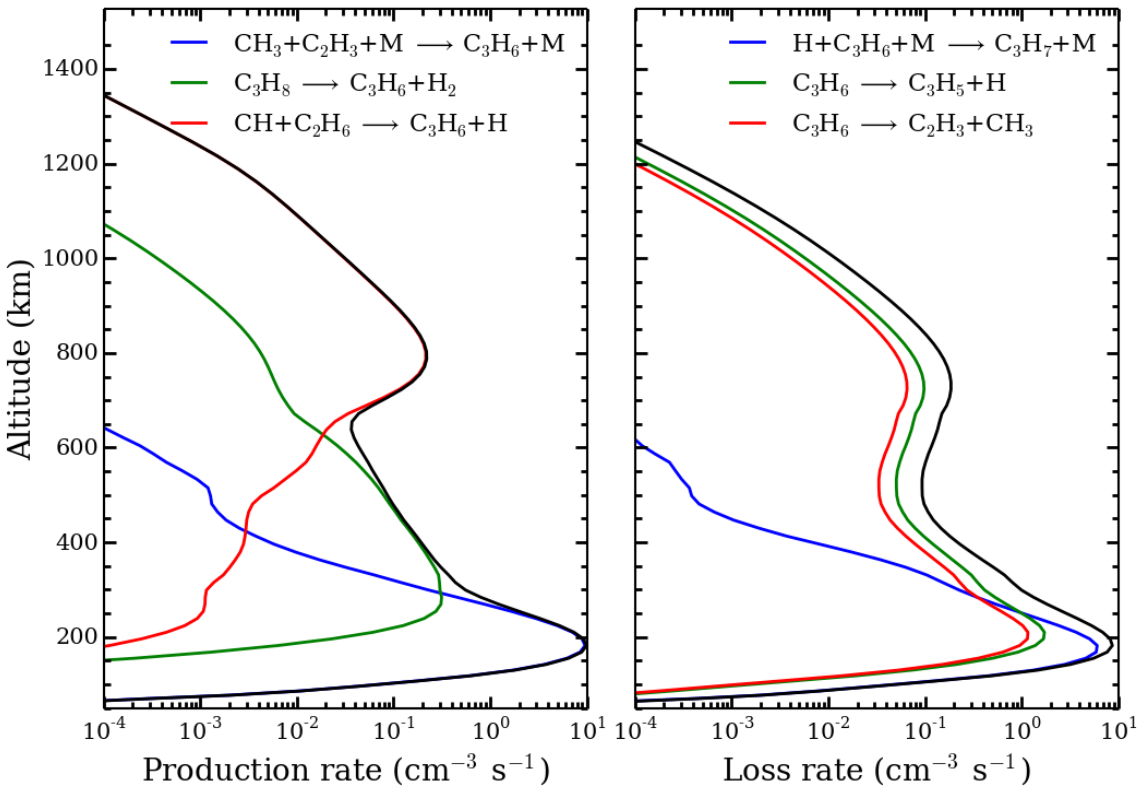

Figure 2.3 Production (left) and loss rates (right) of C_3H_6 due to reactions listed in the figure. The sum of the reactions accounts for more than 90% of the total production and loss rates at each altitude. The total production and loss rates are given by the black lines.

In the stratosphere (< 300 km) where the pressure is high, the three-body reaction

$$CH_3 + C_2H_3 + M \rightarrow C_3H_6 + M\,, \tag{2.7}$$

becomes the dominant production pathway of C_3H_6 and creates the local peak in the mixing ratio as shown in Figure 2.2. Though the production of C_3H_6 peaks at 200 km, our model produces the abundance peak 50 km lower than the production peak. This is probably due to eddy mixing effects because the value of eddy diffusivity at 200km is 2×10^6 cm^2/s, the chemical loss time scale for C_3H_6 at 200 km is 2×10^7s and the expected dynamic

mixing length is $\delta = \sqrt{2 \times 10^6 \times 2 \times 10^7}$ cm $\approx$ 60 km. CH_3 in reaction (2.7) comes from the photosensitized dissociation of CH_4 in the stratosphere (Yung et al., 1984) by:

$$C_2H_2 + h\nu \rightarrow C_2H + H\,, \tag{2.8}$$

$$C_2H + CH_4 \rightarrow CH_3 + C_2H_2\,. \tag{2.9}$$

C_2H_3 in Reaction (2.7) comes from the three-body reaction:

$$H + C_2H_2 + M \rightarrow C_2H_3 + M\,. \tag{2.10}$$

Therefore, the abundance of C_3H_6 in the stratosphere is directly related to the abundance of C_2H_2. Other models fail to produce the abundance of C_3H_6 because they underestimate the stratospheric abundance of C_2H_2 (Hebrard et al., 2013; Krasnopolsky, 2010; Vuitton et al., 2012b; Wilson and Atreya, 2004; Wilson and Atreya, 2009). C_3H_6 is destroyed mainly through photolysis:

$$C_3H_6 + h\nu \rightarrow \alpha(C_3H_5 + H) + \beta(C_2H_3 + CH_3)\,, \tag{2.11}$$

where $\alpha \approx 0.6, \beta \approx 0.4$ are the branching ratios of the photolysis reaction. C_3H_6 can also be destroyed by reacting with an H atom:

$$H + C_3H_6 + M \rightarrow C_3H_7 + M\,. \tag{2.12}$$

The rate of this three-body reaction increases with atmospheric density and becomes greater than the photo-dissociation reaction rate below 300 km (as shown in Figure 2.2).

2.5 Allene (CH_2CCH_2) to methylacetylene (CH_3C_2H) ratio as a probe of H atom abundance

Allene (CH_2CCH_2, or propadiene) and methylacetylene (CH_3C_2H, or propyne) are isomers. Goulay et al. (2009) reported the following branching ratios

$$CH + C_2H_4 \rightarrow CH_2CCH_2 + H \quad (70\%) \tag{2.13}$$

$$\rightarrow CH_3C_2H + H \quad (30\%)\,. \tag{2.14}$$

The enthalpy difference between CH_3C_2H and CH_2CCH_2 is ~1 kcal/mol (Rogers and Mclafferty, 1995). Because it takes very little energy to convert between CH_3CH_2 and CH_2CCH_2, their production and loss rates are expected to be comparable. Using the same algorithm as in section 2.3, their major formation and destruction pathways are calculated and presented in Figure 2.4. In the upper atmosphere, CH_3C_2H and CH_2CCH_2 originate from C_2H_4 and C_3H_5 through:

$$CH + C_2H_4 \rightarrow CH_3C_2H/CH_2CCH_2\,, \tag{2.15}$$

$$H + C_3H_5 \rightarrow CH_3C_2H/CH_2CCH_2 + H_2\,, \tag{2.16}$$

$$CH_3 + C_3H_5 \rightarrow CH_3C_2H/CH_2CCH_2 + CH_4\,. \tag{2.17}$$

Reaction (2.15) terminates near 600 km due to CH_4 self-shielding below 600 km reducing the production rate of CH radicals. Reactions (2.16) and (2.17) persist throughout the entire atmosphere because H atoms and CH_3 are replenished in the lower atmosphere by photosensitized dissociation of CH_4. Reactions (2.16) and (2.17) both lead to the same production rate for CH_3C_2H and CH_2CCH_2, so to explain the non-detection of CH_2CCH_2 Yung et al. (1984) proposed an exchange reaction:

$$H + CH_2CCH_2 \rightarrow CH_3C_2H + H\,, \qquad (2.18)$$

which is exothermic by ~1.6 kcal mol^{-1}. As a result of this exchange reaction, the abundance of CH_2CCH_2 is significantly less than that of CH_3C_2H and their relative abundance equilibrates at a constant ratio as a function of the abundance of H atoms. Figure 2.5 shows the correlation between the mixing ratios of CH_2CCH_2 and CH_3C_2H at several altitudes, as labeled on the correlation curve. From 50 km to 800 km, the mixing ratio of CH_2CCH_2 is equal to 0.2 times that of CH_3C_2H, other than at 150 km to 350 km where the abundance of CH_2CCH_2 increases. The equilibration is a highly sensitive function of the H concentration in the atmosphere, as demonstrated by cracking reactions that can reverse the process of organic synthesis, e.g. Yung et al. (1984). We performed four experiments of the hydrogenation process (Sekine et al., 2008b; Sekine et al., 2008d) with different accommodation coefficients (0, 0.001, 0.01, and 0.1) of H atoms on aerosol particles. As shown in Figure 2.5, the concentration of H atoms in the atmosphere can be inferred from the CH_2CCH_2 to CH_3C_2H ratio, as larger concentrations of H result in lower concentrations of CH_2CCH_2.

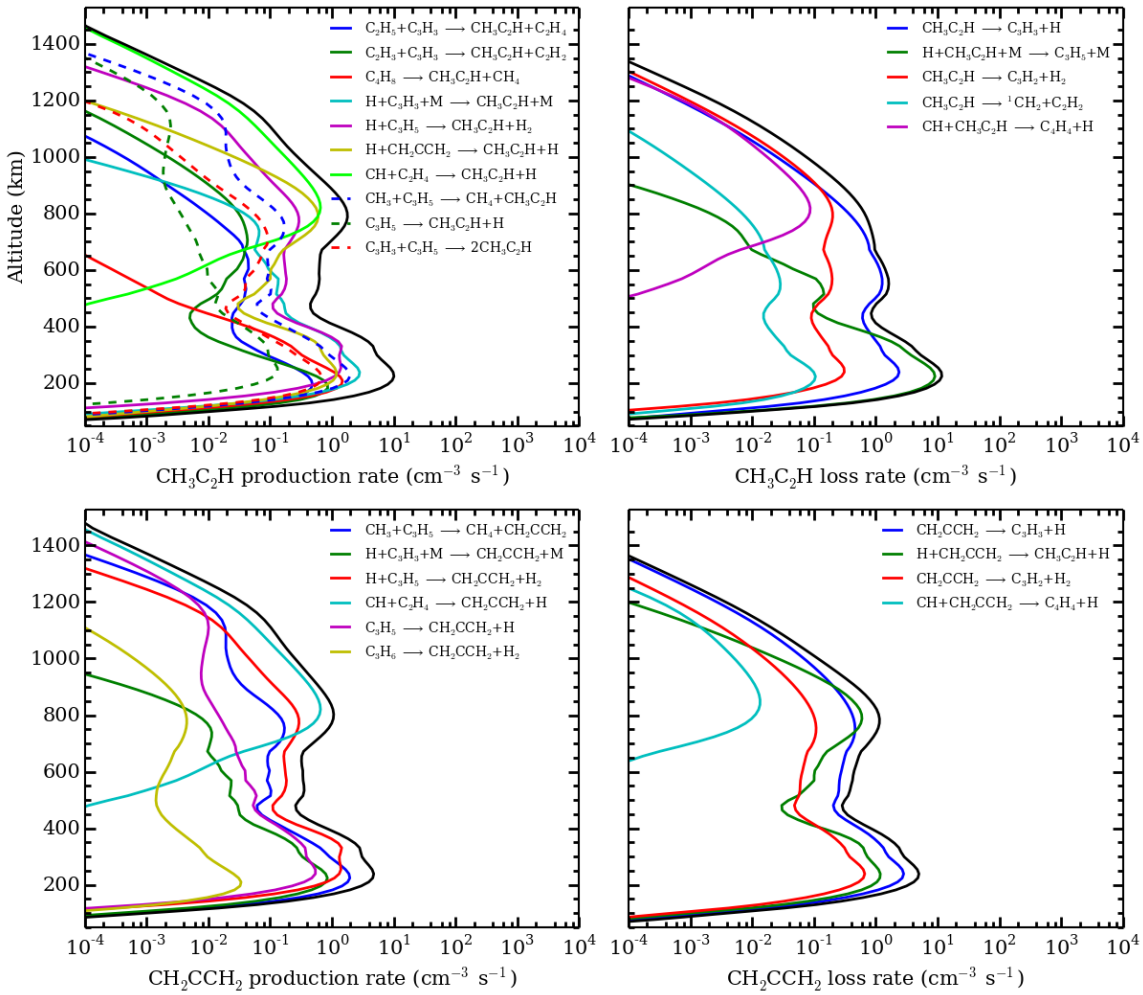

Figure 2.4 Production and loss rates of CH_3C_2H and CH_2CCH_2 due to reactions listed in the figure. The sum of the reactions accounts for more than 90% of the total production and loss rates at each altitude. The total production and loss rates are given by the black lines.

Roe et al. (2011) discussed the challenges of measuring allene in the atmosphere of Titan using extremely high resolution ground-based spectra near 845 cm^{-1} to separate allene lines from ethane lines (this possibility was demonstrated in the upper panel of Figure 12 of (Coustenis et al., 2003)). An upper limit of ~10^{-9} was found, which is an order of magnitude less than that of CH_3C_2H. Nixon et al. (2010) obtained 3σ-upper limits for allene of 0.3x10^{-}

[9] at 100 km and 1.6x10^{-9} at 200 km using Cassini/CIRS. Our model predicts an allene mixing ratio of ~10^{-9} at 200 km, which increases to ~2x10^{-9} at 400 km. These values are consistent with the previous studies and could be confirmed by further measurements given better laboratory spectra. Precise measurements of allene will offer a unique opportunity to probe a very sensitive but hitherto unobserved part of the atmospheric chemistry of Titan.

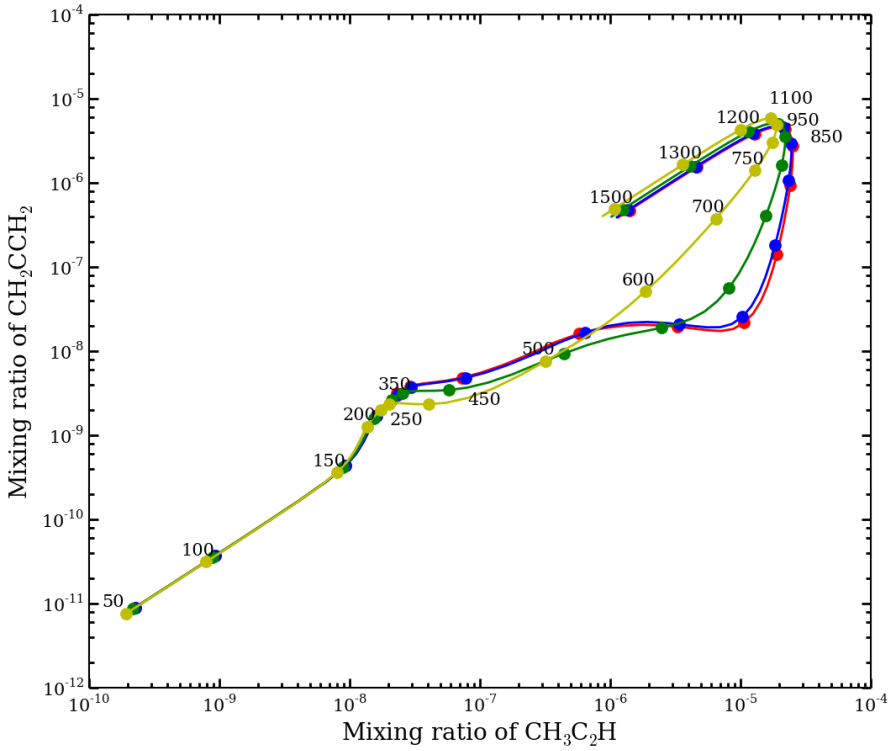

Figure 2.5 Correlation between CH_3C_2H and CH_2CCH_2 with accommodation coefficients of 0 (red), 0.001 (blue), 0.01 (green), and 0.1 (yellow) for H on aerosol particles. The numbers labeling the points indicate the altitude in Titan's atmosphere in km.

2.6 Estimated abundance of cyclopropane (c-C_3H_6)

Figure 1 of Nixon et al. (2013) raises the possibility of c-C_3H_6, which is an isomer of propene. This molecule has not been detected in the atmosphere of Titan. Reaction (2.4) primarily produces C_3H_6, while the branch producing the isomer c-C_3H_6 is considered to be exceedingly slow (Galland et al., 2003). No published yield for c-C_3H_6 is available, though we can estimate a yield ~ 1% relative to C_3H_6 or C_3H_8 from the discharge experiments of Navarro-González and Ramírez (1997). Thus, we would estimate c-C_3H_6 concentrations in the atmosphere of Titan to be a hundred times less than those of C_3H_6.

2.7 Conclusions

Our model reproduced the abundances of C_2-hydrocarbons and the newly observed C_3H_6 in the atmosphere of Titan. The model also shows that CH_2CCH_2 is in equilibrium with its isomer CH_3C_2H by a constant ratio, which is a strong function of the abundance of H atom in the atmosphere. The abundance of CH_2CCH_2 is close to the detection limit. It is possible that further analysis of Cassini/CIRS limb-view observations combined with better laboratory constraints on the spectra of CH_2CCH_2 will lead to its detection, which would fill another gap in the C_3-hydrocarbon family. The observed mixing ratio of CH_3C_2H is 10^{-8}, while our calculated mixing ratio for CH_2CCH_2 in the stratosphere is about 10^{-9}. Confirmation or rejection of this value requires improved laboratory spectral data. Finally, c-C_3H_6 is not likely to be observed due to its low abundance (~10^{-11}).

Chapter 3 Moist convection in hydrogen atmospheres and the frequency of Saturn's giant storms

Cheng Li and Andrew P. Ingersoll

Division of Geological and Planetary Science, California Institute of Technology, Pasadena, CA, 91125

Published in modified form in *Nature Geosicence*, 8, 398-403, 2015

3.1 Abstract

A giant planet-encircling storm occurred on Saturn on Dec. 5th, 2010 at planetographic latitude 37.7ºN. It produced intense lightning, created enormous cloud disturbances and wrapped around the planet in six months. Six such storms, called Great White Spots, have erupted since 1876. They have alternated between mid-latitudes and the equator at intervals ranging from 20 to 30 years. The reason for the intermittent explosion is hitherto unclear and there are no similar storms on brother Jupiter. Here we describe the water-loading mechanism, which could suppress moist convection for decades due to the larger molecular weight of water in a hydrogen-helium atmosphere. We show that this mechanism requires the deep water vapor mixing ratio to be greater than 1.0%, which implies O/H at least 10 times the solar value. Observations imply that Saturn's atmosphere is more enriched in water than Jupiter, which could explain why Saturn has such storms and Jupiter does not. We further use a two-dimensional axisymmetric dynamic model and a top-cooling convective adjustment scheme to connect our theory to observation. We show that for a deep water vapor mixing ratio of 1.1%, the ammonia vapor is depleted down to 6 bars, the tropospheric warming is ~6 K, and the interval between two consecutive storms at one latitude is ~70 years. These values are consistent with observations.

3.2 Introduction

Saturn's giant storms occurred 6 times in the past 140 years (Sanchez-Lavega, 1994). They are like thunderstorms on Earth (Sanchez-Lavega and Battaner, 1987), except that the storm itself is about the size of Earth. The Cassini spacecraft has arrived at a privileged time to capture the most recent outburst, returning fruitful close observations. Features in common with terrestrial thunderstorms include the observed cloud disturbance (Sanchez-Lavega et al., 2011; Sayanagi et al., 2013), lightning discharges (Fischer et al., 2011) and tropospheric warming (Achterberg et al., 2014). What makes the storm more mysterious is the observed depletion of ammonia vapor in the wake of the storm down to several bars (Janssen et al., 2013; Laraia et al., 2013). One might think that an upward transport of ammonia vapor during moist convection would saturate the atmosphere, but apparently it does not. Such post-storm ammonia depletion was also detected in Saturn's southern hemisphere lightning storms (Dyudina et al., 2007), which are much smaller in size.

Moist convection on giant planets differs from that on Earth in three major respects. First, the density of moist air on giant planets is greater than that of dry air. Second, convection in a giant planet atmosphere is controlled by cooling at the top rather than by heating at the bottom. Third, the radiative time scale is on the order of decades. The molecular weight loading of relatively dense condensates will hinder the upward motion of moist parcels and reduce the intensity of convection, which is verified both by a one-dimensional diagnostic calculation (Stoker, 1986) and by a three-dimensional plume model (Hueso and Sanchez-Lavega, 2004). For a sufficiently large mixing ratio of condensates, Guillot (1995) proposed a steady state solution for the heat transfer in giant planet atmospheres in which

the gradient of mean molecular weight leads to a stable super-adiabatic temperature profile. However, whether the atmosphere could reach such a steady state highly depends on the poorly constrained optical opacities near the cloud bottom, and the regular outburst of giant storms in Saturn's atmosphere suggest that this steady state is probably not obtained (see section 3.7.8 for further discussion of this topic). Sugiyama et al. (2011) and Sugiyama et al. (2014) find a quasi-periodic behavior of convection on Jupiter due to the destabilization of a stable layer by the re-evaporation of condensates. Here we investigate a new mechanism, which would give rise to cyclic explosions of giant storms on the time scale of decades without the re-evaporation of condensates.

In our model, there are three phases to the cycle of a giant storm. The first phase, described in section 3.3, is inhibition of convection by the water loading effect and its eventual release. We describe the thermodynamic properties of Saturn's atmosphere and identify the same critical water mixing ratio as Guillot (1995) that would lead to convective inhibition. The second phase is the rapid adjustment to geostrophic balance following the convective event, and is described in section 3.4. There we develop a two-dimensional axisymmetric numerical model to test our theory against observations of ammonia depletion after the storm. The third phase is the slow cooling of the atmosphere (section 3.5) for which we use a moist convective adjustment scheme to calculate the time interval between storms. Because the first two phases take place over 30 hours and the third phase takes place over 70 years, treating them in a single numerical model is impractical and is beyond the scope of this chapter. Section 3.6 concludes and section 3.7 gives a thorough

discussion on the numerical method, sensitivity tests, radiative heat transfer near the cloud base and isobaric mixing across temperature discontinuity.

3.3 Convective inhibition

As temperature is inversely proportional to the density of a dry air parcel, virtual temperature (T_v) has been used as a convenient variable that is inversely proportional to the density of a moist air parcel. T_v is defined as

$$T_v = T\frac{1+\eta}{1+\epsilon\eta}, \tag{3.1}$$

where η is the mole mixing ratio of water (number of water molecules to the number of molecules of hydrogen-helium mixture) and ϵ is the mass ratio of the condensate to the dry air. Consequently, the ideal gas law for the moist air can be written as $P = \rho R_d T_v$, where R_d is the gas constant for dry air. For Saturn's atmosphere, $\epsilon = 18/2.2 = 8.1$. Since the factor $(1+\eta)/(1+\epsilon\eta)$ is less than one, a moist parcel on Saturn is heavier than a dry parcel with the same temperature, which is opposite to the situation on Earth.

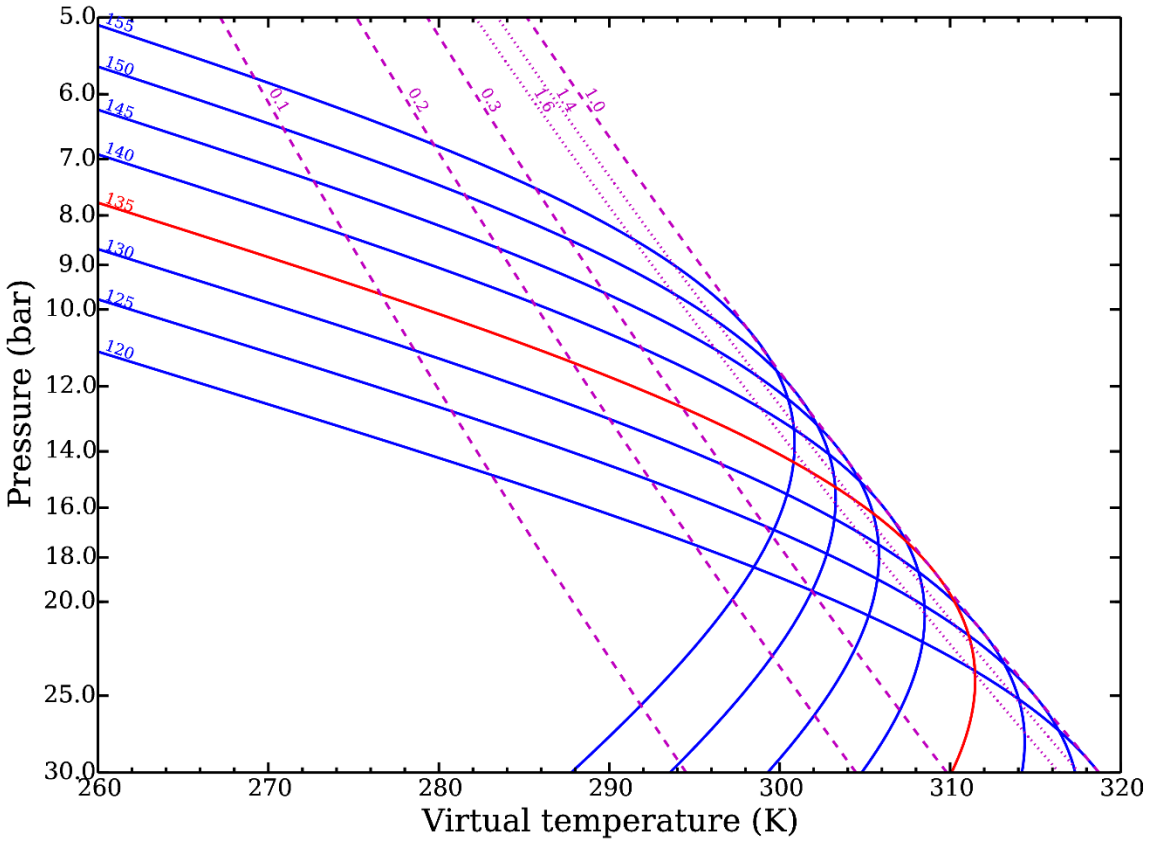

Figure 3.1 Virtual temperature of moist adiabats. The solid curves show the virtual temperature versus pressure for moist adiabatic profiles. The temperature in K at 1 bar level for each moist adiabat is indicated above the line. Dashed/dotted lines show the contours of mixing ratio below/above 1.0% . Mixing ratios are labeled in units of %. The water mixing ratio on a moist adiabatic profile is indicated by the dashed line when it is less than 1.0% and is indicated by the dotted line when it is larger than 1.0%.

We first assume that the temperature profile of Saturn's troposphere follows a moist adiabat, based on the fact that convection usually brings the temperature profile close to the moist adiabat in Earth's tropics. The amount of water vapor (η) is controlled by the saturation vapor pressure $e(T)$ through the ideal gas form of the Clausius-Clapeyron relation:

$$\frac{de}{dT} = \frac{eL}{R_w T^2}, \eta = \frac{e}{p - e}. \qquad (3.2, 3.3)$$

We calculate the virtual temperature profiles of several moist adiabats in Figure 3.1. These curves show that the virtual temperature reaches a maximum value when the water mixing ratio in the parcel equals 1.0% (note that the mixing ratio lines increase to the left when the water mixing ratio is larger than 1.0%). Below this critical mixing ratio, the temperature dominates the density, i.e. virtual temperature increases with temperature; above, the exponential growth of the moisture's mass overwhelms the temperature, causing virtual temperature to decrease as temperature increases. This critical mixing ratio (η_c) can be obtained analytically by maximizing equation (3.1) holding p = constant and using the constraints from equations (3.2, 3.3):

$$\eta_c = \frac{1}{(\epsilon - 1)\frac{L}{R_v T_b} - \epsilon} \approx 1.0\%. \qquad (3.4)$$

We have chosen $T_b \approx 330\,K$, which is the approximate temperature at the cloud base. When $\eta > \eta_c$, there may be two moist adiabats, a warm one and a cold one, differing by an amount ΔT, that have the same T_v (density) at cloud base.

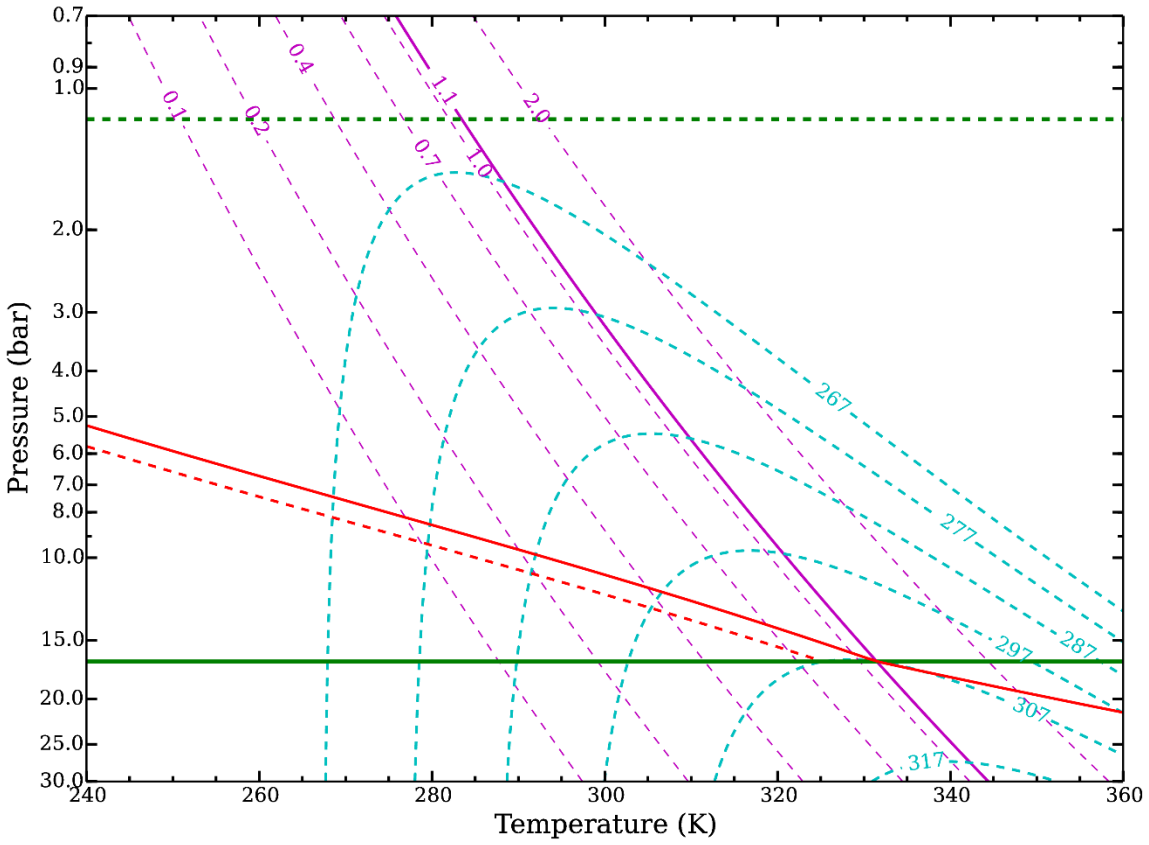

Figure 3.2 Thermodynamic diagram for Saturn's atmosphere. The dashed and solid horizontal green lines are the bottoms of ammonia and water cloud, respectively. The solid red line shows the warm adiabat; the part above the solid green line is the moist adiabat; the part below the solid green line is the dry adiabat. The dashed red line shows the cold adiabat that has the same virtual temperature at the cloud base as the warm one. The cyan lines show the contours of constant virtual temperature. The magenta lines show the contours of constant mixing ratio with 1.1% marked by a solid line.

The thermodynamic diagram for Saturn's atmosphere is plotted in Figure 3.2. Assume that the deep water mixing ratio is supercritical as in equation (3.4) and the troposphere is cooling by radiation from a warm moist adiabat (the solid red line) to the cold moist adiabat (dashed red line) that has the same T_v at cloud base as the warm adiabat. When the tropospheric temperature is between these two adiabats, its T_v is greater, meaning that its density is less. This low density layer floating above the dense deep atmosphere establishes

a stable stratification at cloud base, which inhibits convection and decouples the interior from the troposphere (temperature below the cloud base remain fixed). Convection from below is suppressed as long as the stable stratification exists, allowing convective available potential energy (CAPE) to accumulate. If radiative heat transfer is smaller than the cooling at the top, this stable layer will persist as the tropospheric temperature decreases due to loss of heat at the top, (see section 3.7.8 for a discussion of the situation when this assumption fails). As the troposphere cools, the density just above cloud base first decreases due to the unloading of high-mass molecules by precipitation, creating a stable interface with the fluid just below cloud base. The cooling is slow because the radiating temperature is low and the heat capacity of the atmospheric column is high. The stable stratification disappears when the T_v above cloud base is the same as that below it (the tropospheric adiabat approaches the dashed red line). Mixing across the temperature discontinuity hastens this process by a small amount (see section 3.7.2). When the convective inhibition vanishes, the warm moist parcel rises from the deep interior, releasing the stored CAPE. The parcel is accelerated by the buoyancy difference between the warm adiabat and the cold adiabat, releasing latent heat as it condenses. Finally, the surrounding atmosphere is warmed back to the same temperature as the warm adiabat by compensating subsidence, and the cycle repeats. Radiative cooling and convective heating force the system to oscillate between these two adiabats (the solid and dashed red lines).

If the water mixing ratio is 1.1%, a crude estimate of the cooling time from the warm adiabat to the cold one is (radiative cooling flux is taken to be 4.5 W/m^2 (Orton and Ingersoll, 1980)):

$$t \approx \frac{c_p \Delta p \Delta T}{Flux \times g} \approx \frac{(1.3 \times 10^4) \times (20 \times 10^5) \times (5)}{(5) \times (365 \times 86400) \times (10)} \approx 70 \text{ years} . \quad (3.5)$$

A more sophisticated and precise calculation of the cooling time is provided in section 3.5.

To get the cyclic behavior, the deep water vapor mixing ratio has to be greater than 1.0%, which is 10 times solar, given a solar O/H ratio (Asplund et al., 2009) of 4.90×10^{-4}. This enrichment factor is consistent with that for carbon (Fletcher et al., 2009b; Fletcher et al., 2012) and phosphorus (Fletcher et al., 2009a) on Saturn. The Galileo probe (Niemann et al., 1996) demonstrates that the heavier elements (C, N, P) in Jupiter are enriched by $2 \sim 5$ times with respect to their solar values. If the water on Jupiter is also $2 \sim 5$ times solar, it is not enough to trigger the water-loading mechanism. That is probably the reason why we have observed the giant storms on Saturn but not on Jupiter.

3.4 Geostrophic adjustment

After the warm parcel rises from the deep interior, it gains kinetic energy and overshoots into the stratosphere. The warm convective tower is not stable and will rebound back to a geostrophically balanced state in which the outward pressure gradient force is balanced by the Coriolis force associated with an azimuthal flow. Here we develop a two-dimensional axisymmetric numerical model to investigate the large scale geostrophic adjustment process. The model solves the primitive equations in radius and log-pressure coordinates. This is a valid approximation because the horizontal scale of the phenomenon is ~5000 km (Figure 3.3 and Figure 3.4), which is much greater than the vertical scale. The background atmospheric temperature profile ($\bar{T}$) is the cold adiabat, because it is on the margin to start convection. We assume that the cold adiabat connects to the Voyager temperature profile (Lindal et al., 1985) at 1 bar. The initial temperature distribution (T) is a Gaussian in radius with maximum temperature equal to the warm adiabat (T_w).

$$T(r,z) = \bar{T}(z) + [T_w(z) - \bar{T}(z)]\exp(-r^2/r_0^2)\,, \tag{3.6}$$

where r, z are radial and vertical coordinates; r_0 defines the width of the rising plume. The atmosphere is initially at rest. During the adjustment, water and ammonia are removed from the system when they condense, and the release of latent heat is added to the thermodynamic equation. Other details of the model are described in section 3.7.3. The temperature of the warm adiabat $T_w(z)$ is a function of the deep water mixing ratio η. Different choices of η and r_0 do not change the qualitative manner of the results, as long as the deep water vapor mixing ratio is above 1%. We will describe the results using the

parameters that match the observations best, $\eta = 1.1\%$ and $r_0 = 200$ km, and leave the discussion of other parameters in section 3.7.4.

Figure 3.3 shows the equilibrated azimuthal wind and temperature anomalies. The azimuthal wind displays a 5000 km wide anticyclonic structure with maximum speed of 75 m/s near the tropopause. These values are consistent with the observed cloud morphology and wind speed in the storm's head (Sayanagi et al., 2013). As a result of the convective heating, the tropospheric temperature has been warmed by 6 K and the warming decreases with the radial distance. The lateral temperature gradient balances the anticyclonic vortex through the thermal wind relation. The lower stratospheric temperature decreases by 6 K around 100 mbar as observed from the Cassini/CIRS spectroscopy (Achterberg et al., 2014; Fletcher et al., 2011), which reflects the adiabatic upward motion in the lower stratosphere.

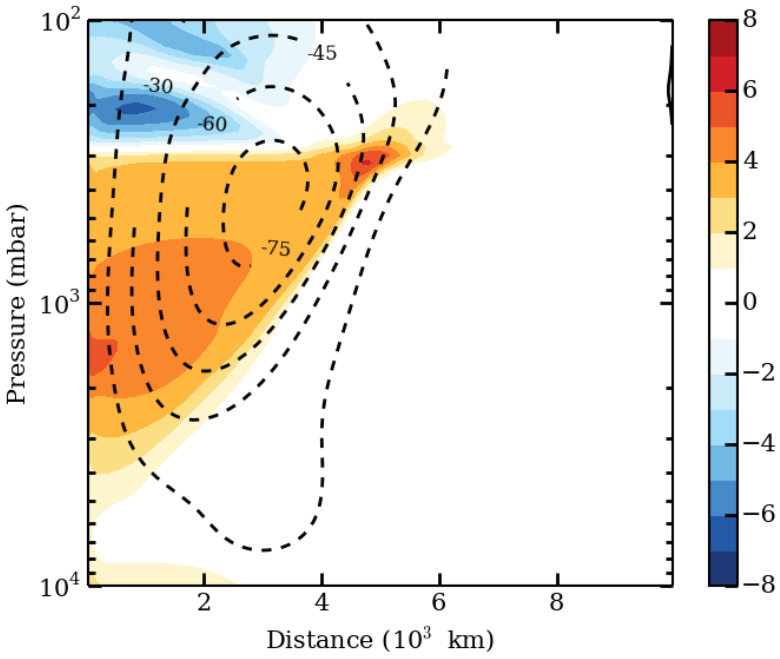

Figure 3.3 Residual azimuthal wind and temperature anomaly after geostrophic adjustment. Wind (dashed contours) is measured in m/s. Negative wind speed denotes clockwise (anticyclonic) flow in the northern hemisphere. Temperature anomaly (colored contours) is defined as $T(r,z) - \bar{T}(z)$. x-axis is the radial distance; y-axis is the pressure.

The geostrophic adjustment process and evolution of ammonia vapor are displayed in Figure 3.4 at six time steps. The adjustment process encompasses three major stages: First (Figure 3.4 a, b), the unbalanced pressure gradient force causes the warm convective tower to expand outward, which is compensated by upward motion in the tower (solid gray contours). The ammonia vapor has been advected to the cold upper troposphere and precipitates out. Second (Figure 3.4 c, d), the circulation in the vertical/radial plane reverses and advects ammonia vapor from the upper troposphere to the deep troposphere along a dry adiabat (dashed gray contours). Because some ammonia has been precipitated in the first stage, the dry adiabatic warming during the reverse circulation creates low ammonia relative humidity. Third (Figure 3.4 e,f), the circulation oscillates between the positive (outward) and the negative (inward) phase in the subsequent time and reaches a steady state with depleted ammonia vapor. The averaged mixing ratio of ammonia and water over the width of the anticyclone are plotted in Figure 3.5 b, which shows that ammonia vapor is depleted down to 6 bars.

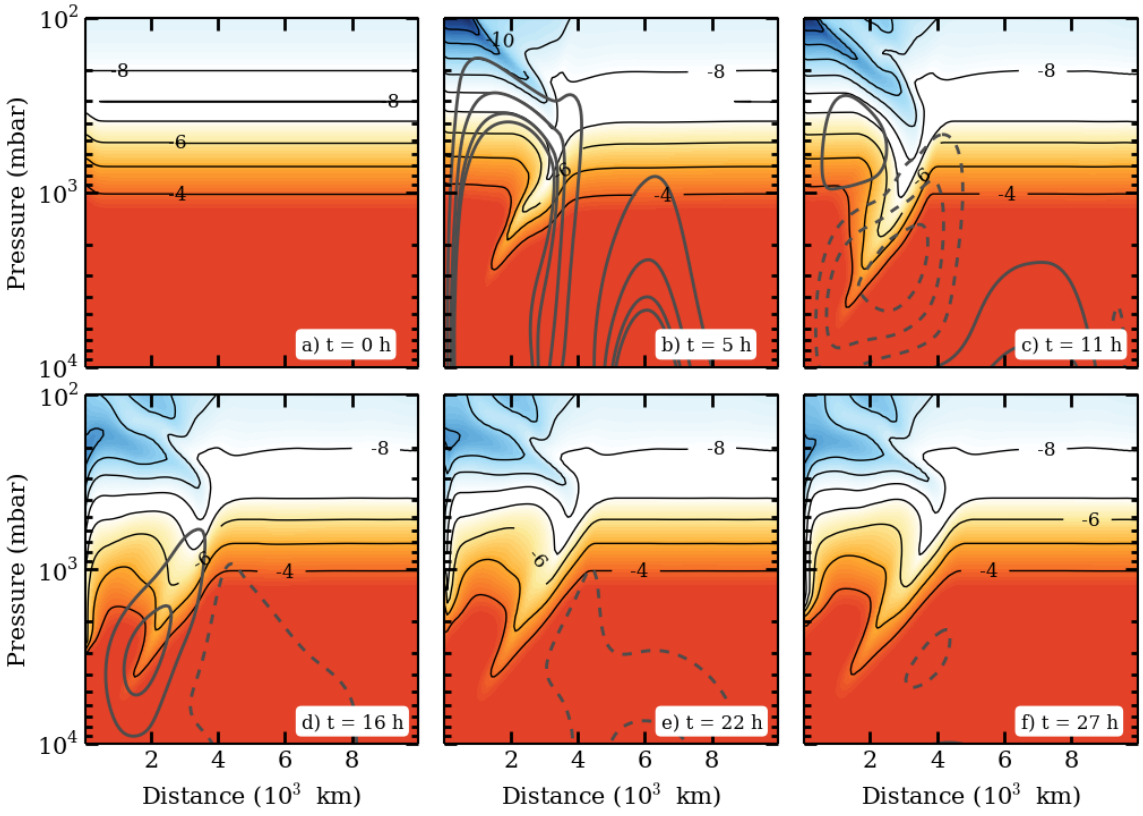

Figure 3.4 Time evolution of ammonia vapor mixing ratio and the streamfunction. Time is indicated at the bottom right corner increasing from panel (a) to panel (f). Colored contours show the mole mixing of ammonia vapor labeled by the exponent in base 10. Gray contours are the radial-vertical mass streamfunctions; solid ones represent clockwise circulation and are drawn from 10^{12} kg/s to 7×10^{12} kg/s at intervals of 2×10^{12} kg/s; dashed ones represent counterclockwise circulation and are drawn from -7×10^{12} kg/s to -10×10^{12} kg/s at intervals of 2×10^{12} kg/s.

3.5 Radiative cooling

In this section, we investigate a convective adjustment scheme that describes the cooling phase of the atmosphere due to thermal radiation at the top. The time interval between two giant storms is estimated to be ~70 years, and we have chosen the deep water vapor mixing ratio η to be consistent with this estimate. The detailed numerical method to calculate these profiles are provided in section 3.7.6. We give an overview in the paragraphs below.

After geostrophic adjustment, the atmosphere is unsaturated and stable with respect to convection. As cooling proceeds, the atmosphere separates into four layers, numbered 1 to 4 from top to bottom. Layer 1 follows a saturated moist adiabat. Radiative heat loss from the top of the atmosphere drives convection in layer 1 and causes it to cool. Layer 2 follows an unsaturated dry adiabat, and the constituents there are well mixed. Because both layers are convecting, temperature and mixing ratios are continuous at the boundary between layers 1 and 2. Cooling of layer 1 and re-evaporation of precipitation from layer 1 drive convection in layer 2. Layer 3 is the stable primordial layer, which is undisturbed since the time of the geostrophic adjustment that followed the last giant storm. The existence of layer 2 ensures that no precipitation falls into layer 3. The boundary between layers 2 and 3 is called the interface; it moves downward as the cooling proceeds. Temperature and mixing ratios could be discontinuous at the interface if the mass loading effect ensures the interface to be stable. Layer 4 is the deep interior, which is assumed to follow a dry adiabat with fixed temperature and fixed mixing ratios for all constituents.

In our calculation, the interface between layers 2 and 3 moves down through successive grid boxes as a two-step process. The entrainment step moves the interface down by one grid box, whose contents become part of layers 1 and 2. Their profiles adjust to conserve column integrated enthalpy and moisture. After the entrainment step, the interface is stable and the slow cooling step begins. The cooling step is driven by radiation from the top. Column integrated enthalpy is reduced, but moisture is conserved. The cooling time is calculated from the energy loss by radiation assuming a constant flux of 4.5 W m^{-2} (Orton and Ingersoll, 1980). The cooling step ends when the interface is neutrally stable and convection is about to begin. This initiates the entrainment step on the next grid box, and the cycle repeats. Eventually the interface reaches the deep interior and the parcel rising from the deep interior initiates another giant storm.

Figure 3.5 shows a snapshot during the cooling process that is close to initiating another giant storm. It might seem counterintuitive that the vertical potential temperature profile evolves to lower values than the cold adiabat. This occurs because the troposphere is cooling from the top down, with an initial profile that is unsaturated and stable. When the initial state from which the atmosphere starts to cool is unsaturated, the top cooling process will redistribute the water vapor in layers 1-3 and saturate the atmosphere. Thus, the amount of water in layers 1-3 after the geostrophic adjustment determines the temperature profile below which the atmosphere is fully saturated. If this minimum temperature profile is higher than the cold adiabat (i.e., if the atmosphere becomes saturated before it reaches the cold adiabat), then our analysis in section 3.3 applies. Otherwise, the temperature

profile cools beyond the cold adiabat (Figure 3.5 a) before the interface becomes unstable, because the amount of water in layers 1-3 is less than the cold adiabat.

3.6 Conclusion

Moist convection on Earth are categorized into two types (Emanuel et al., 1994). Quasi-equilibrium convection acts continuously and is in quasi-equilibrium with its environment. Triggered convection emphasizes the large amount of CAPE that accumulates when the atmosphere is stable for a small amplitude disturbance but unstable for a sufficiently large one (i.e. when it is conditionally unstable) (Charney and Eliassen, 1964). Both quasi-equilibrium and triggered types of convection exist on Saturn. The former applies to the long time radiative cooling and the latter applies when the convective inhibition layer is broken. Many features of Saturn's giant storms still remain unexplained. First, most of the storms have occurred in the northern hemisphere during northern summer, although it might be a statistical fluke (see section 3.7.7). Second, they have occurred at the extrema of the zonal jets. Third, each one stayed confined within its own jet and didn't spread into the oppositely-directed neighboring jets. This is just a partial list. In this work, we show that convection on Saturn would be episodic instead of continuous if the deep water mixing ratio were greater than 1.0%. The best estimation is 1.1%.

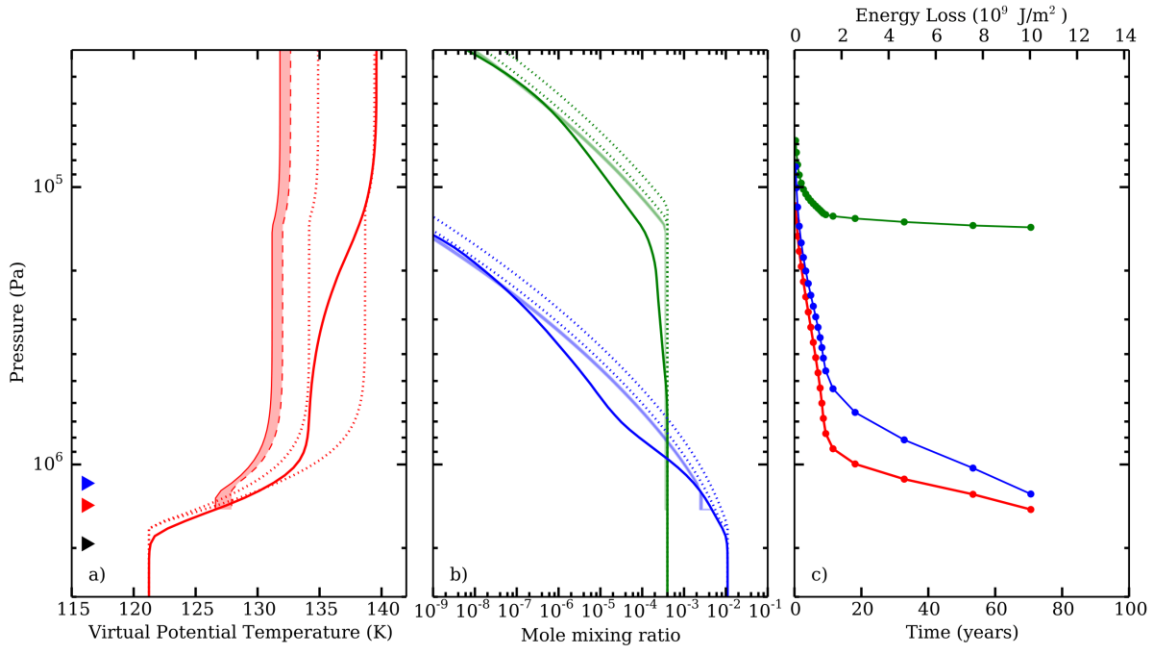

Figure 3.5 Evolution of Saturn's atmospheric temperature and minor constituents. Shaded regions represent one cooling step from right (the profile after the preceding entrainment step) to left (the profile before the next entrainment step). (a) Two dotted lines: the cold and warm moist adiabats as those in Figure 3.2. Thick solid red line: the virtual potential temperature profile after the geostrophic adjustment. Blue, red and black triangles: the bottom of layers 1, 2 and 3. (b) Mole mixing ratio of ammonia (green) and water (blue) vapor. (c) Evolution of ammonia (green), water (blue) cloud base and the interface (red).

3.7 Appendix

3.7.1 Method to solve the primitive equations

The primitive equation is provided in section 3.7.3. The numerical method used to solve the primitive equations is the finite volume method (LeVeque, 2007). Spatial fluxes are reconstructed by the third order ENO (essential non-oscillatory) scheme (Shu and Osher, 1989) with Riemann solver being Roe's linearization method (Roe, 1997).

Hyperviscosity is not required. The discretized equations march forward in time by the Strong Stability Preserving third order Runge-Kutta scheme (Shu, 1988). Therefore, the numerical solution is third order accurate both in space and time. The standard resolution is 128×128, corresponding to 78 km in the horizontal and 3.1 km in the vertical. We have performed a series of resolution dependent tests. The results agree qualitatively and the quantitative differences are summarized in Table 3.1.

Table 3.1 Resolution dependent test for solving the axi-symmetric primitive equation

Resolution	**Azimuthal wind (m/s)**	**Min T (K)**	**Max T (K)**
64x64	56.8	-6.6	7.3
128x128	81.1	-6.5	8.1
256x128	83.6	-8.1	8.4

3.7.2 Isobaric mixing across temperature discontinuity at the cloud bottom

In section 3.3 we discussed convective inhibition due to the mass loading effect: As the troposphere cools, the density just above cloud base first decreases due to the unloading of

high-mass molecules by precipitation, creating a stable interface with the fluid just below cloud base. Further cooling reverses this trend, and the stable layer disappears. The question arises, would mixing across the interface hasten the disappearance, thereby destroying the convective inhibition? Because linear mixing between two points on a convex saturation curve produces an over-saturated parcel, the conserved quantities of the mixing process are the total mass and the moist enthalpy (Emanuel, 1994) defined by

$$h = C_p T + L_v \eta^*(T)\epsilon \,, \tag{3.7}$$

where $\eta^*(T)$ is the saturation water mixing ratio at temperature T . We let f and $1 - f$ be the fractions of upper- and lower-layer fluid in the final mixture, respectively. Since f is unknown, we consider the full range from $f = 0$ to $f = 1$. The temperature of the mixture (T_m) is solved by the equation

$$f\left[C_p T_1 + L_v \eta^*(T_1)\epsilon\right] + (1-f)\left[C_p T_2 + L_v \eta^*(T_2)\epsilon\right] = C_p T_m + L_v \eta^*(T_m)\epsilon \,, \tag{3.8}$$

where T_1 is the temperature above the interface; T_2 is the temperature below the interface; T_m is the temperature of the mixture. As described in section 3.3, the density variable that determines the stability is the virtual temperature. Let the subscript $(\quad)_v$ stand for virtual temperature. If $T_{mv} > T_{2v}$, the mixture is stable with respect to the air beneath it. If $T_{mv} < T_{1v}$, the mixture is stable with respect to the air above it. Therefore, the mixture is totally stable if

$$T_{1v} > T_{mv} > T_{2v} \,. \tag{3.9}$$

We have considered the mass loading of extra liquid water in the mixture. The temperature T_2 below the interface does not change, but T_1 varies from the warm adiabat (332 K) to the cold adiabat (325 K). We display the value of $T_{mv} - T_{1v}$ and $T_{mv} - T_{2v}$ in Figure 3.6.

At the start of the radiative cooling phase, we find that the mixture is always less dense than the fluid below the interface and more dense than the fluid above it, meaning that the interface is stable. However, near the end of the cooling phase the mixture is less dense than the fluid above, and the interface is unstable. Depending on the value of *f*, which is unknown, this could hasten the onset of convection and decrease the time between giant storms by up to 25%. Given the other uncertainties, such as the water vapor mixing ratio at depth, the 25% decrease has no significant effect on the model results.

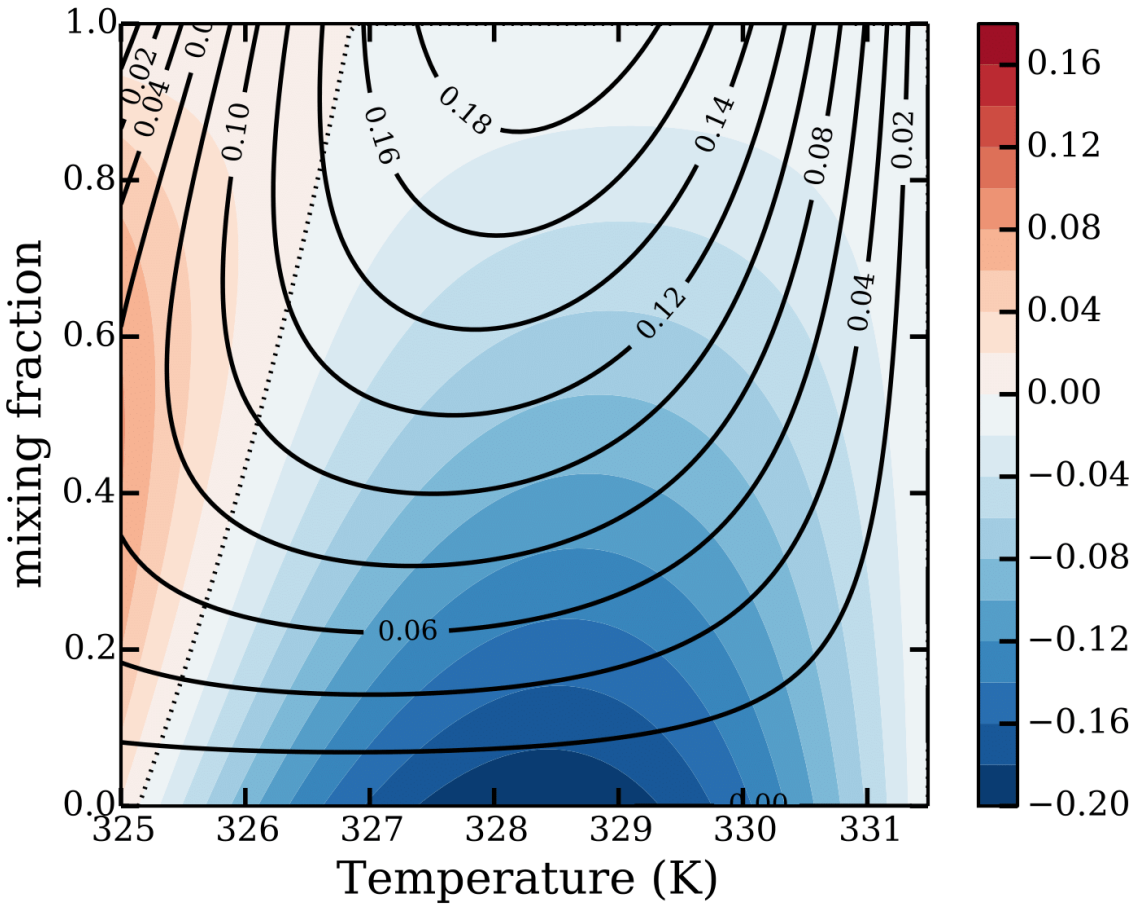

Figure 3.6 Mixing diagram across the temperature discontinuity at the cloud base. X-axis is the temperature above the cloud base (T_1) and y-axis is the fraction of the parcel coming from the top (f). The lower and upper limits of the temperature axis are chosen to be the temperature of the cold and the warm adiabats at the cloud base. The solid curves show $T_{mv} - T_{2v}$, which is always positive. The colored contours show $T_{mv} - T_{1v}$, which is positive (red) to the left and negative (blue) to the right. The mixture is stable (unstable) with respect to the atmosphere above cloud base in the blue (red) zones, respectively.

3.7.3 Details about the numerical model

The axisymmetric primitive equations in log-pressure coordinates are:

$$\frac{\partial u}{\partial t} + u\frac{\partial u}{\partial r} + w\frac{\partial u}{\partial z} - \frac{v^2}{r} - fv = -\frac{\partial \phi}{\partial r} + K_{xx}\nabla^2 \mathrm{u}\,, \tag{3.10}$$

$$\frac{\partial v}{\partial t} + u\frac{\partial v}{\partial r} + w\frac{\partial v}{\partial z} + \frac{uv}{r} + fu = K_{yy}\nabla^2 v\,, \tag{3.11}$$

$$\frac{\partial \theta}{\partial t} + u\frac{\partial \theta}{\partial r} + w\frac{\partial \theta}{\partial z} = \theta\frac{\sum_i L_i \epsilon_i \dot{q}_i}{C_p T}\,, \tag{3.12}$$

$$\frac{\partial \eta_i}{\partial t} + u\frac{\partial \eta_i}{\partial r} + w\frac{\partial \eta_i}{\partial z} = -\dot{q}_i\,, \tag{3.13}$$

$$\dot{q}_i = \frac{\partial}{\partial t}[\eta_i - min(\eta_i,\ \eta_i^*)]\,, \tag{3.14}$$

$$\frac{\partial \phi}{\partial z} = \frac{RT_v}{H_0} = g\frac{T}{T_0}\frac{1+\sum_i \eta_i}{1+\sum_i \epsilon_i \eta_i}\,, \tag{3.15}$$

$$T = \theta\left(\frac{p}{p_0}\right)^{\frac{R_d}{C_p}} = \theta\exp\left(-\frac{gz}{C_p T_0}\right), \tag{3.16}$$

$$\frac{1}{r}\frac{\partial}{\partial r}(ru) + \frac{\partial w}{\partial z} - \frac{z}{H_0} = 0\,, \tag{3.17}$$

$$\frac{\partial \psi}{\partial z} = -\rho_0 ru\exp\left(-\frac{z}{H_0}\right), \frac{\partial \psi}{\partial r} = \rho_0 rw\exp\left(-\frac{z}{H_0}\right), \tag{3.18}$$

where u, v, w are radial, azimuthal and vertical winds. θ, T, T_v are potential temperature, temperature and virtual temperature. ψ is the mass streamfunction; $\rho_0 = 1$ kg/ m^3.$L_i, \epsilon_i, \eta_i, \eta_i^*, \dot{q}_i$ are microphysical variables. They represent the latent heat, molecular mass ratio to dry air, mole mixing ratio, saturation mixing ratio and condensation rate for

condensable species *i* (*i* = NH_3, H_2O), respectively. R_d, C_p are the gas constant and specific heat capacity for dry air. $T_0, H_0 = R_d T_0/g$ are the temperature and density scale height at $p_0 = 1$ bar. r, z are the radial distance and log-pressure coordinate: $z = H_0 \ln \frac{p_0}{p}$. ϕ, g are the geopotential height and gravity. Eddy viscosity K_{xx}, K_{yy} are included in the momentum equations to damp out the energy. Since their values are unknown, we choose a small enough value ($K_{xx}/\Delta x^2 = K_{yy}/\Delta y^2 = 3 \times 10^{-3}$) to both maintain numerical stability and damp out the energy. Any value larger than the current one will result in a decrease of the azimuthal wind and the cooling time. Boundary conditions are applied such that pressure gradient vanishes ($\phi = 0$) at the lower boundary and the vertical velocity vanishes ($w = 0$) at the upper boundary due to the strong stratification of the stratosphere (Achterberg and Ingersoll, 1989). We have moved the lower (upper) boundary low (high) enough to minimize the effects of boundary conditions. Currently, the lower boundary is 30 bars and the upper boundary is 10 mbar. The positions of lower and upper boundary have negligible effects on the result when the lower boundary is placed deeper than 25 bars and the upper boundary higher than 50 mbar. The largest radial distance in the model is 10^7 m and two energy absorbing layers are placed at the top and right part of the domain.

3.7.4 Sensitivity tests for the choices of η and r_0

Figure 3.7 has nine panels showing the equilibrated temperature and azimuthal wind for a 3×3 combination with η being 1.0%, 1.1%, 1.2% and r_0 being 100 km, 200 km, 300 km. Here η is the deep water vapor mixing ratio and r_0 is the Gaussian radius of the initial disturbance. Larger water mixing ratio results in large temperature difference between the

warm and cold adiabat, thereby larger wind speed and tropospheric warming. Different values of r_0 do not change the overall structure of the wind and the warming because those variables are largely related to the deformation radius of the atmosphere and are insensitive to the initial conditions such as r_0.

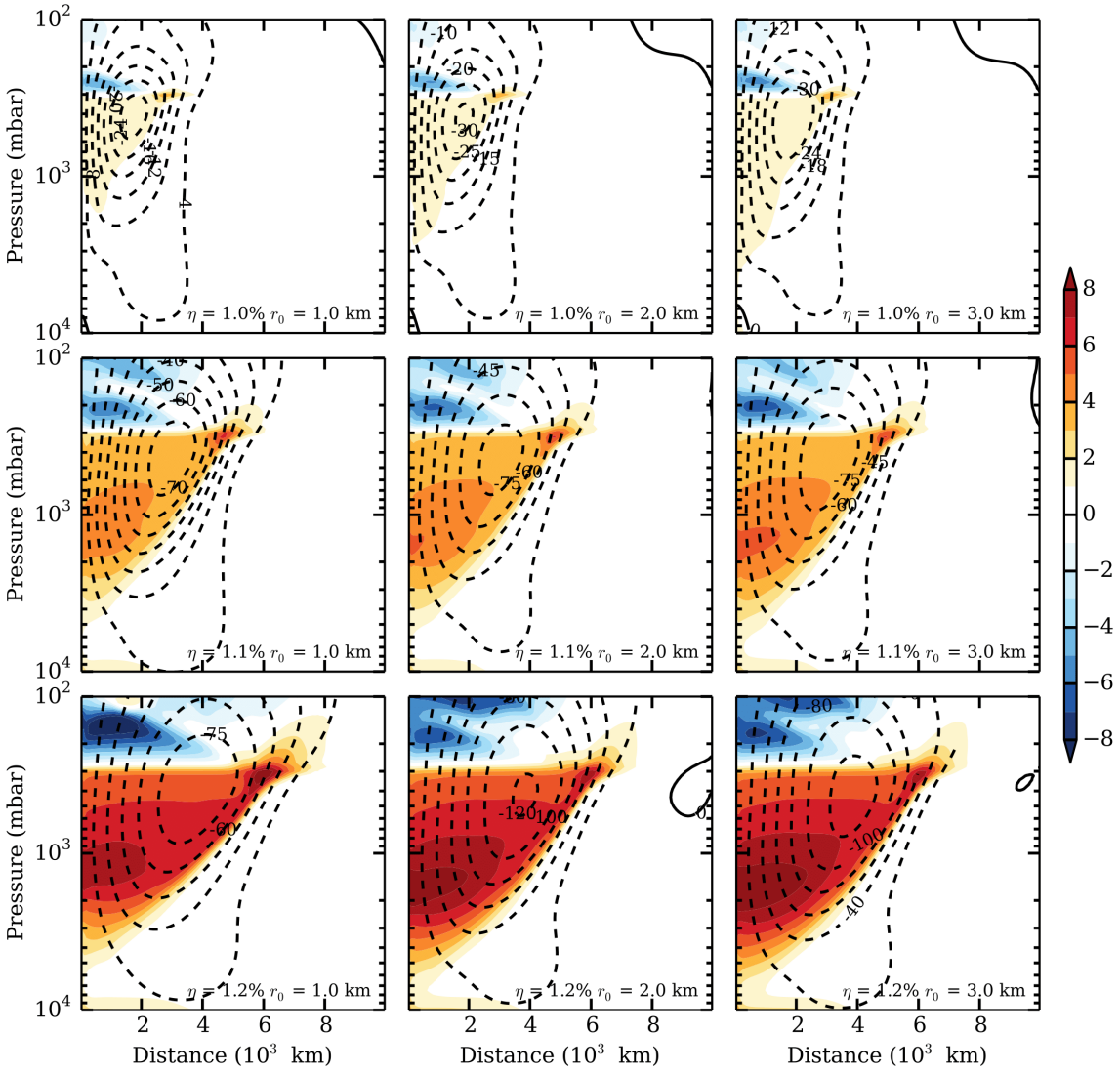

Figure 3.7 Residual azimuthal wind and temperature anomalies for different combinations of parameters. The parameters are indicated at the bottom of each panel. The contours and colors are the same as in Figure 3.3.

3.7.5 More details about the top cooling scheme

The four layer structures described in section 3.5 are fully determined by conservation of column integrated enthalpy and moisture. For example, if we start from the marginally stable state at Year = 2.0 (left boundary of the shaded region, Figure 3.8), any further cooling will result in unstable stratification at the interface. The interface will migrate downward and entrain the air in the topmost grid box of layer 3. Since the entrainment and convective adjustment time scale is small (~ several days) compared to the radiative cooling time scale (~ several years), column integrated enthalpy and moisture should be conserved before and after the entrainment. The convectively adjusted temperature and mixing ratio profiles in layers 1 and 2 are calculated by conservation of column integrated enthalpy and moisture (equations (3.25) and (3.26) in section 3.7.6), which give the right boundary of the shaded region in Year 2.7. The virtual potential temperature above the interface is larger than the virtual potential temperature below it (panel (a), right boundary of the shaded region), meaning that the interface is stable. The next cooling step removes this stable stratification and results in a marginally stable interface (left boundary of the shaded region). The radiated energy in this cooling step is calculated by the enthalpy difference before and after the cooling step and converted into time by a prescribed cooling flux (equation (3.27)). During this cooling step, the top of layer 2 changes its pressure while maintaining conservation of total moisture (equation (3.24)). After the temperature profile reaches the left boundary of the shaded region, the next cycle repeats (from Year = 2.7 to Year = 3.4). These alternating steps continue until Year = 74.0. At that point there is not enough mass left in layer 3 to support another entrainment step, so layer 3 disappears. Then a warm parcel can rise from the deep interior (layer 4) and initiate another giant storm. The

time scale for this final entrainment step is small, so Year = 74.0 can be considered the final stage before the next giant storm.

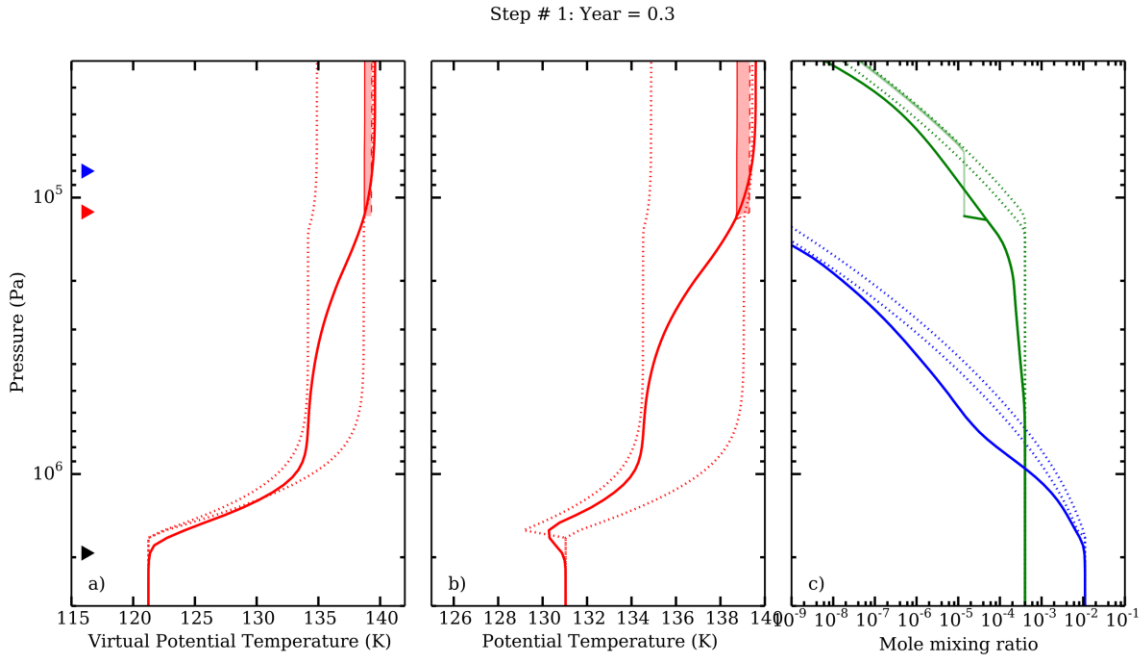

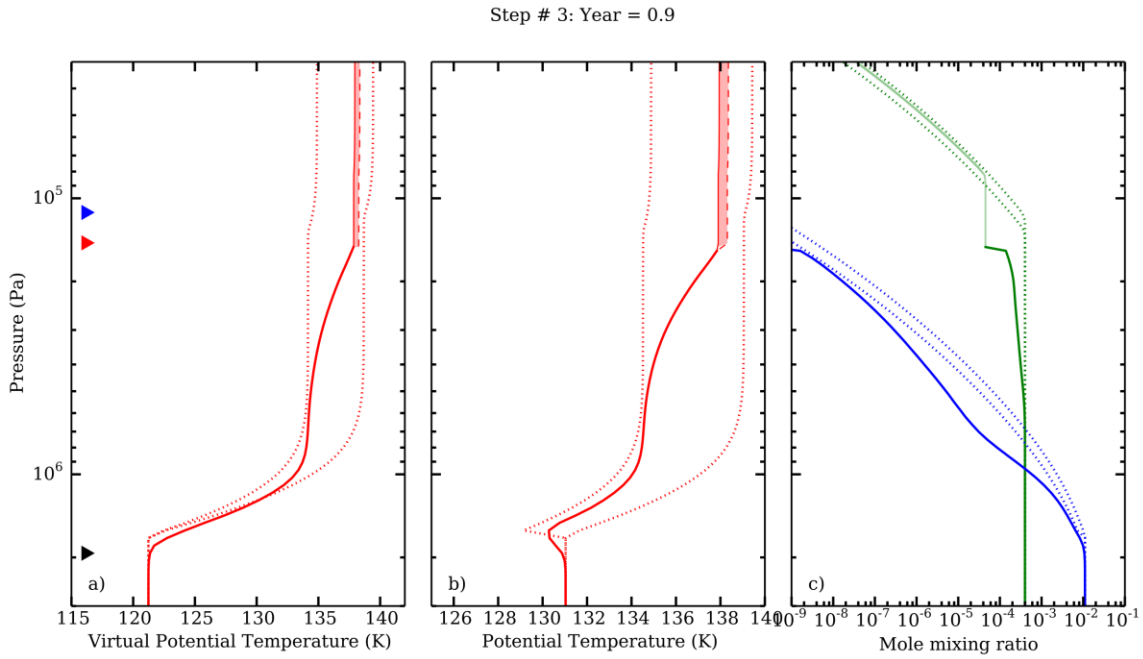

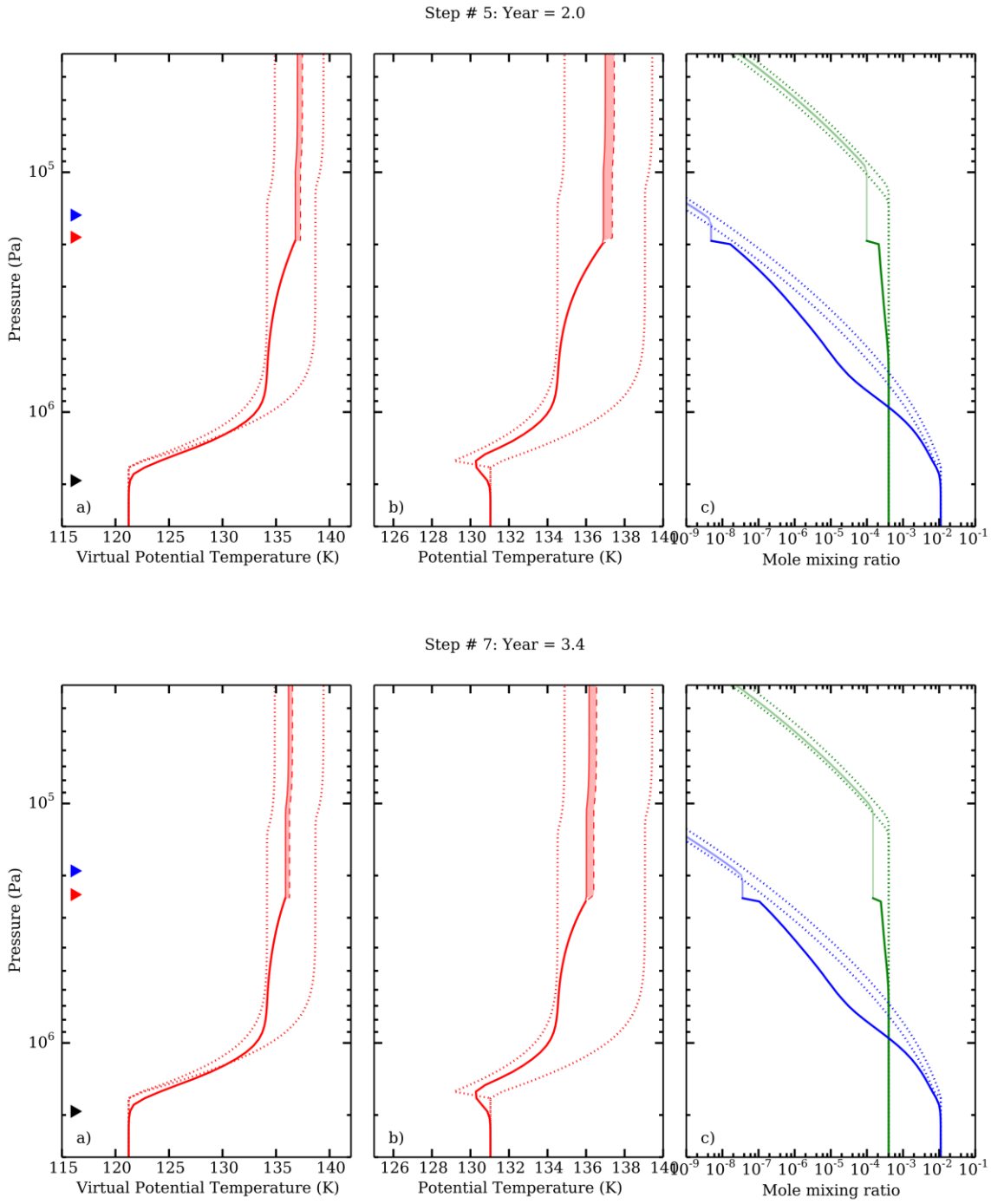

Figure 3.8 A series of cooling steps. Panel (a) and panel (c) represent the same quantities as in Fig. 5. Panel (b) is the potential temperature defined as $\theta = T(p_0/p)^{R/C_p}$. $p_0 = 1$ bar, is the reference pressure. Two dotted lines represent the cold and warm moist adiabat as those in Fig. 2. The thick solid red line is the potential temperature profile after the geostrophic adjustment. The shaded region shows one cooling step, from right to left. The right boundary (dashed line) shows the profile after the preceding entrainment step. The

left boundary (solid line) shows the profile just before the next entrainment step. Only stable interfaces are shown in this figure.

3.7.6 Numerical method of calculating the top cooling scheme

In section 3.5, we presented our scheme for calculating the multi-decadal cooling phase, where the troposphere loses heat from the top. An interface develops between the convecting layers above and the undisturbed layers below. We described the interface moving down through our numerical grid as a two-step process. Step 1 (entrainment step) occurs when the interface is neutrally stable and moves down a level, entraining all the fluid in the grid box below. Step 2 (cooling step) occurs over a period of time and involves lowering the temperature of the fluid above until the interface is neutral again. Here we describe this process in greater detail.

The numerical results calculated by the above scheme at every other grid box are displayed as a time series in Figure 3.8. At each time, the left panel (a) shows virtual potential temperature, whose vertical gradient determines whether the column is stable or unstable to convection. The middle panel (b) shows potential temperature, which gives the contribution of temperature alone to the stability of the column. The right panel (c) gives the mixing ratios of water (blue) and ammonia (green). Temperature itself, which falls off monotonically with altitude at all times, is not shown. The primordial profile, following geostrophic adjustment after the last giant storm, is shown as a heavy solid line in the figure for Year = 0.3. This profile becomes a remnant as the interface moves downward and the primordial layer shrinks. The warm and cold moist adiabats—the solid and dashed red lines

in Figure 3.2 of the main chapter—are shown as dotted lines in Figure 3.8. There are three characteristic features of the potential temperature profile in panel (b). Above the 1 bar level, the profile is close to the warm adiabat. Between 1 bar and 6 bars, the profile follows a transition from the warm adiabat to the cold adiabat. In pressure levels deeper than 6 bars, potential temperature decreases with depth and contributes to the stability of the column, but then it overshoots and creates a potential temperature minimum at the cloud base. However, this negative potential temperature lapse rate is stable because it is compensated by the increase of the mean molecular weight to deep pressure levels. Therefore, the lapse rate of virtual potential temperature in panel (a) is still positive, and the profile is stable.

The lower boundaries of layers 1, 2, and 3 described in the main text are shown as blue, red, and black triangles, respectively. The four layer structure described in the section of radiative cooling phase in the manuscript is best represented at Year = 2.0. Layer 1 is directly subject to radiative cooling at the top. It experiences condensation of ammonia and water. Its temperature profile is moist adiabat and the mixing ratio of the constituent is either the saturated value or a constant. Layer 1 is supported by the dry convecting layer 2 below it. Layer 2 has two roles. First, because it is unsaturated, any precipitation in layer 1 will re-evaporate in layer 2. Layer 2 serves as reservoir that holds the extra moisture in layer 1. Column integrated moisture in layers 1 and 2 is conserved. Second, the lower boundary of layer 2 (the interface) separates the convective layers (layers 1 and 2) from the non-convective layers (layer 3) by a jump in temperature and mixing ratios. In the numerical model, the jump is a discontinuity, but in the figure it appears as a steep gradient. Below Layer 2 is layer 3 where the atmosphere is stably stratified and does not convect to

mix the minor constituents. Since layer 3 is not disturbed by convection, its temperature and mixing ratio profiles are set by the previous geostrophic adjustment. Layer 3 transits into layer 4 at about 20 bars. Layer 4 is the deep interior, which is a dry adiabat with the minor constituents well mixed. It is somewhat arbitrary to define the precise level of the boundary between layer 3 and layer 4 because the temperature and mixing ratios are continuously changing.

As stated in the main chapter, the vertical potential temperature profile (shaded region in Figure 3.8 after year 9 evolves to lower values than the cold adiabat (left dotted line in Figure 3.8a) around year 9, as shown in Figure 3.8. However the interface (red triangle) remains stable relative to the cold adiabat. This is because the troposphere is cooling from the top down, with an initial profile that is unsaturated and stable (thick solid line in step #1 of Figure 3.8). After year 9, the profile is to the left of the cold adiabat in the upper troposphere, but it crosses to the right in the dry adiabatic layer (between the blue and red triangles), making the interface stable.

Here we present the actual numerical implementation of the above scheme. Suppose the atmospheric column is divided into *n* discrete cells centered at pressure, $p_i, i = 0 \ldots n-1$, from top to bottom. The profile of temperature and mixing ratios are $T_i,\ \eta_i^a,\ \eta_i^w$ where *w* represents "water" and a represents "ammonia". These variables are cell averaged quantities from $p_{i-1/2}$ to $p_{i+1/2}$ over the width of the remaining anticyclone after the geostrophic adjustment (section 3.4). The boundary values between cells are calculated by

linear interpolation. We define ϵ^w and ϵ^a as the molecular weights of water and ammonia relative to that of the H_2-He mixture. Then the corresponding mass mixing ratios are:

$$r^a = \frac{\eta^a \epsilon^a}{1 + \eta^a \epsilon^a + \eta^w \epsilon^w}, \qquad r^w = \frac{\eta^w \epsilon^w}{1 + \eta^a \epsilon^a + \eta^w \epsilon^w}, \tag{3.19}$$

Mass per unit area of each cell is:

$$m_i = \frac{p_{i+1/2} - p_{i-1/2}}{g}. \tag{3.20}$$

Column integrated moisture per unit area above the cell k is:

$$Q_k^a = \sum_{i=0}^{k} r_i^a m_i \ , \qquad Q_k^w = \sum_{i=0}^{k} r_i^w m_i \ . \tag{3.21}$$

Column integrated enthalpy per unit area above the cell k is:

$$H_k = \sum_{i=0}^{k} C_p T_i m_i \ . \tag{3.22}$$

If the bottom of layer 2 is located at the bottom of cell k: $p = p_{k+1/2}$, then all quantities above that level are determined by $T_k,\ \eta_k^a,\ \eta_k^w$, at pressure p_k. This is because layer 2 is dry adiabatic with constant mixing ratios and layer 1 is moist adiabatic with saturation mixing ratios. One simply follows the dry adiabat up to cloud base—the lifting condensation level for each gas—and then follows the moist adiabat from that point on. This gives $T_i,\ \eta_i^a,\ \eta_i^w, i = 0 \ldots k$, so one can calculate $H_k,\ Q_k^a, Q_k^w$.

Let the initial profile of temperature and mixing ratios to be $T_i^0,\ \eta_i^{a,0},\ \eta_i^{w,0}, i = 0 \ldots n-1$. We proceed from one entrainment step to the next, during which time the interface moves down from pressure $p_{k-1/2}$ to pressure $p_{k+1/2}$. We assume the preceding entrainment step ended with a stable interface at pressure $p_{k+1/2}$, as indicated by the dashed line in Fig. S3. In other words, the virtual temperature above the interface was greater than that below the interface:

$$T_{k+1/2}\frac{1+\eta_{k+1/2}^a+\eta_{k+1/2}^w}{1+\epsilon^a\eta_{k+1/2}^a+\epsilon^w\eta_{k+1/2}^w} \geq T_{k+1/2}^0\frac{1+\eta_{k+1/2}^{a,0}+\eta_{k+1/2}^{w,0}}{1+\epsilon^a\eta_{k+1/2}^{a,0}+\epsilon^w\eta_{k+1/2}^{w,0}}. \tag{3.23}$$

The cycle begins with the slow cooling step, which reduces H_k and T_i, with $\eta_i^a,\ \eta_i^w, i = 0 \ldots k$ adjusted to maintain the dry/moist adiabat and conserve the total moisture per unit area:

$$Q_k^a = Q_k^{a,0}, \qquad Q_k^w = Q_k^{w,0}\ . \tag{3.24}$$

where $Q_k^{a,0},\ Q_k^{w,0}$ are the initial column-integrated moisture per unit area. When equation (3.23) becomes an equality, as indicated by the thin solid line in Figure 3.8, the cooling step ends and the next entrainment step begins. The proper temperature and moistures at cell k: $T_k,\ \eta_k^a,\ \eta_k^w$, when the cooling step ends, are solved using Newton's iteration method to satisfy equations (3.23) and (3.24). After we solved for these quantities, we can go for the vertical profiles of $T_i,\ \eta_i^a,\ \eta_i^w, i = 0 \ldots k$ by following a dry adiabat and then moist adiabat. The column-integrated enthalpy per unit area is bookkept as H_k^+ using equation (3.22).

The entrainment process moves the interface down to pressure $p_{k+3/2}$. The new column-integrated enthalpy and column-integrated moisture per unit area are

$$H_{k+1} = H_k^+ + C_p T_{k+1}^0 m_{k+1} \,, \tag{3.25}$$

$$Q_{k+1}^a = Q_k^{a,0} + r_{k+1}^{a,0} m_{k+1}, \qquad Q_{k+1}^w = Q_k^{w,0} + r_{k+1}^{w,0} m_{k+1} \,, \tag{3.26}$$

where $r_{k+1}^{a,0},\ r_{k+1}^{w,0}$ are the initial mass ratios. One then solves, iteratively, for the new values of $T_{k+1},\ \eta_{k+1}^a,\ \eta_{k+1}^w$ that give the values on the left sides of equations (3.25) and (3.26). The interface is now at pressure $p_{k+3/2}$. The elapsed time $\Delta\tau_k$ during this cycle is computed from the decrease in H_k needed to drive the inequality in equation (3.23) to equality, i.e.:

$$\Delta\tau_k = \frac{\Delta H_k}{Flux} = \frac{H_k - H_k^+}{Flux}, \qquad Flux = 4.5\ \mathrm{W/m^2} \,. \tag{3.27}$$

If the virtual temperature above this new interface is smaller than the virtual temperature below it, the interface is unstable. Then the interface moves one cell further down and the entrainment step repeats until a stable interface is found or the interface reaches the deep interior.

3.7.7 Discussion about the six occurrences of giant storms in the northern hemisphere

We feel that the occurrence in the northern summer could be a statistical fluke complicated by the difficulty of using discrete statistics on hard-to-define phenomena in a turbulent fluid. (Sanchez-Lavega, 1994) defines a Great White Spot as "a kind of rarely-observed disturbance that rapidly grows and expands zonally from a single outburst site, and whose

visual appearance is that of a complex pattern of bright white clouds confined to a large latitude band that breaks with the usual banded telescopic aspect of the planet." From 2004 to 2010, Cassini observed lightning storms near the center of the westward jet at 35^{o} in the southern hemisphere, but not at any other latitude. The season was southern summer in 2004 and early autumn in 2010, so not all activity is in the northern hemisphere. The 1876 storm had the shortest lifetime of 26 days, and until the 2010-2011 storm, the 1903 storm had the longest lifetime of 150 days. The lifetime of the 2010-2011 storm was ~200 days. The fact that we are dealing with real phenomena in a turbulent fluid adds uncertainty to statistical inferences. Even if we were dealing with six coin flips, the probability of their all coming out the same is 1/32. Since one of the great storms was at a latitude of 2 ± 3°N, the number of coins should probably be reduced to five, for which the probability of their all falling in one hemisphere is 1/16. What seems more likely to us is a preference for the sunlit hemisphere, with a statistical fluke favoring the north. A preference for the sunlit hemisphere and for the extrema of the zonal jets might have a physical basis, but we leave that for another paper.

3.7.8 Discussion about radiative heat transfer near the cloud base

Guillot et al. (1994) points out that the giant planets might not be fully convective—that at some levels the radiative opacity is small enough that the internal heat flux could be carried by radiation. For Saturn, they show that a radiative zone could develop in the layer from 300 K < T < 450 K, which spans cloud base according to our Figure 3.2. Then the cooling shown in Figure 3.5 and Figure 3.8 might not occur, and the atmosphere above cloud base might reach a steady state, with 4.5 W m^{-2} coming in at the bottom and 4.5 W m^{-2} going

out at the top. The interface at cloud base, stabilized by the molecular weight gradient, would never cool enough to initiate a giant storm. In this situation, one should remember that atmospheric temperature profile has CAPE, which means it has the potential to convect when the stable interface is broken by an other mechanism such as the re-evaporation of condensates from above (Sugiyama et al., 2014).

However, the existence of a radiative zone is uncertain. It vanishes if water clouds are present around this level, as shown in Figure 6 of Guillot. If it vanishes, then giant storms can occur. If radiation delivers more than zero but less than the 4.5 W m^{-2} needed to maintain steady state, then the layers above will still cool but at a slower rate. This lengthens the interval between giant storms, but it does not prevent them. Despite the uncertainty, we shall assume that the time between giant storms is set by the time it takes the atmosphere to cool from the warm adiabat to the cold one, as illustrated in Figure 3.2.

Chapter 4 Inversion of Jovian water, ammonia and dynamics using Juno Microwave Radiometer

Cheng Li[1], Andrew P. Ingersoll[1] and Michael Janssen[2]

[1]Division of Geological and Planetary Science, California Institute of Technology, Pasadena, CA, 91125

[2]Jet Propulsion Laboratory, California Institute of Technology

Preprint, in preparation for submission

4.1 Abstract

The Juno Microwave Radiometer (MWR) is designed to measure the thermal emission from Jupiter's atmosphere from the cloud tops at about 1 bar pressure to as deep as hundreds of bars pressure, with unprecedented accuracy (0.1% in the relative limb darkening measurement) and spatial resolution (100 km footprints near the equator). Unlike infrared spectroscopy, microwave observations of giant planetary atmospheres are difficult to interpret due to the breadth of the weighting functions and the absence of spectral features. The observed radiance is an intricate consequence of thermodynamic and dynamic processes. To sort out these processes, we first review the thermodynamic model for the atmosphere laden with multiple condensable species and with variable heat capacity. We generalize the expression of moist adiabatic lapse rate and clarify the assumptions used in various formulas in the literature. Second, we develop two scalar variables that parameterize dynamic alteration of the atmosphere from an equilibrium condensation model. Finally, we make use of the state-of-the-art retrieval method – Markov Chain Monte Carlo – to determine the joint probability distribution of all parameters of interest. This approach fully calibrates error, assesses covariance between parameters, and explores the widest possible types of atmospheric conditions in contrast to traditional trial-and-error method. We apply this method to simulated Juno/MWR observations. We show that the water abundance is constrained to +3.1/-1.5 times solar for a normal situation (close to a moist adiabat) and is constrained to an upper limit for an extreme situation (close to a dry adiabat).

4.2 Introduction

Water is the key to a giant planet's volatile and heavy element history because H, He, and O are the three most abundant elements, and a significant fraction of a giant planet's total mass resides in its gaseous envelopes (Helled and Lunine, 2014). Water is also the key to a giant planet's meteorology, which we observe at the cloud level because it provides an additional heat source to drive jets, vortices and thunderstorms when it condenses at low pressure (Li et al., 2006; Showman, 2007).

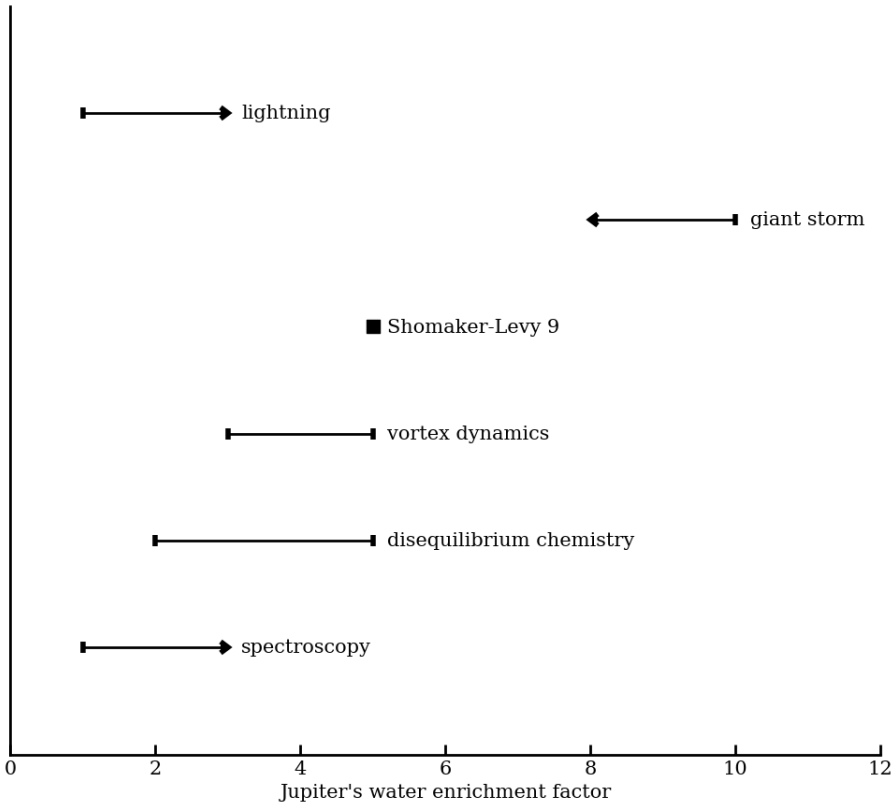

Figure 4.1 A compilation of Jupiter's water abundance inferred by various methods. The methods are indicated in the figure and the references are explained in the main text. Water abundance is measured in enrichment factor with respect to solar (Asplund et al., 2009).

Many attempts have been made to determine Jupiter's water abundance using spectroscopy, disequilibrium chemical species, dynamics and lightning. Their methods and preferred values for the water abundances are summarized in Figure 4.1. To be specific, 1) The overall O/H ratio derived by spectroscopy near 5 μm (Bjoraker et al., 2015; Giles et al., 2015; Roos-Serote et al., 2004) and visible images (Banfield et al., 1998) is compatible with one or more times solar (Asplund et al., 2009), though the results are inconclusive and display large spatial variance. 2) Studies of disequilibrium chemical species (CO, PH_3, etc.), which trace back to Prinn and Barshay (1977) and were further developed by Visscher et al. (2010) and Wang et al. (2015) prefer a 2 – 5 times solar abundance of water. 3) The size of vortices and the spacing of jets are partially governed by the radius of deformation $L_d \sim (R\Delta\theta/f^2)^{1/2}$ for the observed weather layer (Barcilon and Gierasch, 1970; Ingersoll and Cuong, 1981); where $R \approx 3.7 \times 10^3$ J/ kg^{-1} K^{-1} is the gas constant for Jupiter's atmosphere; $f = 1.75 \times 10^{-4}$ s^{-1} is the planetary vorticity and $\Delta\theta$ is the potential temperature difference between the weather layer and the deep atmosphere. Numerical simulation of Jupiter's Great Red Spot favors L_d to be $1000 - 2000$ km (Dowling and Ingersoll, 1989), which translates into $\Delta\theta \approx 8 - 33$ K. The range is consistent with a three to five times solar abundance of water. 4) The collision of comet Shoemaker-Levy 9 with Jupiter created ripples propagating at the speed of 450 m/s (Hammel et al., 1995). The observed ripples can either propagate in the stratosphere (Walterscheid et al., 2000) or are caused by trapped gravity waves in a stable layer produced by moist convection in the troposphere (Ingersoll et al., 1994). If they do originate in the troposphere, the water abundance is estimated to be five times solar (Ingersoll and Kanamori, 1995). Note that the solar abundance of O/H has been updated and the value used in Ingersoll and Kanamori

(1995) is about a half of what we use in this chapter (Asplund et al., 2009). 5) The absence of giant cyclic storms like those on Saturn suggests an upper limit of 10 times solar abundance for water (Li and Ingersoll, 2015). 6) Spatially resolved brightness distribution of lightning in Voyager and Galileo images infers that the depth of lightning is beyond 5 bars (Dyudina et al., 2007), consistent with a water abundance enriched over its solar value.

In contrast to all indirect inferences, the only in situ measurement of the water abundance comes from the Galileo Probe, which detected 2 – 5 times enrichment of CH_4, NH_3, and H_2S with respect to the solar, but the amount of water was severely subsolar (Niemann et al., 1996; Wong et al., 2004). The most plausible explanation that reconciles the Galileo probe result and other evidence is that the Galileo probe entered the "Sahara Desert" of Jupiter, which is identified by a 5-μm hot spot. Dynamic dry downdrafts dominate this region and deplete water from a globally average value (Showman and Ingersoll, 1998). The assumption has been further tested using a three dimensional numerical model (Showman and Dowling, 2000) with prescribed wave forcing showing that atmospheric dynamics could create a trough in the material surface, such that air flowing through the hot spots undergoes a temporary increase in pressure by a factor of 2. Though this deflection of material surface toward a high pressure is still too small to explain the Galileo probe results, it shows that the thermodynamics and dynamics of Jupiter's atmosphere have a complicated interaction and should not be considered separately.

The Juno spacecraft, which will arrive and orbit Jupiter in late 2016, will open a new frontier in the field. The Juno Microwave Radiometer (MWR) will measure the limb

darkening of Jupiter's atmosphere at six wavelengths and multiple limb angles. Limb darkening – defined as the relative change of brightness temperature at a limb angle with respect to the nadir one – is a relative measurement, so it is an order of magnitude more accurate (~0.1%) than the absolute brightness temperature measurements. Unfortunately, the major absorber in the Juno/MWR wavelengths is ammonia, and water has its effect in the limb darkening spectra through the change of lapse rate when it condensed. Four scenarios for water are studied in Figure 4.2. The one, in which water does not release latent heat but has opacity, has a smaller signal than the opposite one, in which water releases latent heat but does not have opacity. If the atmospheric vertical structure were moist adiabat, the Juno/MWR would be able to retrieve the deep water abundance (Janssen et al., 2005). The strategy of the Juno/MWR team begins with this idealized setup.

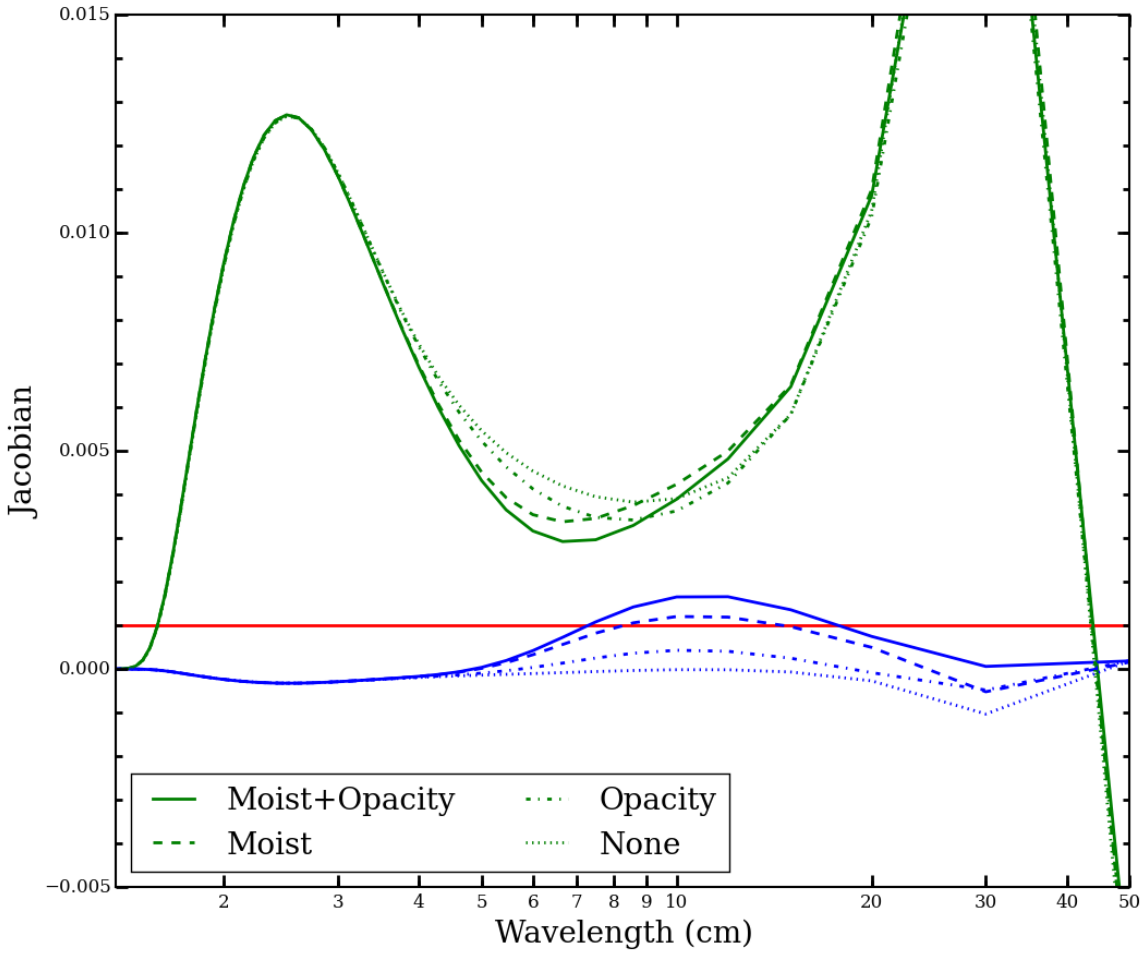

Figure 4.2 Water's signal in the Juno/MWR spectra. The vertical axis (Jacobian) is the fractional change of limb darkening when the deep abundances of water (blue line) and ammonia (green line) are changed by 1 times solar. Four scenarios are studied: water does not have latent heat or opacity (dotted line); water has opacity but no latent heat (dash-dotted line); water has latent heat but no opacity (dashed line); water has both latent heat and opacity (solid line). Red line is the error limit of limb darkening measurements (0.1%).

However, the atmosphere of Jupiter can be very far from an idealized moist adiabat, as evidence from the recent 5 μm observation of Jupiter's atmosphere (Bjoraker et al., 2015). In fact, studies with the Very Large Array (VLA) show depleted ammonia with respect to saturation for all four giant planets in the Solar System (de Pater et al., 2001; de Pater and Massie, 1985). The same depletion of ammonia is also observed after Saturn's Giant Storm (Janssen et al., 2013; Laraia et al., 2013) and in the smaller storm in Saturn's southern hemisphere (Dyudina et al., 2007). Li and Ingersoll (2015) modeled the dynamic desiccation of ammonia after convection using numerical simulation, and they found that geostrophic adjustment processes after convection deplete ammonia from saturation. Sugiyama et al. (2014) used a two-dimensional cloud-resolving model to show the explicit cycles of convective events. In their model, ammonia and water remain unsaturated during the quiescent period of the cycle. Since thermodynamics and dynamics are inevitably intertwined, and neither of them are understood well enough to give a conclusive picture of the atmosphere, a novel thermodynamic model and dynamic parameterization are developed to balance the flexibility to model a variety of dynamic processes and the accuracy to retrieve the water abundance from the limb darkening spectra.

Section 4.3 describes the new thermodynamic model applied to the atmosphere laden with multiple condensable species and with variable heat capacity. The assumptions used in deriving the moist adiabatic lapse rate are clarified. Section 4.4 describes two dynamic parameterizations that are used in the retrievals. Section 4.5 describes the retrieval method and results on synthetic Juno/MWR observations. Sections 4.6 concludes and discusses the potential application of this method to ground based observations.

4.3 Thermodynamic model

The ground work of Jupiter's thermodynamic model was laid by Weidenschilling and Lewis (1973) and Atreya (1987). Their expression for the moist adiabatic lapse rate is used in numerous papers from then on. Because Juno/MWR measures limb darkening in the precision of parts per thousand, the traditional Jovian thermodynamics – assuming constant heat capacity and small mixing ratios of condensates – needs to be updated according to the requirement of the new instrument. Here we develop a new thermodynamic model that accounts for the temperature dependence of heat capacity and latent heat in a physically consistent way. This model generalizes the thermodynamics in the presence of multiple condensable species and chemical reactions. It can handle any ratio of condensable vapor to dry gas – from zero to infinity – and can be coupled to dynamic parameterization as described in section 4.3.

4.3.1 Generalized moist adiabatic model

The derivation of generalized moist adiabat model largely follows chapter 4 in Emanuel (1994) but extends to ideal gas with varying heat capacity as a function of temperature and multiple condensable species. It calculates the temperature and moisture of an air parcel when it is displaced reversibly and adiabatically. We assume that an air parcel is an ideal mixture of dry air, vapors and clouds (condensed liquid and solid), and each gaseous component satisfies ideal gas law $PV = nRT$. Using the first law of thermodynamics for one mole of pure ideal gas:

$$\begin{aligned} T\mathrm{d}S &= \mathrm{d}H - V\mathrm{d}P \\ &= \mathrm{d}H - RT\mathrm{d}\ln P \\ &= c_p(T)\mathrm{d}T - RT\mathrm{d}\ln P\,. \end{aligned} \tag{4.1}$$

The entropy at temperature T and pressure P is obtained from integrating equation (4.1):

$$S(T,P) = \int c_p(T)\frac{dT}{T} - R\mathrm{d}\ln P = s(T) - RT\ln P\,. \tag{4.2}$$

We have neglected the integration constant, and $s(T)$ denotes the result of integral $\int c_p(T)\frac{dT}{T}$. For a gas with constant heat capacity c_p, $s(T) = c_p \ln T$. We will use subscript *d* for the dry component of a gas mixture, subscript *v* for vapor, subscript *c* for cloud and subscript *i* for *i*-th condensable component later on.

The entropy of a condensed component is related to the gaseous component through the definition of latent heat:

$$\begin{aligned} L(T) &= T \times [S_v(T,P) - S_c(T,P)]\,, \\ S_c(T,P) &= S_v(T,P) - \frac{L(T)}{T}\,, \end{aligned} \tag{4.3}$$

where $S_v(T,P)$ is the molar entropy of saturated vapor. Note that by writing the latent heat as $L(T)$, we neglect the pressure dependence of L, but we account for its temperature dependence. The first derivative of latent heat is given by Kirchhoff's law:

$$\frac{\mathrm{d}\,L(T)}{\mathrm{d}\,T} = c_p(T) - c_c(T)\,, \tag{4.4}$$

where $c_c(T)$ is the heat capacity of a condensed phase.

Consider one mole of gas-cloud mixture, in which the molar amount of dry air is x_d, the molar amounts of i-th vapor and cloud are x_{v_i} and x_{c_i} respectively. The total molar amount of condensable componet i is conserved during phase change, which is denoted as $x_{t_i} = x_{v_i} + x_{c_i}$ and $x_d + \sum_i x_{t_i} = 1$. The total entropy is the sum of the entropy of each component

$$\begin{aligned} S(T,P) &= x_d S_d(T,P) + \sum\nolimits_i x_{v_i} S_{v_i}(T,P) + \sum\nolimits_i x_{c_i} S_{c_i}(T,P) \\ &= x_d s_d(T) + \sum\nolimits_i x_{t_i} s_{v_i}(T) - R\left(x_d \ln P_d + \sum\nolimits_i x_{t_i} \ln P_{v_i}\right) \\ &\quad - \sum\nolimits_i x_{c_i} \frac{L_i(T)}{T} \\ &= \bar{s}(T) - R\left(x_d \ln P_d + \sum\nolimits_i x_{t_i} \ln P_{v_i}\right) - \sum\nolimits_i x_{c_i} \frac{L_i(T)}{T}, \end{aligned} \tag{4.5}$$

where P_d and P_{v_i} are the partial pressures defined by

$$P_d = \frac{x_d}{x_d + \sum_i x_{v_i}} P, P_{v_i} = \frac{x_{v_i}}{x_d + \sum_i x_{v_i}} P\,, \tag{4.6}$$

and $\bar{s}(T)$ is defined as

$$\begin{aligned} \bar{s}(T) &= \int \left(x_d c_{pd}(T) + \sum\nolimits_i x_{t_i}\, c_{pv_i}(T)\right) \frac{dT}{T} \\ &= x_d s_d(T) + \sum\nolimits_i x_{t_i}\, s_{v_i}(T)\,. \end{aligned} \tag{4.7}$$

Conventionally, entropy is expressed as potential temperature (θ), which is defined implicitly as:

$$S(\theta, P^0) = \bar{s}(\theta) - R\left(x_d \ln P_d^0 + \sum_i x_{t_i} \ln P_{v_i}^0\right). \tag{4.8}$$

P^0 is the reference pressure at which all condensates evaporate. Let $S(T, P) = S(\theta, P^0)$ gives an implicit expression for potential temperature:

$$\bar{s}(\theta) = \bar{s}(T) + R \ln\left(\frac{P_d^0}{P_d}\right) - R \sum_i x_{t_i} \ln \frac{x_{v_i}}{x_{t_i}} - \sum_i \frac{L_i(T)}{T} x_{c_i}\,. \tag{4.9}$$

The potential temperature defined in equation (4.9) is known as "liquid water potential temperature" in Emanuel (1994) (equation 4.5.15), but generalized for gases with non-constant heat capacities. It represents the temperature of an air parcel when it is adiabatically compressed to a reference pressure P^0 such that all its condensates evaporate. We also define the dry potential temperature θ_d by dropping the latent heat term in equation (4.9):

$$\bar{s}(\theta_d) = \bar{s}(T) + R \ln\left(\frac{P_d^0}{P_d}\right) - R \sum_i x_{t_i} \ln \frac{x_{v_i}}{x_{t_i}}\,, \tag{4.10}$$

to describe the potential temperature of an air parcel with no condensate when it is adiabatically compressed to a reference pressure P^0. Note that equation (4.9) and (4.10) reduce to the nominally defined potential temperature if no vapor has condensed and if the heat capacity is constant, as can be seen by setting $x_{c_i} = 0$, $x_{v_i} = x_{t_i}$, $\bar{s}(T) = c_p \ln T$ and $\bar{s}(\theta) = c_p \ln \theta$

$$\theta = \theta_d = T\left(\frac{P_d^0}{P_d}\right)^{R/c_p} = T\left(\frac{P^0}{P}\right)^{R/c_p} . \tag{4.11}$$

In the next paragraphs, we will derive the moist adiabatic lapse rate $\Gamma_m = \frac{\ln T}{\ln P}$ by taking the derivative of equation (4.9) with respect to $\ln P$. Another way to derive Γ_m using the differential form of the thermodynamic laws are also provided in the appendix section 4.7.1. The results are the same.

After taking the derivative of equation (4.9) with respect to $\mathrm{d}\ln P$, The left hand side is zero and the right hand side has four terms. The first term is

$$\frac{\mathrm{d}\bar{s}(T)}{\mathrm{d}\ln P} = T\frac{\mathrm{d}\bar{s}(T)}{\mathrm{d}T}\frac{\mathrm{d}\ln T}{\mathrm{d}\ln P} = \left(x_d c_{pd}(T) + \sum\nolimits_i x_{t_i}\, c_{v_i}(T)\right)\Gamma_m . \tag{4.12}$$

The second term is

$$R\frac{\mathrm{d}(\ln P_d^0 - \ln P_d)}{\mathrm{d}\ln P} = -R\frac{\mathrm{d}\ln P_d}{\mathrm{d}\ln P} . \tag{4.13}$$

The third term is

$$-R\sum\nolimits_i x_{t_i}\frac{\mathrm{d}\left(\ln x_{v_i} - \ln x_{t_i}\right)}{\mathrm{d}\ln P} = -R\sum\nolimits_i x_{t_i}\frac{\mathrm{d}\ln x_{v_i}}{\mathrm{d}\ln P} . \tag{4.14}$$

The fourth term is

$$
\begin{aligned}
&-\sum_i \frac{\mathrm{d}}{\mathrm{d}\ln P}\left(\frac{L_i(T)}{T}x_{c\,i}\right) \\
&= -\sum_i \left(\frac{x_{c_i}}{T}\frac{\mathrm{d}L_i(T)}{\mathrm{d}\ln P} + \frac{L_i(T)}{T}\frac{\mathrm{d}x_{c_i}}{\mathrm{d}\ln P} - \frac{x_{c_i}L(T)}{T}\Gamma_m\right) \\
&= \sum_i \frac{x_{v_i}L_i(T)}{T}\frac{\mathrm{d}\ln x_{v_i}}{\mathrm{d}\ln P} + \sum_i x_{c_i}\left(\frac{L_i(T)}{T} - \left(c_{pv_i}(T) - c_{c_i}(T)\right)\right)\Gamma_m\,.
\end{aligned}
\tag{4.15}
$$

Note that we have used equation (4.4) and $x_{t_i} = x_{v_i} + x_{c_i}$ to derive equation (4.15). These four terms are all expressed in three gradients: Γ_m, $\mathrm{d}\ln P_d\,/\mathrm{d}\ln P$ and $\mathrm{d}\ln x_{v_i}\,/\mathrm{d}\ln P$. The first one is what we want and the last two are unknown. Equation (4.6) is used to derive the expression for the last two gradients. First take the logarithm of the second equation of (4.6) and then take differentials:

$$
\begin{aligned}
\mathrm{d}\ln\frac{P_{v_i}}{P} &= \mathrm{d}\ln x_{v_i} - \mathrm{d}\ln\left(x_d + \sum_i x_{v_i}\right) \\
&= \mathrm{d}\ln x_{v_i} - \frac{\sum_i \mathrm{d}x_{v_i}}{x_d + \sum_i x_{v_i}}\,.
\end{aligned}
\tag{4.16}
$$

For a system with a single condensable component, equation (4.16) is trivial to solve for $\mathrm{d}\ln x_{v_i}$ in terms of $\mathrm{d}\ln P_{v_i}$. But for a system with multiple condensable components, a set of equations needs to be solved simultaneously. The way to solve this set of equations is to solve for the case of two species first and then generalize the solution for multiple species. We provide the detailed procedures in the appendix section 4.7.2 and list the solution below:

$$\frac{\mathrm{d}\ln x_i}{\mathrm{d}\ln P} = \frac{\mathrm{d}\ln P_{v_i}}{\mathrm{d}\ln P} - 1 + \sum\nolimits_j \eta_j \left(\frac{\mathrm{d}\ln P_{v_j}}{\mathrm{d}\ln P} - 1 \right), \tag{4.17}$$

where $\eta_i = x_{v_i}/x_d$ is the molar mixing ratio with respect to dry air. Second, the vapor pressure is proportional to the molar mixing ratio:

$$\begin{aligned} \frac{\mathrm{d}\ln P_d}{\mathrm{d}\ln P} &= \frac{\mathrm{d}\ln P_{v_i}}{\mathrm{d}\ln P} - \frac{\mathrm{d}\ln x_{v_i}}{\mathrm{d}\ln P} \\ &= 1 - \sum\nolimits_j \eta_j \left(\frac{\mathrm{d}\ln P_{v_j}}{\mathrm{d}\ln P} - 1 \right) . \end{aligned} \tag{4.18}$$

x_d vanishes in equation (4.18) because it is a constant. Equation (4.17) and (4.18) can be further simplified using the Clausius-Clapeyron relation:

$$\frac{\mathrm{d}\ln P_{v_i}(T)}{\mathrm{d}\ln T} = \frac{L_i(T)}{RT} = \beta_i(T) . \tag{4.19}$$

Because all derivative are expanded, we omit (T) in $\beta(T)$ and $c_p(T)$ for clarity.

$$\begin{aligned} \frac{\mathrm{d}\ln P_d}{\mathrm{d}\ln P} &= 1 - \sum\nolimits_j \eta_j \left(\beta_j \Gamma_m - 1\right) , \\ \frac{\mathrm{d}\ln x_i}{\mathrm{d}\ln P} &= \beta_i \Gamma_m - 1 + \sum\nolimits_j \eta_j \left(\beta_j \Gamma_m - 1\right) . \end{aligned} \tag{4.20}$$

Substitute equation (4.20) into equations (4.12) – (4.15) gives

$$\frac{\mathrm{d}\bar{s}(T)}{\mathrm{d}\ln P} = \left(x_d c_{pd} + \sum\nolimits_i x_{t_i} c_{pv_i}\right)\Gamma_m \,,$$

$$R\,\frac{\mathrm{d}(\ln P_d^0 - \ln P_d)}{\mathrm{d}\ln P} = -R\left(1 + \sum\nolimits_j \eta_j - \sum\nolimits_j \eta_j \beta_j \Gamma_m\right),$$

$$-R\sum\nolimits_i x_{t\,i}\,\frac{\mathrm{d}\left(\ln\left(\frac{x_{v_i}}{x_{t_i}}\right)\right)}{\mathrm{d}\ln P}$$

$$= -R\sum\nolimits_i x_{t\,i}\left(\beta_i\Gamma_m - 1 - \sum\nolimits_j \eta_j + \sum\nolimits_j \eta_j\beta_j\Gamma_m\right),$$

$$-\sum\nolimits_i \frac{\mathrm{d}}{\mathrm{d}\ln P}\left(\frac{L_i(T)}{T}x_{c\,i}\right) =$$

$$R\sum\nolimits_i \beta_i x_{v_i}\left(\beta_i\Gamma_m - 1 - \sum\nolimits_j \eta_j + \sum\nolimits_j \eta_j\beta_j\Gamma_m\right)$$

$$+\sum\nolimits_i x_{c_i}\left(R\beta_i - \left(c_{pv_i} - c_{c_i}\right)\right)\Gamma_m \,. \tag{4.21}$$

The four equations sum to zeros. Collecting all terms involving Γ_m to the left hand side and all other terms to the right hand side results

$$\Gamma_m = \frac{1 + \sum_i \eta_i\beta_i}{\widehat{c_p}/R + \frac{\sum_i \eta_i {\beta_i}^2 + (\sum_i \eta_i\beta_i)^2}{1 + \sum_i \eta_i}}\,,$$

$$\widehat{c_p} = \frac{\bar{c_p}}{x_d + \sum_i x_{v_i}} = \frac{x_d c_{pd} + \sum_i x_{v_i} c_{pv_i} + \sum_i x_{c_i} c_{pc_i}}{x_d + \sum_i x_{v_i}}\,. \tag{4.22}$$

The above expression for reversible moist adiabatic lapse rate is exact under the following approximations:

1) The air parcel can be considered as an ideal mixture and follows ideal gas law.

2) The specific volume of condensates is neglected.

3) The pressure dependence of latent heat is neglected.

If the implicit expression of potential temperature in equation (4.9) is used instead of equation (4.22), the second approximation can be relaxed because the Clausius-Clapeyron relation is not used in deriving equation (4.9). By assuming a single condensable component and constant heat capacity, equation (4.22) reduces to the moist adiabatic lapse rate derived by Emanuel (1994) (equation 4.7.5) after rearrangement of terms. By further assuming small concentration of condensable species, equation (4.22) reduces to that derived by Weidenschilling and Lewis (1973). Furthermore, equation (4.22) reduces to the Clausius-Clapeyron relation for a single component steam atmosphere ($\eta \to \infty$):

$$\frac{\mathrm{d}\ln T}{\mathrm{d}\ln P} = \lim_{\eta\to\infty} \frac{R}{\hat{C}_p} \frac{\frac{\eta L(T)}{RT}}{\frac{\eta L^2(T)}{\hat{C}_p RT^2}} = \frac{RT}{L}. \tag{4.23}$$

4.3.2 NH_3 solution

The amount of gas dissolved in a solution is described by two limit laws: Henry's law and Raoult's law. Henry's law states that for a sufficiently dilute solution, the partial pressure of the solute (P) is proportional to the molar concentration of the solute (c). The proportionality constant is Henry's law constant (k_H). In mathematical form:

$$\text{Henry's law:} \qquad \lim_{c\to 0} P(c,T) \to c k_H(T) \tag{4.24}$$

On the other hand, Raoult's law states that, under the condition of ideal solution, the partial pressure of each component in the solution is equal to the vapor pressure of this pure

component (P^*) multiplied by the molar mixing ratio in the solution. For non-ideal solution, such as the NH_3-H_2O system, Raoult's law applies to the limiting case when the solute (ammonia) is in large excess. That is to say:

$$\text{Raoult's law:} \qquad \lim_{c\to 1} P(c,T) \to cP^*(T) \tag{4.25}$$

Various empirical functions have been developed to calculate the partial vapor pressures of ammonia and water as a function of temperature and ammonia concentration in the liquid: Weidenschilling and Lewis (1973) used a fifth-order polynomial and Atreya and Romani (1985) used a spline interpolation of twenty coefficients. We find that it is unnecessary to use a complicated expression because Henry's law adequately describes how ammonia dissolves into water for a wide range of possible compositions of Jupiter's atmosphere. So we design a simple empirical function that only depends on one parameter, Henry's law coefficient $k_H(T)$. The formula is:

$$P(c,T) = \left(\frac{P^*(T) - k_H(T)}{2} \times \cos\big(\pi(1-c)\big) + \frac{P^*(T) + k_H(T)}{2}\right) c\,. \tag{4.26}$$

It is easy to verify that the function asymptotically converges to Henry's law at the low end of the concentration and converges to Raoult's law at the high end with a continuous derivative:

$$\begin{gathered} P(0,T) = 0, P(1,T) = P^*(T)\,, \\ \partial_c P(c,T)|_{c=0} = k_H(T), \partial_c P(c,T)|_{c=1} = P^*(T)\,. \end{gathered} \tag{4.27}$$

Figure 4.3 shows the excellent agreement between the partial pressures calculated by formula (4.26) and the laboratory measurements. If both water and ammonia have five

times solar abundance – 4.7×10^{-3} and 6.5×10^{-4} in molar mixing ratio respectively – Jupiter's water cloud forms at around 7 bars at 300 K. Partial pressure of ammonia near the water cloud bottom is $P(c,T) = 6.5 \times 10^{-4} \times 7 \times 10^{5} = 455$ pa. Using equation (4.26) to solve for c at $T = 300$ K gives $c = 4.5 \times 10^{-3}$. The molar amount of ammonia dissolved in the water cloud is proportional to the total amount of liquid in the cloud, which is highly unknown. But the maximum molar amount of dissolved NH_3 in the liquid in one mole of gas, by assuming all water condenses as liquid at the cloud bottom, is about $4.5 \times 10^{-3} \times 4.7 \times 10^{-3}\text{mol} = 1.8 \times 10^{-5}$ mol, which is about 3% of the total amount of NH_3 vapor. Moreover, the "fresh" cloud model developed by Wong et al. (2015) predicts orders of magnitude fewer cloud particles than the maximum amount of possible cloud calculated by the equilibrium condensation model. Because of the large uncertainty on the amount of cloud and the small value of possible dissolved ammonia, incorporating the solution chemistry will improve neither the temperature profile nor the vertical distribution of NH_3. Thus, the solution chemistry described in this section is not included in the nominal thermodynamic model, but will be provided as an option for future investigation.

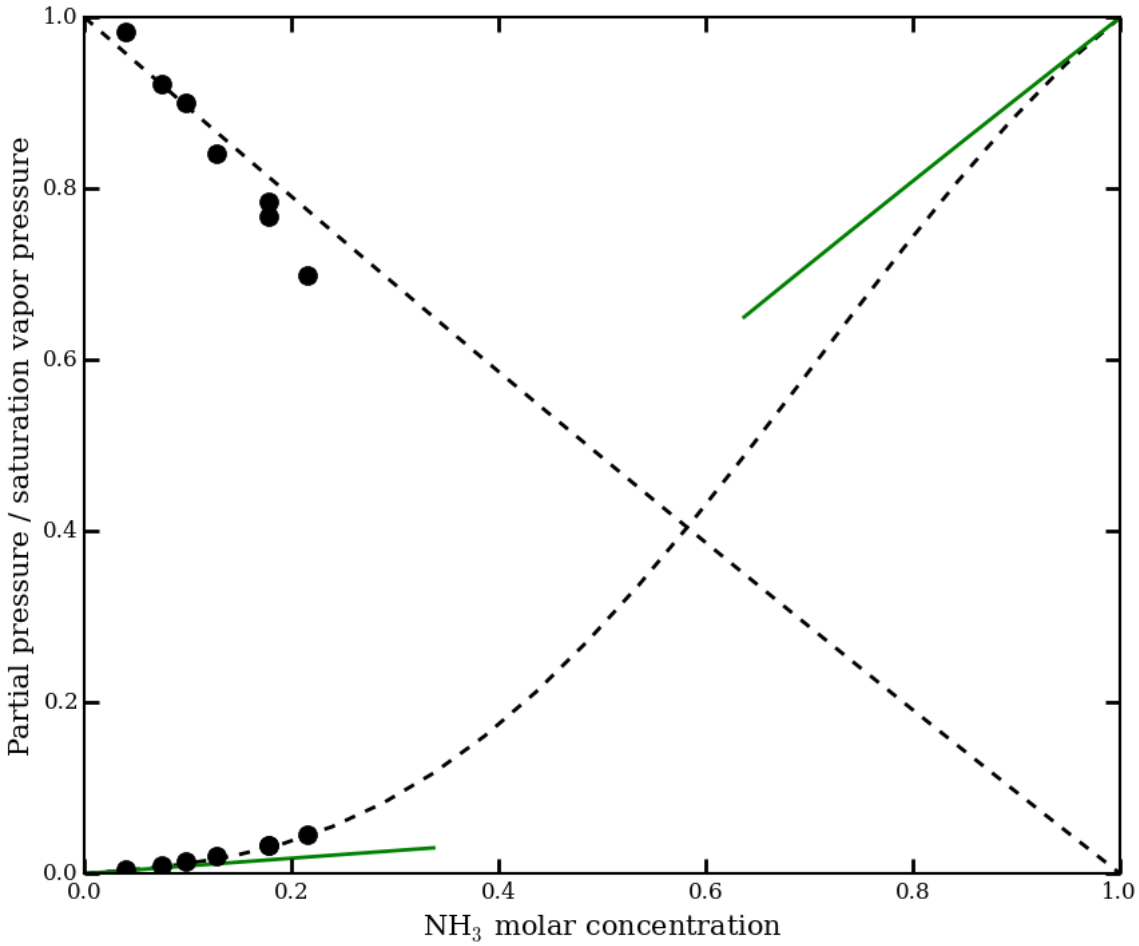

Figure 4.3 Partial pressure of ammonia and water over aqueous ammonia solution at 300 K. The dashed line going from bottom left to top right is the partial pressure of ammonia over the saturation vapor pressure of pure ammonia. The dashed line going from top left to bottom right is that of water. Two green lines indicate the Henry's law limit (bottom) and Raoult's law limit (top). The Henry's law constant is 10^5. Blacks dots are laboratory measurements (Perman, 1903)

4.3.3 NH_4SH cloud

The chemical reaction that forms the solid NH_4SH cloud is:

$$\mathrm{NH_3(g) + H_2S(g) == NH_4SH(s)}\,, \tag{4.28}$$

where "g" stands for gas phase and "s" stands for solid phase. It forms when the product of the partial pressure of NH_3 and H_2S exceeds an equilibrium constant (K), which is given in Lewis (1969) by:

$$\ln K = 14.82 - \frac{4705}{T}. \tag{4.29}$$

This reaction is predicted by the chemical equilibrium model and was confirmed in the laboratory experiment (Magnusson, 1907). Yet, whether this cloud layer exists on Jupiter is still controversial. Another form of cloud that might condense is $(NH_4)_2S$ (personal communication with Sushil Atreya and Maarten Roos). The details of this reaction and how it removes H_2S gas were described in Weidenschilling and Lewis (1973), and will not be repeated here. Instead, we emphasize that including the condensation of the NH_4SH cloud will reduce the amount of NH_3 gas by 12%, so this reaction must be taken into account for the accurate modeling of the thermodynamic process. Adding this reaction into our previous entropy formulation is straightforward. Similar to equation (4.3), we wrote the entropy of NH_4SH solid as:

$$S_{\mathrm{NH_4SH}}(T,P) = S_{\mathrm{NH_3}}(T,P) + S_{\mathrm{H_2S}}(T,P) - \frac{L_{\mathrm{NH_4SH}}(T)}{T}. \tag{4.30}$$

The entropy of the NH_4SH cloud is:

$$x_{\mathrm{NH_4SH}}\left(S_{\mathrm{NH_3}}(T,P)+S_{\mathrm{H_2S}}(T,P)-\frac{L_{\mathrm{NH_4SH}}(T)}{T}\right)$$
$$=x_{\mathrm{NH_4SH}}S_{\mathrm{NH_3}}(T,P)+x_{\mathrm{NH_4SH}}S_{\mathrm{H_2S}}(T,P)-x_{\mathrm{NH_4SH}}\frac{L_{\mathrm{NH_4SH}}(T)}{T}. \quad (4.31)$$

Define $x_{t_{\mathrm{NH3}}}=x_{v_{\mathrm{NH_3}}}+x_{c_{\mathrm{NH_3}}}+x_{\mathrm{NH_4SH}}$ and $x_{t_{\mathrm{H_2S}}}=x_{v_{\mathrm{H_2S}}}+x_{c_{\mathrm{H_2}S}}+x_{\mathrm{NH_4SH}}$ as the total molar mixing ratio of NH_3 and H_2S. Equation (4.5) bears the same expression after combining the first two terms into the first summation and the third term in the second summation. Therefore, the expression for entropy, equation (4.9), is correct when the NH_4SH cloud is added in as the latent heat term.

4.3.4 Numerical method and model verification

There are two ways to calculate the moist adiabatic profile. One way is to integrate equation (4.22) vertically, while keeping track of the condensed species. This method is faster to calculate, but its accuracy depends on the vertical resolution, especially on the ability to locate the cloud bottom. Large numerical errors will be introduced if the cloud bottom is off by one grid point. In order to calculate the moist adiabatic profile accurately, one has to insert numerical grids to represent the cloud bottom adaptively. Another drawback of this method is that it fails to calculate the triple point equilibrium correctly. At the triple point of one substance, the temperature gradient is zero. The liquid phase coexists with the solid phase to keep a constant temperature and partial pressure. This process is not accounted for in equation (4.22).

Those drawbacks are avoided by using an alternative approach, which is to solve equation (4.9) directly for a constant θ, including the constraints from condensation of clouds. Because equation (4.9) is nonlinear, an iterative method shall be used. At a specified pressure, the iteration starts from an initial guess of temperature. Then the saturation vapor pressure of a condensable species is calculated. If it is smaller than the partial vapor pressure, the species condenses either to a liquid or to a solid depending on the temperature. The condensing process is done sequentially for all condensable species to reach an equilibrium state. This process has to be repeated several times because condensation of one species will change the partial pressure of the others. After that, the entropy is computed for the equilibrium state. If the entropy is not the same as the required entropy, another iteration begins with an updated temperature calculated by the secant method. The iteration usually converges in a few tens of steps.

Special consideration needs to be applied at the triple point, because the above method only applies to a pure liquid phase or solid phase. In the fusion process, entropy takes a finite jump between those two states although temperature maintains. If the required entropy is in the middle of the above two situations, the iteration will stop at the correct temperature but the partitioning of liquid and solid is not right. A practical and elegant way to handle the triple point equilibrium is to calculate two equilibrium states at $T_1 = T_{tr} + \Delta T$ and $T_2 = T_{tr} - \Delta T$, representing a pure liquid phase and a pure solid phase. T_{tr} is the triple point temperature and $\Delta T = 10^{-4}$ is a very small number. Because entropy is a linear function of mixing ratio during fusion, the equilibrium state at the triple point is given by a linear interpolation between the liquid state and the solid state:

$$x = \frac{s_2 - s_0}{s_2 - s_1} x_1 + \frac{s_0 - s_1}{s_2 - s_1} x_2 \,, \tag{4.32}$$

where x is the molar mixing ratio; s_1 and s_2 are the entropies at two states; s_0 is the required entropy.

Since potential temperature is explicitly conserved, all calculated thermodynamic quantities are precise to machine precision. Moreover, the later method opens up a simple and flexible way to calculate the secondary alteration of the atmosphere by dynamics or microphysics. For example, it would be straightforward to calculate the temperature profile, given a prescribed distribution of potential temperature. Due to the benefits above, we use the second method in our thermodynamic model.

We test the correctness of our model by comparing the adiabatic lapse rate against the analytical solution of temperature gradient derived in equation (4.22). The gases included in the nominal Jovian atmosphere are H_2, He, CH_4, NH_3, H_2S and H_2O. Their solar abundances, standard enrichment factors and heat capacities are listed in Table 4.1. The heat capacity of hydrogen depends upon the ratio of ortho-hydrogen to para-hydrogen, and upon the rate at which they equilibrate (Conrath and Gierasch, 1984; Massie and Hunten, 1982). For a simple and benchmark calculation, we assume that the ortho- to para- ratio is fixed at 3:1 (normal hydrogen) and the heat capacities for other species are constant. The condensed phases are NH_3(l), NH_3(s), H_2O(l), H_2O(s), NH_4SH(s), where "l" stands for liquid phase. NH_3(l) only exists in the form of liquid solution when solution chemistry is

enabled. The formula for calculating saturation vapor pressures and the associated latent heats are provided in Table 4.2. The adiabatic temperature profile is generated to match a target temperature at the one-bar level. Currently, it is chosen to be 166 K (Seiff et al., 1998). Figure 4.4 (a) shows the vertical profiles of NH_3, H_2O and H_2S. H_2O, NH_4SH and NH_3 cloud layers form at 7.6 bar, 2.4 bar and 0.83 bar, respectively. A small but visible kink near water mixing ratio equals 10^{-3} is due to triple point equilibrium. The increase of temperature due to freezing is recognized as a horizontal segment in the dry potential temperature profile in Figure 4.4 (b). Figure 4.4 (c) compares the numerical adiabatic lapse rate and its analytical value calculated by equation (4.22). They match exactly except for two places: one is at the triple point of water and the other is at the NH_4SH cloud base. The analytic solution converges to the numerical solution at the wings near the triple point. Because the formation of NH_4SH cloud does not satisfy the Clausius-Clapeyron relation the analytic solution cannot be applied to NH_4SH condensation. For the expression of lapse rate including NH_4SH cloud, readers are referred to Atreya and Romani (1985).

Table 4.1 Standard Jovian atmosphere.

Molecule	Solar abundance (relative to H_2)	Enrichment factor (relative to solar)	Heat capacity (J mol^{-1} K^{-1})
H_2	1.	1.	21.8-28.9
He	0.1941	0.808	20.79
CH_4	6.04×10^{-4}	3.92	35.76
NH_3	1.52×10^{-4}	5.00	35.70
H_2S	2.96×10^{-5}	3.01	34.22

H_2O	1.10×10^{-3}	5.00	33.50

Table 4.2 Saturation vapor pressure and latent heat. The unit of P_{NH_3} or P_{H_2S} in the last expression is bar, otherwise it is dyn/cm^2. The value of latent heat is evaluated at triple point. The latent heat at an arbitrary temperature is calculated using equation (4.4).

Condensation	Saturation vapor pressure ($\ln \mathrm{dyn/cm^2}$):	Latent heat (J mol^{-1})
$H_2O(g) == H_2O(s)$	$\ln P_{H_2O} = -\frac{5631.12}{T} - 8.3636 + 8.2312 \ln T - 3.8614 \times 10^{-2}\, T + 2.7749 \times 10^{-5}\, T^2$	51.01
$H_2O(g) == H_2O(l)$	$\ln P_{H_2O} = -\frac{2313.0}{T} - 164.03 + 38.054 \ln T - 1.3844 \times 10^{-1}\, T + 7.4465 \times 10^{-5}\, T^2$	45.01
$NH_3(g) == NH_3(s)$	$\ln P_{NH_3} = -\frac{4122.0}{T} + 41.679 - 1.8163 \ln T$	31.20
$NH_3(g) == NH_3(l)$	$\ln P_{NH_3} = -\frac{4409.4}{T} + 76.864 - 8.4598 \ln T + 5.5103 \times 10^{-3}\, T + 6.8046 \times 10^{-6}\, T^2$	23.50
$NH_3(g) + H_2S(g) == NH_3SH(s)$	$\ln P_{NH_3} + \ln P_{H_2S} = 14.82 - \frac{4705}{T}$	93.12

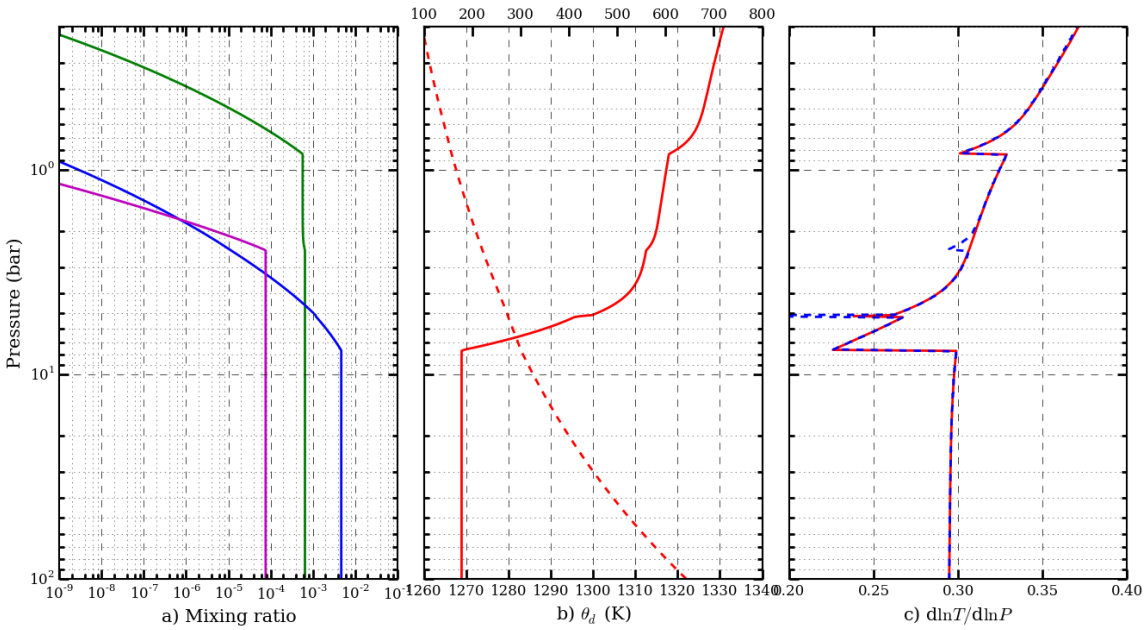

Figure 4.4 Standard Jovian troposphere. Panel (a): vertical distribution of NH_3 (green), H_2S (magenta) and H_2O (blue); their enrichment factors are 5, 3 and 5 respectively. Panel (b): temperature (dashed line, top axis) and dry potential temperature (solid line, bottom axis) profiles. The dry potential temperature is referenced at 1000 bar and is defined in equation (4.11). Panel (c): numerical and analytical adiabatic lapse rate. Blue dashed line is an approximation of adiabatic lapse rate by finite difference using the temperature profile in panel (b). Red solid line is the analytical solution in equation (4.22).

4.4 Dynamic parameterization

The Juno/MWR measures brightness temperature at six wavelengths and multiple limb angles. We cannot expect to extract more than six pieces of information from the spectra, and we will probably extract fewer than six. Moreover, the opacity in these wavelengths is dominated by ammonia absorption, and that of water is ten times smaller. As a result, the signal of water in the microwave spectrum resides in the change of lapse rate when water condenses. Studying the possible dynamic effect on shaping the temperature and distribution of ammonia is indispensable for correctly interpreting the Juno/MWR observations. This section discusses two scalar parameters that reflect the dynamic alteration of the atmosphere. We will demonstrate that these two parameters cover a wide range of atmospheric conditions including the Galileo Probe site, moist adiabat and dry adiabat.

4.4.1 Stretch parameter

The stretch parameter (S) is motivated by observations from the Galileo probe, by the numerical experiment that shows a downward deflection of material surfaces (vertical stretching of the air column) in Showman and Dowling (2000), and by an analytical wave saturation model by Friedson (2005). We simplify the dynamic distortion of the material surface to a scalar "stretch parameter" (S), so that the final pressure of the material surface (p_2) is S times its original pressure (p_1) : $p_2 = S \times p_1$. During the vertical stretch of the column, air parcels conserve their potential temperature and moisture contents. The stretch parameter effectively reduces the relative humidity of the atmosphere while maintaining the magnitude of stratification. We find that the vertical abundances of NH_3, H_2S and H_2O

measured in situ by the Galileo Probe are consistent with $S = 4$ (shown in Figure 4.5). Moreover, statically stable layers predicted by equilibrium condensation are preserved but displaced to higher pressures. In our stretched model, three stable layers occur at ~1.5 bars, ~7 bars and ~17 bars, which match the locations of stable layers at 0.5-1.7 bars, 3-8.5 bars and 14-20 bars derived by Magalhaes et al. (2002) from the *T*-sensor data of the Galileo probe. Because the value $S = 1$ gives an unaltered saturated moist adiabat, and $S = 4$ gives the observed mixing ratios of NH_3, H_2S, and H_2O from the Galileo, by varying *S*, one can model any profile in between.

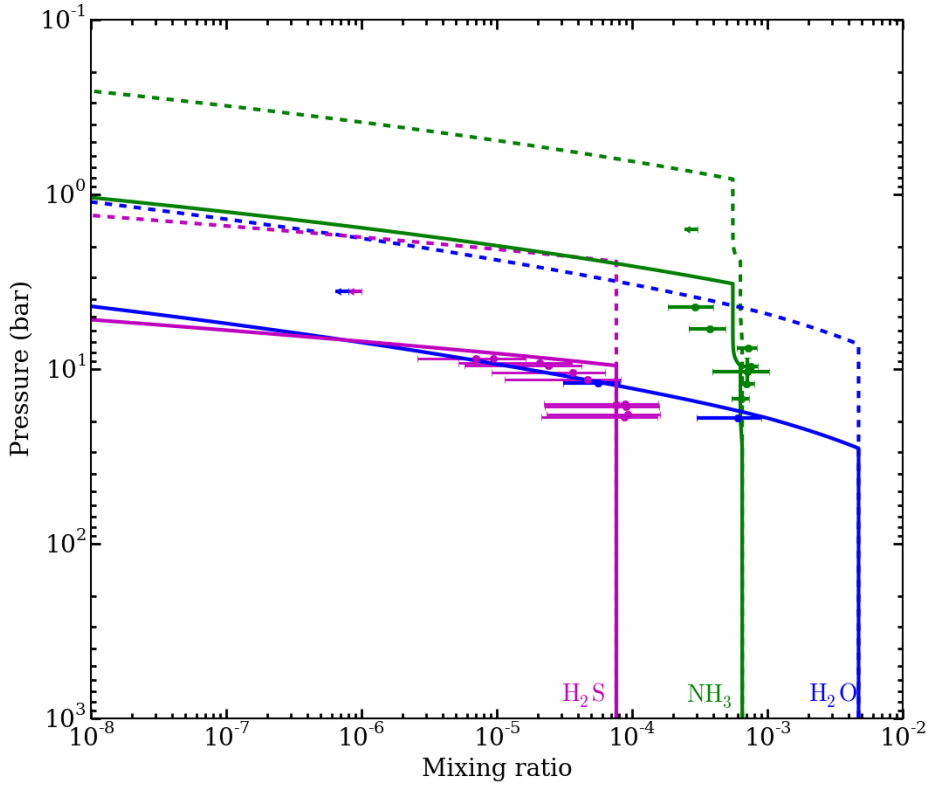

Figure 4.5 Galileo probe results fitted by stretch parameter $S = 4$. Green lines represent NH3 mixing ratio; blue lines represent H_2O mixing ratio and magenta lines represent H_2S mixing ratio. Dashed lines show the equilibrium condensation model with five times solar abundance for both NH_3 and H_2O. They do not match the Galileo probe results (Wong et al., 2004), which are the data points with error bars. The uppermost NH_3 point is simply an upper bound. Solid lines show the same amount of enrichment but with $S = 4$.

We constructed several typical atmospheric profiles and performed pencil beam radiative transfer calculations using the molecular opacity in Juno Atmosphere Model and Radiative Transfer (JAMRT) code to identify parameter sensitivity. Figure 4.6 illustrates the sensitive channels for NH_3, H_2O and stretch parameter. The signal of the stretch parameter is largest in small wavelength channels (< 8 cm) and vanishes at wavelengths longer than 40 cm. This is because the effect of vertical stretching subsides in the subcloud layer, where the mixing ratio and potential temperature is constant. The signal of water is weak but noticeable at wavelengths from 8 cm to 40 cm when $S = 1$. However, the signal of water disappears when $S > 2$ (not shown). As a result, retrieving the stretch parameter helps to identify the place where the dynamic alteration is the least ($S \approx 1$) and is therefore suitable for the retrieval of deep water abundance. The signal of ammonia dominates all spectra because it is the major absorber. Since both stretching and water have little effect on the wavelength longer than 40 cm, the long wavelength channel can be used to determine the deep abundance of ammonia.

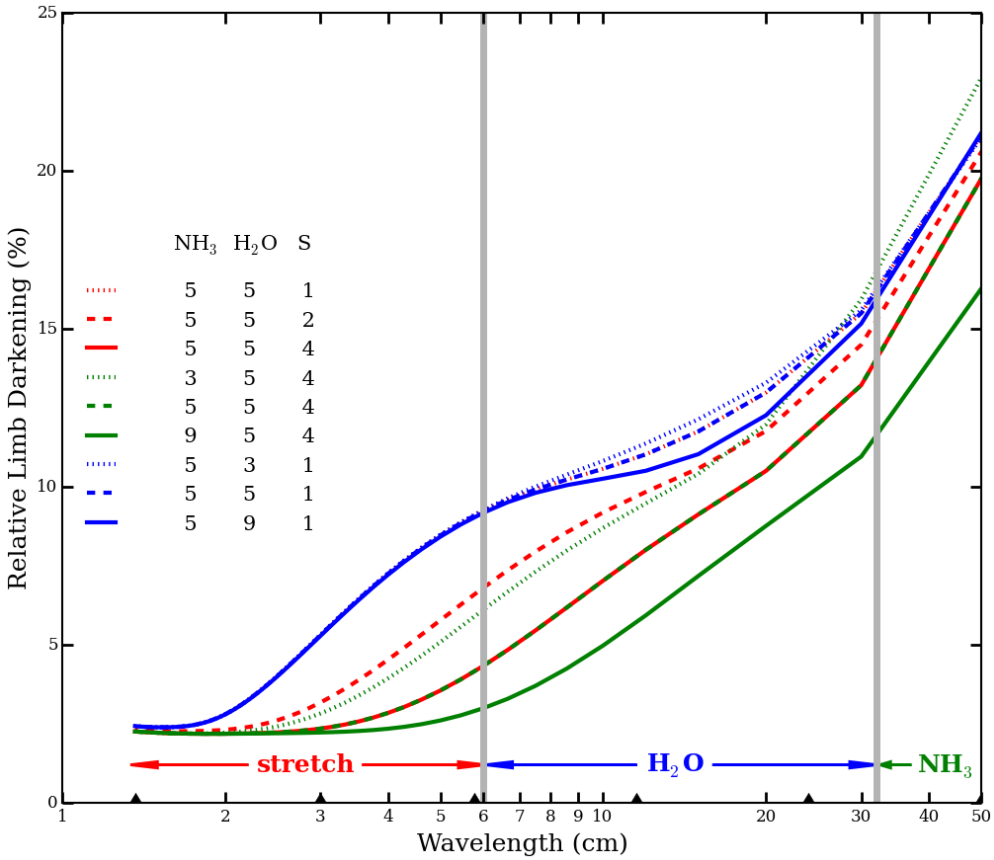

Figure 4.6 Sensitive channels for NH_3, H_2O, and stretch parameter. Lines in the figure show synthetic Juno/MWR measurements and they are grouped in three colors. Red curves represent varying the stretch parameter while keeping H_2O and NH_3 constant. Blue curves represent varying the H_2O abundance while keeping NH_3 and stretch constant. Green curves represent varying the NH_3 abundance while keeping H_2O and stretch constant. Black triangles at the bottom mark the wavelengths of Juno/MWR. The sensitive channels for each parameter are indicated in the figure.

4.4.2 Mixing parameter

Another possible parameter is the mixing parameter (M), which linearly scales the potential temperature profile $\theta_s(p)$ from a stretched moist adiabat to a dry adiabat according to the expression:

$$\theta(p) = M\theta_0 + (1 - M)\theta_s(p), 0 \leq M \leq 1, \quad (4.33)$$

where θ_0 is the potential temperature in the subcloud layer, representing a dry adiabat, and $\theta_s(p)$ is the potential temperature profile of a stretched moist adiabat. After the temperature profile $\theta(p)$ is constructed. The mixing ratios of NH_3 and H_2O in the result profile are equal to those in the stretched moist adiabat. The purpose of designing this mixing parameter is to investigate the effect of temperature only while keeping the same moisture as the stretched moist adiabat. Therefore we can have another variable to change that complements the stretch parameter, as illustrated in Figure 4.7.

Given a reference temperature and pressure (T_r, P_r) at the top of troposphere, the temperature profile of the whole troposphere is bounded by two end members in the formula, with $M = 0$ being a moist adiabat and $M = 1$ being a dry adiabat. Though a saturated atmosphere with a dry adiabatic lapse rate would be unstable and unrealistic, it defines the upper limit of the brightness temperature for a saturated atmosphere because temperature is given at the top. An unsaturated atmosphere with a dry adiabatic lapse rate can be stable and is possible to exist. The mixing parameter explores such possibilities.

In the presence of both stretch and mixing, we first apply the stretch parameter to create a stretched and unsaturated atmosphere $\theta_s(p)$. Then, we apply equation (4.33) to scale the potential temperature profile (M). The former process represents the vertical displacement of an air parcel caused by atmospheric waves and the latter process represents the possible reduction of temperature gradient by mixing. Figure 4.7 shows the nadir brightness temperature residuals relative to a brightness temperature distribution obtained from a reversible moist adiabatic atmosphere. Being relatively orthogonal to the effect of

stretching, the effect of mixing increases with wavelength because the temperature difference between the moist and dry adiabat is largest in the subcloud layer if the temperature is given at the top.

Physically, the mixing process also complements the stretch process because mixing changes the magnitude of stratification but not the location of the stratified layer, while stretching alters the latter instead of the former. *M* and *S* separate two major factors contributing to how Jupiter's atmosphere is stratified.

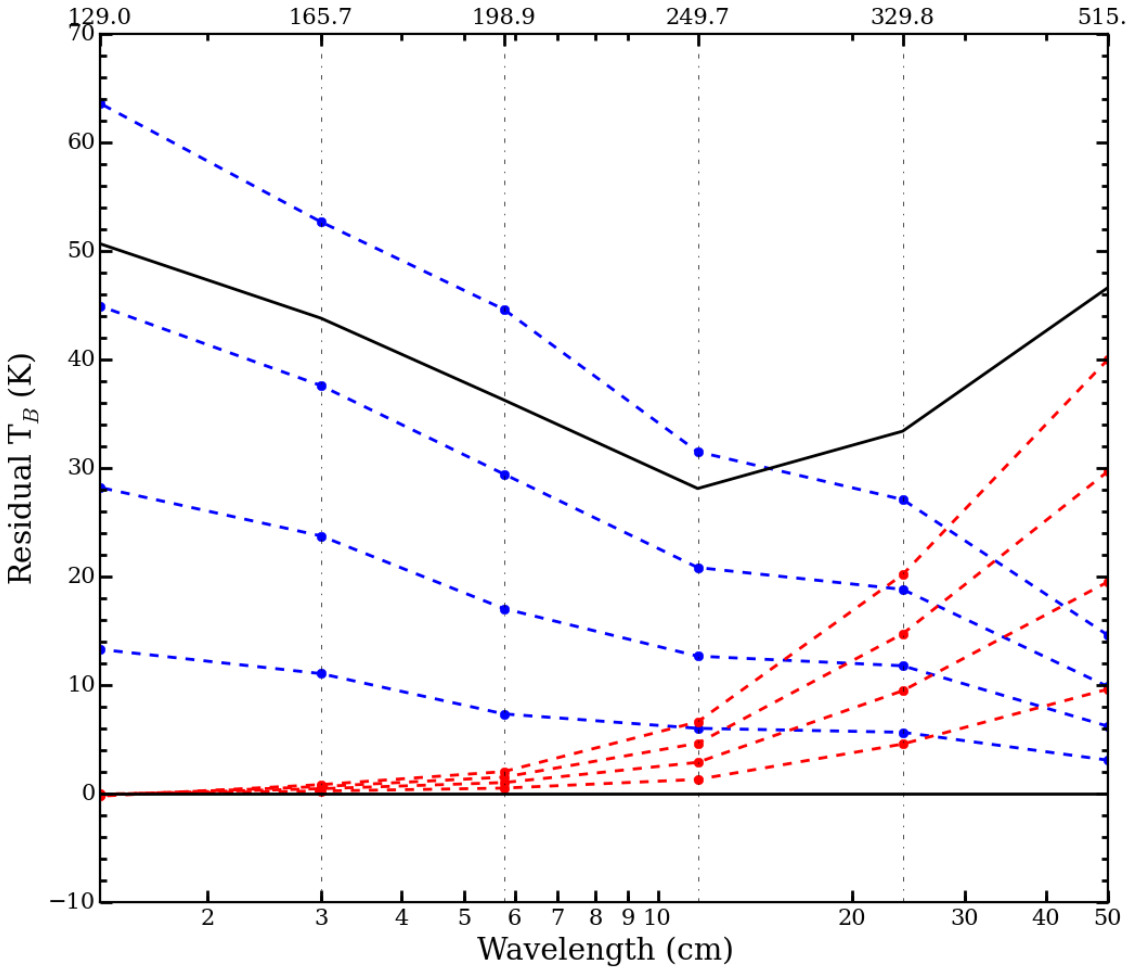

Figure 4.7 Residual nadir brightness temperature (T_B) distribution. Blue dashed lines show the residual T_B distribution of several stretched atmospheres (S = 1.3, 2, 2.8 and 4 from bottom to top). Red dashed lines show several mixed atmospheres (M = 0.25, 0.5, 0.75 and 1) from bottom to top. The black solid line indicates the atmosphere with S = 4 and M = 1. Numbers at the top axis are the nadir brightness temperature of a reversible moist adiabat.

4.5 Retrieval method and results

In order to receive signals from great depths, the Juno/MWR must sample a portion of the spectrum where the absorption coefficients are weak and the spectral features are nearly absent. Therefore, the retrieved parameters from the spectra are usually highly correlated. The prevailing method of fitting the microwave spectra is still done by forward modeling and trial-and-error. Here we use the Markov Chain Monte Carlo (MCMC) method (Goodman and Weare, 2010) to fit the spectra. The MCMC method is adept at overcoming local extrema and obtaining a global extremum. In addition, it computes the complete joint probability distribution between parameters, and can be displayed graphically. The application of the MCMC method to retrieval problems in astrophysics has been successfully implemented and tested in the literature, including a detailed comparison of the strengths and weakness against a more traditional Levenberg-Marquardt method (Line et al., 2013). However, the application of the MCMC method toward inverting the microwave spectra has not yet been studied. This novel approach explores a new field in microwave spectrometry.

We model the synthetic observation by

$$\widetilde{T_B}(\lambda_i, \theta_j) = T_B(\lambda_i, \theta_j)\big(1 + \epsilon(\lambda_i)\big) + \gamma(\lambda_i, \theta_j)\,, \tag{4.34}$$

where $\widetilde{T_B}(\lambda_i, \theta_j)$ is the synthetic observation of brightness temperature at wavelength λ_i and limb angle θ_j, with $T_B(\lambda_i, \theta_j)$ being the true brightness temperature. Two types of noise terms, $\epsilon(\lambda_i)$ and (λ_i, θ_j) , represent the fractional error in brightness temperature and the absolute error in limb darkening, respectively. They have zero means and are

independent. Their standard deviations are 3% and 0.5 K respectively (Janssen et al., 2005). The covariance matrix is

$$\Sigma(i;j,i';j') = T_B(\lambda_i,\theta_j)T_B(\lambda_{i'},\theta_{j'})\mathrm{Var}(\epsilon)\delta_{ii'} + \mathrm{Var}(\gamma)\delta_{ii'}\delta_{jj'}\,, \qquad (4.35)$$

where δ_{ij} is the Kronecker delta, and Var stands for variance. The state vector is composed of five parameters: *X* is the deep ammonia mixing ratio, *Y* is the deep water mixing ratio (both are ratios to solar abundance), *S* is the stretch parameter and *M* is the mixing parameter, Θ is the temperature at the one-bar level, which can be estimated from ground based observations. Assuming ϵ and γ have Gaussian statistics, the log probability of an observation is:

$$\ln P\left(\widetilde{T_B} \mid X,Y,S,M,\Theta\right) \propto -\frac{1}{2}\left(\widetilde{T_B}-T_B\right)^T\Sigma^{-1}\left(\widetilde{T_B}-T_B\right) - \frac{1}{2}\ln|\Sigma|\,. \qquad (4.36)$$

Using Bayes' theorem, the log probability of parameters given an observation is:

$$\begin{aligned}\ln P(X,Y,S,M,\Theta|\,\widetilde{T_B}) \propto{}& \ln P\left(\widetilde{T_B} \mid X,Y,S,M,\Theta\right)\\ &+ \ln P(X) + \ln P(Y) + \ln P(S) + \ln P(M)\\ &+ \ln P(\Theta)\,.\end{aligned} \qquad (4.37)$$

The last five terms are the prior probabilities of the five parameters. The MCMC algorithm randomly draws (X,Y,S,M,Θ) from possible combinations in parameter space and adds the new state to the Markov chain – a sequence of states that are generated – if the probability calculated by equation (4.36) is greater than the previous one, otherwise the new state will be added to the Markov chain contingent on a number known as the acceptance ratio. The final statistics is obtained by gathering all states in the chain. The number density of the states in the parameter space is propotional to the posterior probability.

In the current stage, we test the retrieval result on a pencil beam radiation model, though the real beam pattern has a finite width and may observe spatially inhomogeneous atmospheres. First, we study a normal situation with moderate stretch and mixing. Five limb angles starting from the nadir and separated by 15^o are considered. The deep ammonia (*X*) and water (*Y*) abundances are set to be 5 times solar; the stretch parameter (*S*) is 2; the mixing parameter (*M*) is 0.5. Temperature at one bar level (Θ) is 166 K (Seiff et al., 1998). Synthetic spectrum is generated according to equation (4.34). Prior probabilities for (*X*, *Y*, *S* and *M*) are chosen to be uniformly distributed within $0 \leq X \leq 10, 0 \leq Y \leq 20, 1 \leq S \leq 5$ and $0 \leq M \leq 1$. The prior probability for Θ is a Gaussian distribution with a mean of 166 K and a standard deviation of 1 K. The algorithm uses 24 Markov chains with 20,000 states in each chain to explore the entire parameter space. We will express the fitted result and uncertainties in the symbol $A^{+\sigma}_{-\delta}$, where $A-\delta, A,$ and $A+\sigma$ represent the 16th, 50th and 84th percentile of the samples in the marginal distribution.

Figure 4.8 shows the joint distribution between all pairs of parameters and the marginal distribution of each parameter. It is not surprising to see that the ammonia abundance ($4.96^{+0.19}_{-0.09}$) and the stretch parameter ($2.03^{+0.17}_{-0.11}$) are well constrained, as ammonia is the major absorber. Their marginal posterior distributions are almost symmetric about the mean value. The water abundance is reasonably constrained to $4.55^{+3.11}_{-1.55}$ times solar, given that the true value is 5. The mixing parameter ($0.48^{+0.24}_{-0.29}$) is poorly constrained and has a large correlation with the water abundance. This is because adding water reduces the lapse rate, and mixing with a dry adiabat increases it. Thus high water and high mixing ratio

produce nearly the same brightness temperature as low water and low mixing ratio. The correlation between water and mixing is skewed. Water abundance is slightly biased toward low values when mixing is small (< 0.7) and largely biased toward high values when mixing is large (> 0.7). Another important result from this study is that Θ is independent of *X*, *Y*, *S* and *M*, which is equivalent to saying

$$P(\Theta, X, Y, S, M) = P(\Theta) \times P(X, Y, S, M)\,. \tag{4.38}$$

This is because the limb darkening depends more on the relative humidity of ammonia and changes in the lapse rate but less on the absolute temperature. The independence of Θ and other parameters allows a large tolerance on the error in estimating the temperature of the moist adiabat at 1 bar level, i.e. the posterior distributions of (*X*, *Y*, *S* and *M*) will be the same for any reasonable value of Θ.

Second, we study an extreme situation where the temperature profile is a dry adiabat ($M = 1$). Other parameters remain the same. Because of the independency, we don't retrieve the value of Θ in this study. The posterior distributions are displayed in Figure 4.9. Like the normal case, the ammonia abundance ($4.75^{+0.16}_{-0.07}$) and the stretch parameter ($1.85^{+0.10}_{-0.08}$) are adequately retrieved but the water abundance is severely biased toward low values ($1.49^{+2.61}_{-1.02}$). The distribution of the mixing parameter ($0.79^{+0.16}_{-0.43}$) peaks at $M = 1$ and has a long tail toward $M = 0$. On the other hand, even for the extreme situation, it is possible to put an upper limit on the water abundance (high values of water would be unlikely) and the mixing parameter indicates whether we are in such an extreme situation.

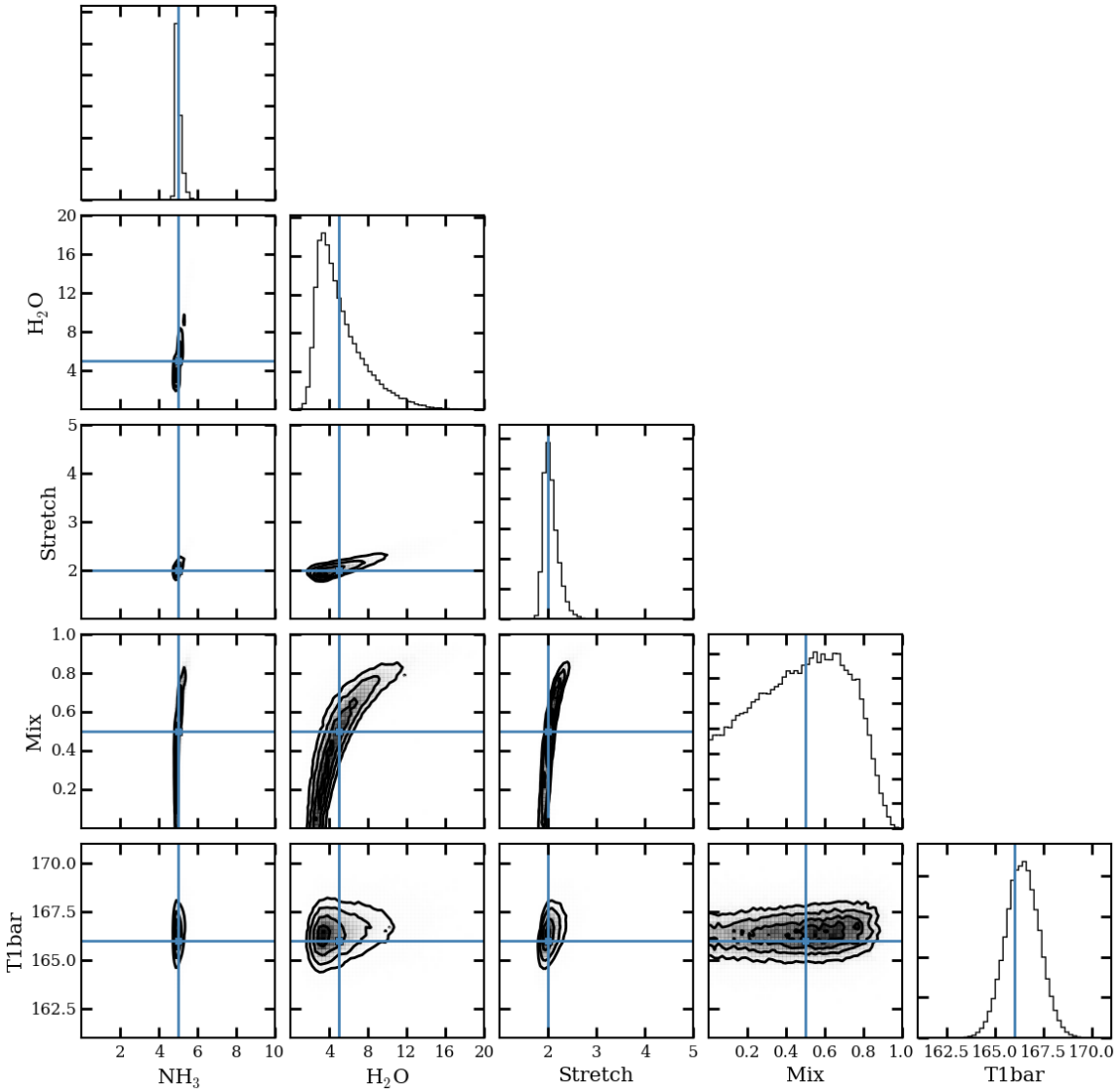

Figure 4.8 Joint and marginal probability distribution of parameters. Each panel with shaded contours shows the joint distribution (covariance) of two parameters in the state vector. The contours show the number density of samplings. The panels in the diagonal show the normalized marginal distribution of a single parameter. The blue lines show the true values of the parameters used to generate the synthetic data.

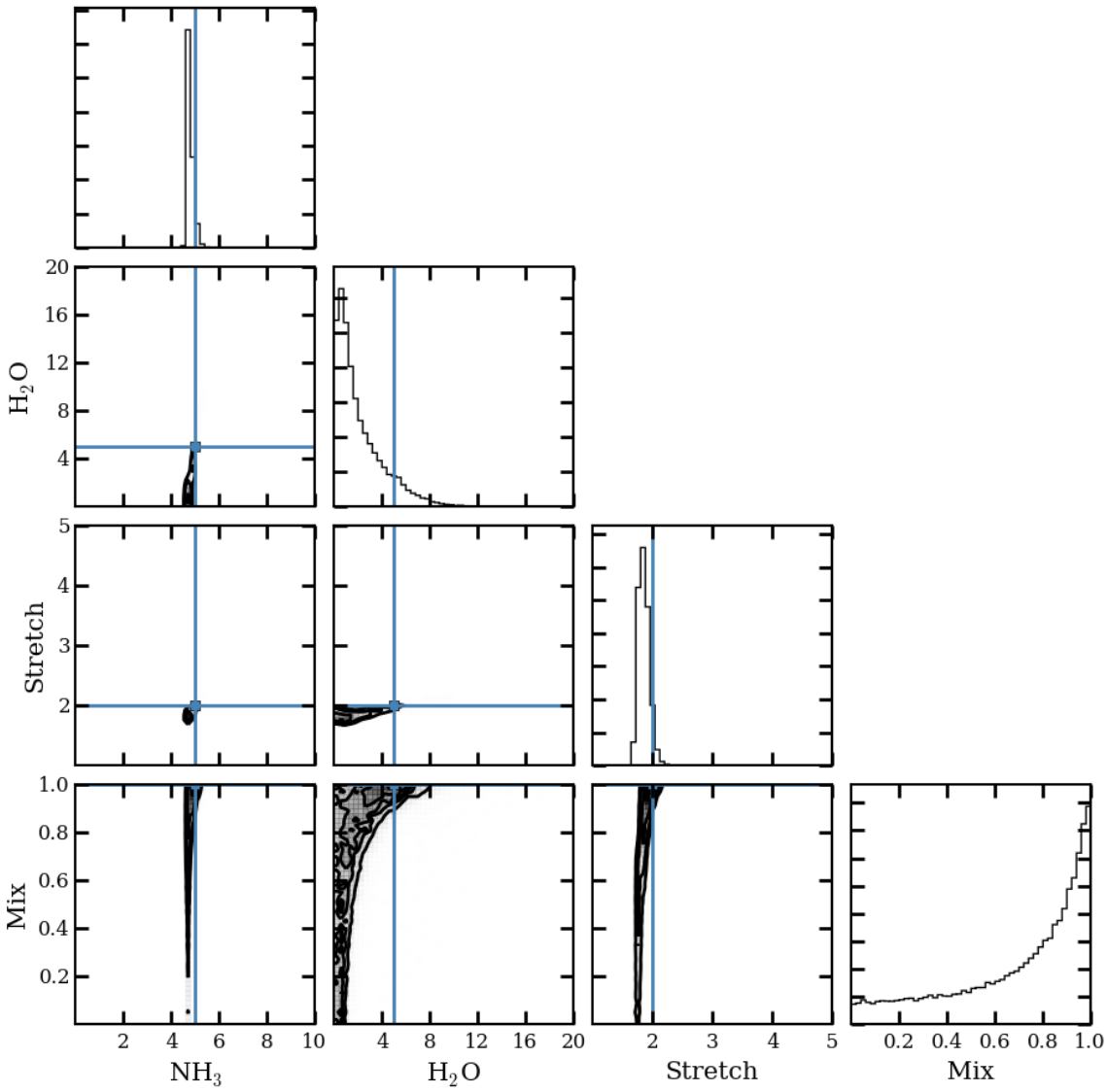

Figure 4.9 Similar to Figure 4.8, but for an extreme situation (dry adiabat $M = 1$).

4.6 Conclusion

In this chapter, we reviewed the calculation of moist adiabatic lapse rate and various assumptions involved in deriving the expression. We pointed out a general expression that holds for multiple condensable species, varying heat capacity and arbitrary number of mixtures. We discussed the importance of aqueous ammonia solution and the formation of NH_4SH cloud. We found that less than 3% of ammonia gas will dissolve in water cloud and it is very likely that the number will be orders of magnitude lower (Wang et al., 2015). Therefore ammonia solution is not important for the calculation of temperature profile and the distribution of ammonia gas. On the contrary, the NH_4SH cloud will reduce the amount of ammonia gas by 12%, which is significant for an accurate thermodynamic modeling of Jupiter's atmosphere.

We introduced two dynamic parameters that alter the atmosphere from the equilibrium condensation model. The stretch parameter (S) describes the vertical displacement of an air parcel. We found that the distribution of NH_3, H_2S and H_2O measured by the Galileo Probe can all be fitted by $S = 4$. The mixing parameter (M) scales the atmospheric temperature profile from a dry adiabat to a moist adiabat. Their effects are complementary because the former alters the location of a stratified layer and the latter alters the magnitude of the stratification. Given the polar orbits of Juno, it is then possible to extract the dynamic information from the spectrum and construct a latitudinal profile of dynamic parameters. This approach extends the Juno/MWR's functionality: from retrieving the deep water abundance to retrieving the latitudinally varying dynamic effects. These observational

constraints are crucial for understanding subcloud dynamics that we have never seen before.

We investigated the application of the Markov Chain Monte Carlo (MCMC) method to the inversion of microwave spectra. Five variables are included in the retrieval: the deep ammonia mixing ratio (*X*), the deep water mixing ratio (*Y*), stretch parameter (*S*), mixing parameter (*M*) and temperature at 1 bar level (Θ). The posterior joint distribution shows that Θ is independent of X, Y, S and M. Errors in estimation of Θ will not affect the results of other parameters. Ammonia abundance and the stretch parameter can be well determined from the spectra. For a normal situation (close to moist adiabat), water abundance is constrained to the accuracy of +3.1/-1.5 times solar. For an extreme situation (close to dry adiabat), water abundance is constrained to an upper limit.

4.7 Appendix

4.7.1 Derive moist adiabatic lapse rate using differential forms of thermodynamic laws

We use the differential form of thermodynamic equation to derive the equation (4.22). For simplicity, the symbols used in this derivation has small differences compared to the main section. We will use subscript *d* for dry gas, *i* for condensable species and *c* for clouds. Their molar concentrations are x_d, x_i and x_c respectively. P_d is the pressure of dry gas. e_i and L_i is the saturation vapor pressure and latent heat for *i*-th species. From the first law of thermodynamics:

$$0 = T\mathrm{d}s = \bar{c_p}\mathrm{d}T - V\mathrm{d}P + \sum_i L_i \mathrm{d}x_i \ . \tag{4.39}$$

$$\bar{c}_p = x_d c_{pd} + \sum_i x_i c_{pi} + \sum_c x_c c_{pc} \ .$$

$\bar{c}_p$ is the average heat capacity (can be temperature dependence) defined as:

$$\bar{c}_p = x_d c_{pd} + \sum_i x_i c_{pi} + \sum_c x_c c_{pc} \ . \tag{4.40}$$

From the ideal gas law:

$$PV = \left(x_d + \sum_i x_i\right) RT. \tag{4.41}$$

Solve for V and substitute into equation (4.39) gives:

$$0 = \bar{c_p}\mathrm{d}T - \left(x_d + \sum_i x_i\right) RT\mathrm{d}\ln P + \sum_i L_i \mathrm{d}x_i \ . \tag{4.42}$$

Vapor pressure is proportional to molar concentration:

$$\frac{e_i}{P_d} = \frac{x_i}{x_d} = \eta_i \,. \tag{4.43}$$

η_i is the mixing ratio of the i-th species with respect to dry air. Take the logarithm and calculate differentials, then uses Clausius-Clapeyron relation $\frac{\mathrm{d}\ln e_i}{\mathrm{d}\ln T} = \frac{L_i}{RT} = \beta_i$ gives:

$$\frac{d\eta_i}{\eta_i} = \beta_i \mathrm{d}\ln T - \mathrm{d}\ln P_d \,. \tag{4.44}$$

Total pressure is equal to sum of all vapor pressures:

$$P = P_d + \sum\nolimits_i e_i = P_d \left(1 + \sum\nolimits_i \frac{e_i}{P_d}\right) = P_d \left(1 + \sum\nolimits_i \eta_i\right). \tag{4.45}$$

Take logarithm and calculate differentials:

$$\begin{aligned} \mathrm{d}\ln P &= \mathrm{d}\ln P_d + \mathrm{d}\ln\left(1 + \sum\nolimits_i \eta_i\right) \\ &= \mathrm{d}\ln P_d + \frac{\sum_i \mathrm{d}\eta_i}{1 + \sum_i \eta_i} \\ &= \mathrm{d}\ln P_d + \frac{\sum_i \eta_i(\beta_i \mathrm{d}\ln T - \mathrm{d}\ln P_d)}{1 + \sum_i \eta_i} \\ &= \frac{1}{1 + \sum_i \eta_i}\mathrm{d}\ln P_d + \frac{\sum_i \eta_i \beta_i}{1 + \sum_i \eta_i}\mathrm{d}\ln T \,. \end{aligned} \tag{4.46}$$

Solve for $\mathrm{d}\ln P_d$:

$$\mathrm{d}\ln P_d = \left(1 + \sum\nolimits_i \eta_i\right)\mathrm{d}\ln P - \sum\nolimits_i \eta_i \beta_i \,\mathrm{d}\ln T \,. \tag{4.47}$$

Use this expression to simplify equation (4.44):

$$\frac{d\eta_i}{\eta_i} = \left(\beta_i + \sum\nolimits_j \eta_j \beta_j\right) \mathrm{d}\ln T - \left(1 + \sum\nolimits_j \eta_j\right) \mathrm{d}\ln P \,. \tag{4.48}$$

To avoid confusion, we have changed the summation index to *j*. Now we have every pieces and go back to equation (4.42).

$$0 = \bar{c_p}\mathrm{d}T - \left(x_d + \sum\nolimits_i x_i\right) RT \mathrm{d}\ln P + \sum\nolimits_i L_i \mathrm{d}x_i \,,$$

$$0 = \frac{\bar{c_p}}{Rx_d}\mathrm{d}\ln T - \left(1 + \sum\nolimits_j \eta_j\right) \mathrm{d}\ln P + \sum\nolimits_i \beta_i \mathrm{d}\eta_i \,,$$

$$0 = \frac{\bar{c_p}}{Rx_d}\mathrm{d}\ln T - \left(1 + \sum\nolimits_j \eta_j\right) \mathrm{d}\ln P$$

$$+ \sum\nolimits_i \beta_i \eta_i \left(\left(\beta_i + \sum\nolimits_j \eta_j \beta_j\right) \mathrm{d}\ln T - \left(1 + \sum\nolimits_j \eta_j\right) \mathrm{d}\ln P\right),$$

$$\left(\frac{\bar{c_p}}{Rx_d} + \sum\nolimits_i \beta_i^2 \eta_i + \left(\sum\nolimits_i \eta_i \beta_i\right)^2\right) \mathrm{d}\ln T = \left(1 + \sum\nolimits_i \eta_i\right)\left(1 + \sum\nolimits_i \beta_i \eta_i\right) \mathrm{d}\ln P \,. \tag{4.49}$$

In deriving the above equation, we first divide every term by $x_{d,}$ then use equation (4.48). Finally, the lapse rate is:

$$\begin{aligned} \frac{\mathrm{d}\ln T}{\mathrm{d}\ln P} &= \left(1 + \sum\nolimits_i \eta_i\right) \frac{(1 + \sum_i \beta_i \eta_i)}{\left(\frac{\bar{c_p}}{Rx_d} + \sum_i \beta_i^2 \eta_i + (\sum_i \eta_i \beta_i)^2\right)} \\ &= \frac{1 + \sum_i \eta_i \beta_i}{\widehat{c_p}/R + \frac{\sum_i \eta_i {\beta_i}^2 + (\sum_i \eta_i \beta_i)^2}{1 + \sum_i \eta_i}} \,. \end{aligned} \tag{4.50}$$

$\widehat{c_p}$ is defined in equation (4.22).

4.7.2 Procedures to solve for $d\ln x_i / d\ln P$

Start from the partial pressure for *i*-th vapor

$$P_{v_i} = P\frac{x_{v_i}}{x_d + \sum_i x_{v_i}},$$

$$\ln P_{v_i} = \ln P + \ln x_{v_i} - \ln\left(x_d + \sum\nolimits_i x_{v_i}\right), \tag{4.51}$$

$$\mathrm{d}\ln P_{v_i} = \mathrm{d}\ln P + \frac{\mathrm{d}x_{v_i}}{x_{v_i}} - \frac{\sum_i \mathrm{d}x_i}{x_d + \sum_i x_{v_i}}.$$

Equation (4.51) is a system of *n* equations (*n* is the total number of vapors):

$$\begin{cases} \mathrm{d}\ln P_{v_1} = \mathrm{d}\ln P + \dfrac{\mathrm{d}x_{v_1}}{x_{v_1}} - \dfrac{\mathrm{d}x_{v_1} + \mathrm{d}x_{v_2} + \cdots + \mathrm{d}x_{v_n}}{x_d + x_1 + x_2 + \cdots + x_{v_n}} \\ \mathrm{d}\ln P_{v_2} = \mathrm{d}\ln P + \dfrac{\mathrm{d}x_{v_2}}{x_{v_2}} - \dfrac{\mathrm{d}x_{v_1} + \mathrm{d}x_{v_2} + \cdots + \mathrm{d}x_{v_n}}{x_d + x_1 + x_2 + \cdots + x_{v_n}} \\ \cdots \\ \cdots \\ \mathrm{d}\ln P_{v_n} = \mathrm{d}\ln P + \dfrac{\mathrm{d}x_{v_n}}{x_{v_n}} - \dfrac{\mathrm{d}x_{v_1} + \mathrm{d}x_{v_2} + \cdots + \mathrm{d}x_{v_n}}{x_d + x_1 + x_2 + \cdots + x_{v_n}} \end{cases}. \tag{4.52}$$

We need to solve $\mathrm{d}x_1, \mathrm{d}x_2, \ldots, \mathrm{d}x_n$ from equations (4.52). The solution is easy to obtain for $n = 2$, which is:

$$\begin{cases} \mathrm{d}\ln x_1 = \mathrm{d}\ln P_{v_1}/P + x_1\mathrm{d}\ln P_{v_1}/P + x_2\mathrm{d}\ln P_{v_2}/P \\ \mathrm{d}\ln x_1 = \mathrm{d}\ln P_{v_2}/P + x_1\mathrm{d}\ln P_{v_1}/P + x_2\mathrm{d}\ln P_{v_2}/P \end{cases}. \tag{4.53}$$

Then we generalize (4.53) to *n* equations:

$$\mathrm{d}\ln x_i = \mathrm{d}\ln P_{v_i} - \mathrm{d}\ln P + \sum\nolimits_j \eta_j \left(\mathrm{d}\ln P_{v_j} - \mathrm{d}\ln P\right). \tag{4.54}$$

We verify this result by back substitution into the *i*-th equation in equations (4.52). $\mathrm{d}\ln P_{v_i} - \mathrm{d}\ln P$ will cancel immediately and the rest is to verify whether

$$\sum\nolimits_j \eta_j \left(\mathrm{d}\ln P_{v_j} - \mathrm{d}\ln P\right) == \frac{\sum_i \mathrm{d}x_i}{x_d + \sum_i x_{v_i}}. \tag{4.55}$$

Divided by x_d, the right hand side becomes:

$$\frac{\sum_i \mathrm{d}x_i}{x_d + \sum_i x_{v_i}} = \frac{\sum_i \mathrm{d}\eta_i}{1 + \sum_i \eta_i}. \tag{4.56}$$

Divided by P_d, the left hand side becomes:

$$\sum_i \eta_i \left(\mathrm{d}\ln\frac{P_{v_i}}{P}\right) = \sum_i \eta_i \left(\mathrm{d}\ln\frac{\eta_i}{1+\sum_j \eta_j}\right)$$

$$= \sum_i \eta_i \left(\frac{\frac{\mathrm{d}\eta_i\left(1+\sum_j \eta_j\right) - \eta_i \sum_j \mathrm{d}\eta_j}{\left(1+\sum_j \eta_j\right)^2}}{\frac{\eta_i}{1+\sum_j \eta_j}}\right)$$

$$= \frac{\sum_i \mathrm{d}\eta_i + \sum_i \mathrm{d}\eta_i \sum_j \eta_j - \sum_i \eta_i \sum_j \mathrm{d}\eta_j}{1+\sum_j \eta_j}$$

$$= \frac{\sum_i \mathrm{d}\eta_i}{1+\sum_i \eta_i} \tag{4.57}$$

Therefore, we proved that equation (4.55) is correct.

Bibliography

Achterberg, R. K., et al., 2014. Changes to Saturn's Zonal-mean Tropospheric Thermal Structure after the 2010-2011 Northern Hemisphere Storm. The Astrophysical Journal. 786**,** 92-100.

Achterberg, R. K., Ingersoll, A. P., 1989. A Normal-Mode Approach to Jovian Atmospheric Dynamics. Journal of the Atmospheric Sciences. 46**,** 2448-2462.

Allen, M., Yung, Y. L., Waters, J. W., 1981. Vertical transport and photochemistry in the terrestrial mesosphere and lower thermosphere (50-120 km). Journal of Geophysical Research. 86**,** 3617-3627.

Asplund, M., Grevesse, N., Sauval, A. J., Scott, P., 2009. The Chemical Composition of the Sun. Annual Review of Astronomy and Astrophysics, Vol 47. 47**,** 481-522.

Atreya, S. K., 1987. Atmospheres and Ionospheres of the Outer Planets and Their Satellites. Springer, New York-Berlin.

Atreya, S. K., Romani, P. N., 1985. Photochemistry and clouds of Jupiter, Saturn and Uranus. Recent advances in planetary meteorology.

Banfield, D., et al., 1998. Jupiter's cloud structure from Galileo imaging data. Icarus. 135**,** 230-250.

Barcilon, A., Gierasch, P., 1970. A Moist, Hadley Cell Model for Jupiters Cloud Bands. Journal of the Atmospheric Sciences. 27**,** 550-&.

Bjoraker, G. L., Wong, M. H., de Pater, I., Adamkovics, M., 2015. Jupiter's Deep Cloud Structure Revealed Using Keck Observations of Spectrally Resolved Line Shapes. Astrophysical Journal. 810.

Charney, J. G., Eliassen, A., 1964. On the Growth of the Hurricane Depression. Journal of the Atmospheric Sciences. 21**,** 68-75.

Conrath, B. J., Gierasch, P. J., 1984. Global Variation of the Para Hydrogen Fraction in Jupiters Atmosphere and Implications for Dynamics on the Outer Planets. Icarus. 57**,** 184-204.

Coustenis, A., et al., 2007. The composition of Titan's stratosphere from Cassini/CIRS mid-infrared spectra. Icarus. 189**,** 35-62.

Coustenis, A., Bezard, B., Gautier, D., 1989. Titan's atmosphere from Voyager infrared observations .1. the gas-composition of Titan's equatorial region. Icarus. 80**,** 54-76.

Coustenis, A., et al., 2003. Titan's atmosphere from ISO mid-infrared spectroscopy. Icarus. 161**,** 383-403.

Crespin, A., et al., 2008. Diagnostics of Titan's stratospheric dynamics using Cassini/CIRS data and the 2-dimensional IPSL circulation model. Icarus. 197**,** 556-571.

Cui, J., Yelle, R., Volk, K., 2008. Distribution and escape of molecular hydrogen in Titan's thermosphere and exosphere. Journal of Geophysical Research. 113**,** E10004.

de Pater, I., Dunn, D., Romani, P., Zahnle, K., 2001. Reconciling Galileo probe data and ground-based radio observations of ammonia on Jupiter. Icarus. 149**,** 66-78.

de Pater, I., Massie, S. T., 1985. Models of the Millimeter-Centimeter Spectra of the Giant Planets. Icarus. 62**,** 143-171.

Dowling, T. E., Ingersoll, A. P., 1989. Jupiters Great Red Spot as a Shallow-Water System. Journal of the Atmospheric Sciences. 46**,** 3256-3278.

Dyudina, U. A., et al., 2007. Lightning storms on Saturn observed by Cassini ISS and RPWS during 2004-2006. Icarus. 190**,** 545-555.

Emanuel, K. A., 1994. Atmospheric convection. Oxford University Press, New York.

Emanuel, K. A., Neelin, J. D., Bretherton, C. S., 1994. On Large-Scale Circulations in Convecting Atmospheres. Quarterly Journal of the Royal Meteorological Society. 120**,** 1111-1143.

Fischer, G., et al., 2011. A giant thunderstorm on Saturn. Nature. 475**,** 75-77.

Fletcher, L. N., et al., 2011. Thermal Structure and Dynamics of Saturn's Northern Springtime Disturbance. Science. 332**,** 1413-1417.

Fletcher, L. N., Orton, G. S., Teanby, N. A., Irwin, P. G. J., 2009a. Phosphine on Jupiter and Saturn from Cassini/CIRS. Icarus. 202**,** 543-564.

Fletcher, L. N., Orton, G. S., Teanby, N. A., Irwin, P. G. J., Bjoraker, G. L., 2009b. Methane and its isotopologues on Saturn from Cassini/CIRS observations. Icarus. 199**,** 351-367.

Fletcher, L. N., et al., 2012. Sub-millimetre spectroscopy of Saturn's trace gases from Herschel/SPIRE. Astronomy & Astrophysics. 539**,** A44.

Friedson, A. J., 2005. Water, ammonia, and H2S mixing ratios in Jupiter's five-micron hot spots: A dynamical model. Icarus. 177**,** 1-17.

Fulchignoni, M., et al., 2005. In situ measurements of the physical characteristics of Titan's environment. Nature. 438**,** 785-791.

Galland, N., Caralp, F., Hannachi, Y., Bergeat, A., Loison, J.-C., 2003. Experimental and theoretical studies of the methylidyne CH (X2π) radical reaction with ethane (C2H6): Overall rate constant and product channels. Journal of Physical Chemistry A. 107**,** 5419-5426 %@ 1089-5639.

Giles, R. S., Fletcher, L. N., Irwin, P. G. J., 2015. Cloud structure and composition of Jupiter's troposphere from 5-mu m Cassini VIMS spectroscopy. Icarus. 257**,** 457-470.

Goodman, J., Weare, J., 2010. Ensemble Samplers with Affine Invariance. Communications in Applied Mathematics and Computational Science. 5**,** 65-80.

Goulay, F., et al., 2009. Cyclic Versus Linear Isomers Produced by Reaction of the Methylidyne Radical (CH) with Small Unsaturated Hydrocarbons. Journal of the American Chemical Society. 131**,** 993-1005.

Guillot, T., 1995. Condensation of Methane, Ammonia, and Water and the Inhibition of Convection in Giant Planets. Science. 269**,** 1697-1699.

Guillot, T., Gautier, D., Chabrier, G., Mosser, B., 1994. Are the Giant Planets Fully Convective. Icarus. 112**,** 337-353.

Hammel, H. B., et al., 1995. Hst Imaging of Atmospheric Phenomena Created by the Impact of Comet Shoemaker-Levy-9. Science. 267**,** 1288-1296.

Hebrard, E., Dobrijevic, M., Loison, J. C., Bergeat, A., Hickson, K. M., Caralp, F., 2013. Photochemistry of C3Hp hydrocarbons in Titan's stratosphere revisited. Astronomy & Astrophysics. 552.

Helled, R., Lunine, J., 2014. Measuring Jupiter's water abundance by Juno: the link between interior and formation models. Monthly Notices of the Royal Astronomical Society. 441**,** 2273-2279.

Hörst, S. M., Vuitton, V., Yelle, R. V., 2008. Origin of oxygen species in Titan's atmosphere. J. Geophys. Res. 113**,** E10006.

Hueso, R., Sanchez-Lavega, A., 2004. A three-dimensional model of moist convection for the giant planets II: Saturn's water and ammonia moist convective storms. Icarus. 172**,** 255-271.

Ingersoll, A. P., Cuong, P. G., 1981. Numerical-Model of Long-Lived Jovian Vortices. Journal of the Atmospheric Sciences. 38**,** 2067-2076.

Ingersoll, A. P., Kanamori, H., 1995. Waves from the Collisions of Comet Shoemaker-Levy-9 with Jupiter. Nature. 374**,** 706-708.

Ingersoll, A. P., Kanamori, H., Dowling, T. E., 1994. Atmospheric Gravity-Waves from the Impact of Comet Shoemaker-Levy-9 with Jupiter. Geophysical Research Letters. 21**,** 1083-1086.

Janssen, M. A., et al., 2005. Microwave remote sensing of Jupiter's atmosphere from an orbiting spacecraft. Icarus. 173**,** 447-453.

Janssen, M. A., et al., 2013. Saturn's thermal emission at 2.2-cm wavelength as imaged by the Cassini RADAR radiometer. Icarus. 226**,** 522-535.

Kammer, J. A., Shemansky, D. E., Zhang, X., Yung, Y. L., 2011. Probing Titan's upper atmosphere: observations from Cassini/UVIS. EPSC-DPS Joint Meeting. 347.

Kammer, J. A., Shemansky, D. E., Zhang, X., Yung, Y. L., 2013. Composition of Titan's upper atmosphere from Cassini UVIS EUV stellar occultations. Planetary and Space Science. 88**,** 86-92.

Koskinen, T. T., et al., 2011. The mesosphere and thermosphere of Titan revealed by Cassini/UVIS stellar occultations. Icarus. 216**,** 507-534.

Krasnopolsky, V. A., 2009. A photochemical model of Titan's atmosphere and ionosphere. Icarus. 201**,** 226-256.

Krasnopolsky, V. A., 2010. The photochemical model of Titan's atmosphere and ionosphere: A version without hydrodynamic escape. Planetary and Space Science. 58**,** 1507-1515.

Krasnopolsky, V. A., 2014. Chemical composition of Titan's atmosphere and ionosphere: Observations and the photochemical model. Icarus. 236**,** 83-91.

Lara, L. M., Lellouch, E., Lopez-Moreno, J. J., Rodrigo, R., 1996. Vertical distribution of Titan's atmospheric neutral constituents. Journal of Geophysical Research-Planets. 101**,** 23261-23283.

Laraia, A. L., Ingersoll, A. P., Janssen, M. A., Gulkis, S., Oyafuso, F., Allison, M., 2013. Analysis of Saturn's thermal emission at 2.2-cm wavelength: Spatial distribution of ammonia vapor. Icarus. 226**,** 641-654.

Lavvas, P., Sander, M., Kraft, M., Imanaka, H., 2011. Surface Chemistry and Particle Shape: Processes for the Evolution of Aerosols in Titan's Atmosphere. Astrophysical Journal. 728**,** 80.

Lavvas, P., Yelle, R. V., Griffith, C. A., 2010. Titan's vertical aerosol structure at the Huygens landing site: Constraints on particle size, density, charge, and refractive index. Icarus. 210**,** 832-842.

Lavvas, P. P., Coustenis, A., Vardavas, I. M., 2008a. Coupling photochemistry with haze formation in Titan's atmosphere, part I: Model description. Planetary and Space Science. 56**,** 27-66.

Lavvas, P. P., Coustenis, A., Vardavas, I. M., 2008b. Coupling photochemistry with haze formation in Titan's atmosphere, Part II: Results and validation with Cassini/Huygens data. Planetary and Space Science. 56**,** 67-99.

Lebonnois, S., Toublanc, D., Hourdin, F., Rannou, P., 2001. Seasonal variations of Titan's atmospheric composition. Icarus. 152**,** 384-406.

LeVeque, R. J., 2007. Finite difference methods for ordinary and partial differential equations : steady-state and time-dependent problems. Society for Industrial and Applied Mathematics, Philadelphia, PA.

Lewis, J. S., 1969. The clouds of Jupiter and the NH 3—H 2 O and NH 3—H 2 S systems. Icarus. 10**,** 365-378.

Li, C., Ingersoll, A. P., 2015. Moist convection in hydrogen atmospheres and the frequency of Saturn's giant storms. Nature Geoscience. 8**,** 398-403.

Li, C., Zhang, X., Kammer, J. A., Liang, M.-C., Shia, R.-L., Yung, Y. L., 2014. A non-monotonic eddy diffusivity profile of Titan's atmosphere revealed by Cassini observations. Planetary and Space Science. 104, Part A**,** 48-58.

Li, L. M., Ingersoll, A. P., Huang, X. L., 2006. Interaction of moist convection with zonal jets on Jupiter and Saturn. Icarus. 180**,** 113-123.

Liang, M. C., Yung, Y. L., Shemansky, D. E., 2007. Photolytically generated aerosols in the mesosphere and thermosphere of Titan. Astrophysical Journal. 661**,** L199-L202.

Lightfoot, P. D., Pilling, M. J., 1987. Temperature and Pressure-Dependence of the Rate-Constant for the Addition of H to C2h4. Journal of Physical Chemistry. 91**,** 3373-3379.

Lindal, G. F., Sweetnam, D. N., Eshleman, V. R., 1985. The Atmosphere of Saturn - an Analysis of the Voyager Radio Occultation Measurements. Astronomical Journal. 90**,** 1136-1146.

Lindzen, R. S., 1981. Turbulence and stress owing to gravity wave and tidal breakdown. Journal of Geophysical Research. 86**,** 9707-9714.

Line, M. R., et al., 2013. A Systematic Retrieval Analysis of Secondary Eclipse Spectra. I. A Comparison of Atmospheric Retrieval Techniques. Astrophysical Journal. 775.

Loison, J. C., et al., 2015. The neutral photochemistry of nitriles, amines and imines in the atmosphere of Titan. Icarus. 247**,** 218-247.

Magalhaes, J. A., Seiff, A., Young, R. E., 2002. The stratification of Jupiter's troposphere at the Galileo probe entry site. Icarus. 158**,** 410-433.

Magee, B. A., Waite, J. H., Mandt, K. E., Westlake, J., Bell, J., Gell, D. A., 2009. INMS-derived composition of Titan's upper atmosphere: Analysis methods and model comparison. Planetary and Space Science. 57**,** 1895-1916.

Magnusson, J. P., 1907. Equilibrium between ammonia and hydrogen sulphide. Journal of Physical Chemistry. 11**,** 21-46.

Massie, S. T., Hunten, D. M., 1982. Conversion of Para-Hydrogen and Ortho-Hydrogen in the Jovian Planets. Icarus. 49**,** 213-226.

Michelangeli, D. V., Allen, M., Yung, Y. L., 1989. El Chichón volcanic aerosols: Impact of radiative, thermal, and chemical perturbations. Journal of Geophysical Research: Atmospheres (1984-2012). 94**,** 18429-18443.

Moré, J., 1978. The Levenberg-Marquardt algorithm: implementation and theory. Numerical analysis. 105-116.

Moses, J., Fouchet, T., Bézard, B., Gladstone, G., Lellouch, E., Feuchtgruber, H., 2005a. Photochemistry and diffusion in Jupiter's stratosphere: constraints from ISO

observations and comparisons with other giant planets. Journal of Geophysical Research. 110**,** E08001.

Moses, J. I., Fouchet, T., Bezard, B., Gladstone, G. R., Lellouch, E., Feuchtgruber, H., 2005b. Photochemistry and diffusion in Jupiter's stratosphere: Constraints from ISO observations and comparisons with other giant planets. Journal of Geophysical Research-Planets. 110**,** E08001.

Moses, J. I., Greathouse, T. K., 2005. Latitudinal and seasonal models of stratospheric photochemistry on Saturn: Comparison with infrared data from IRTF/TEXES. Journal of Geophysical Research-Planets. 110.

Navarro-González, R., Ramírez, S. I., 1997. Corona discharge of Titan's troposphere. Advances in Space Research. 19**,** 1121-1133 %@ 0273-1177.

Niemann, H. B., et al., 1996. The Galileo probe mass spectrometer: Composition of Jupiter's atmosphere. Science. 272**,** 846-849.

Nixon, C. A., et al., 2010. Upper limits for undetected trace species in the stratosphere of Titan. Faraday discussions. 147**,** 65-81.

Nixon, C. A., et al., 2013. Detection of Propene in Titan's Stratosphere. Astrophysical Journal Letters. 776**,** L14.

Orton, G. S., Ingersoll, A. P., 1980. Saturn's Atmospheric Temperature Structure and Heat Budget. Journal of Geophysical Research-Space Physics. 85**,** 5871-5881.

Perman, E. P., 1903. Vapour pressure of aqueous ammonia solution Part II. Journal of the Chemical Society. 83**,** 1168-1184.

Prinn, R. G., Barshay, S. S., 1977. Carbon-Monoxide on Jupiter and Implications for Atmospheric Convection. Science. 198**,** 1031-1034.

Roe, H. G., Greathouse, T., Tokunaga, A., 2011. Update on the TEXES Titan Mid-Infrared Spectral Survey. EPSC-DPS Joint Meeting. 6.

Roe, P. L., 1997. Approximate Riemann solvers, parameter vectors, and difference schemes (Reprinted from the Journal of Computational Physics, vol 43, pg 357-372, 1981). Journal of Computational Physics. 135**,** 250-258.

Rogers, D. W., Mclafferty, F., 1995. G2 Ab-Initio Calculations of the Enthalpies of Formation of C-3 Hydrocarbons. Journal of Physical Chemistry. 99**,** 1375-1376.

Roos-Serote, M., Atreya, S. K., Wong, M. K., Drossart, P., 2004. On the water abundance in the atmosphere of Jupiter. Planetary and Space Science. 52**,** 397-414.

Sanchez-Lavega, A., 1994. Saturn's Great White Spots. Chaos. 4**,** 341-353.

Sanchez-Lavega, A., Battaner, E., 1987. The Nature of Saturns Atmospheric Great White Spots. Astronomy & Astrophysics. 185**,** 315-326.

Sanchez-Lavega, A., et al., 2011. Deep winds beneath Saturn's upper clouds from a seasonal long-lived planetary-scale storm. Nature. 475**,** 71-74.

Sayanagi, K. M., et al., 2013. Dynamics of Saturn's great storm of 2010-2011 from Cassini ISS and RPWS. Icarus. 223**,** 460-478.

Seiff, A., et al., 1998. Thermal structure of Jupiter's atmosphere near the edge of a 5-mu m hot spot in the north equatorial belt. Journal of Geophysical Research-Planets. 103**,** 22857-22889.

Sekine, Y., et al., 2008a. The role of organic haze in Titan's atmospheric chemistry: I. Laboratory investigation on heterogeneous reaction of atomic hydrogen with Titan tholin. Icarus. 194**,** 186-200.

Sekine, Y., et al., 2008b. The role of organic haze in Titan's atmospheric chemistry I. Laboratory investigation on heterogeneous reaction of atomic hydrogen with Titan tholin. Icarus. 194**,** 186-200.

Sekine, Y., et al., 2008c. The role of organic haze in Titan's atmospheric chemistry: II. Effect of heterogeneous reaction to the hydrogen budget and chemical composition of the atmosphere. Icarus. 194**,** 201-211.

Sekine, Y., et al., 2008d. The role of organic haze in Titan's atmospheric chemistry II. Effect of heterogeneous reaction to the hydrogen budget and chemical composition of the atmosphere. Icarus. 194**,** 201-211.

Showman, A. P., 2007. Numerical simulations of forced shallow-water turbulence: Effects of moist convection on the large-scale circulation of Jupiter and Saturn. Journal of the Atmospheric Sciences. 64**,** 3132-3157.

Showman, A. P., Dowling, T. E., 2000. Nonlinear simulations of Jupiter's 5-micron hot spots. Science. 289**,** 1737-1740.

Showman, A. P., Ingersoll, A. P., 1998. Interpretation of Galileo probe data and implications for Jupiter's dry downdrafts. Icarus. 132**,** 205-220.

Shu, C. W., 1988. Total-Variation-Diminishing Time Discretizations. Siam Journal on Scientific and Statistical Computing. 9**,** 1073-1084.

Shu, C. W., Osher, S., 1989. Efficient Implementation of Essentially Non-Oscillatory Shock-Capturing Schemes. Journal of Computational Physics. 83**,** 32-78.

Stoker, C. R., 1986. Moist Convection - a Mechanism for Producing the Vertical Structure of the Jovian Equatorial Plumes. Icarus. 67**,** 106-125.

Strobel, D. F., 1974. Photochemistry of hydrocarbons in atmosphere of Titan. Icarus. 21**,** 466-470.

Stull, R. B., 1988. An Introduction to Boundary Layer Meteorology. Kluwer Academic.

Sugiyama, K., et al., 2011. Intermittent cumulonimbus activity breaking the three-layer cloud structure of Jupiter. Geophysical Research Letters. 38**,** 201-206.

Sugiyama, K., Nakajima, K., Odaka, M., Kuramoto, K., Hayashi, Y. Y., 2014. Numerical simulations of Jupiter's moist convection layer: Structure and dynamics in statistically steady states (vol 229, pg 71, 2014). Icarus. 231**,** 407-408.

Tanguy, L., et al., 1990. Stratospheric profile of HCN on Titan from millimeter observations. Icarus. 85**,** 43-57.

Taylor, G., 1931. Effect of variation in density on the stability of superposed streams of fluid. Proceedings of the Royal Society of London. Series A. 132**,** 499-523.

Teanby, N., et al., 2008. Titan's winter polar vortex structure revealed by chemical tracers. Journal of Geophysical Research. 113**,** E12003.

Toublanc, D., Parisot, J., Brillet, J., Gautier, D., Raulin, F., McKay, C., 1995. Photochemical modeling of Titan's atmosphere. Icarus. 113**,** 2-26.

Vinatier, S., et al., 2010a. Analysis of Cassini/CIRS limb spectra of Titan acquired during the nominal mission II: Aerosol extinction profiles in the 600-1420 cm(-1) spectral range. Icarus. 210**,** 852-866.

Vinatier, S., et al., 2007. Vertical abundance profiles of hydrocarbons in Titan's atmosphere at 15 S and 80 N retrieved from Cassini/CIRS spectra. Icarus. 188**,** 120-138.

Vinatier, S., et al., 2010b. Analysis of Cassini/CIRS limb spectra of Titan acquired during the nominal mission I. Hydrocarbons, nitriles and CO2 vertical mixing ratio profiles. Icarus. 205**,** 559-570.

Visscher, C., Moses, J. I., Saslow, S. A., 2010. The deep water abundance on Jupiter: New constraints from thermochemical kinetics and diffusion modeling. Icarus. 209**,** 602-615.

Vuitton, V., Yelle, R., Cui, J., 2008. Formation and distribution of benzene on Titan. Journal of Geophysical Research. 113**,** E05007.

Vuitton, V., Yelle, R., Lavvas, P., Klippenstein, S., 2012a. Rapid Association Reactions at Low Pressure: Impact on the Formation of Hydrocarbons on Titan. The Astrophysical Journal. 744**,** 11.

Vuitton, V., Yelle, R. V., Lavvas, P., Klippenstein, S. J., 2012b. Rapid Association Reactions at Low Pressure: Impact on the Formation of Hydrocarbons on Titan. Astrophysical Journal. 744**,** 11.

Vuitton, V., Yelle, R. V., McEwan, M. J., 2007. Ion chemistry and N-containing molecules in Titan's upper atmosphere. Icarus. 191**,** 722-742.

Waite Jr, J. H., et al., 2005. Ion neutral mass spectrometer results from the first flyby of Titan. Science. 308**,** 982-986.

Walterscheid, R. L., Brinkman, D. G., Schubert, G., 2000. Wave disturbances from the comet SL-9 impacts into Jupiter's atmosphere. Icarus. 145**,** 140-146.

Wang, D., Gierasch, P. J., Lunine, J. I., Mousis, O., 2015. New insights on Jupiter’s deep water abundance from disequilibrium species. Icarus. 250**,** 154-164.

Weidenschilling, S. J., Lewis, J. S., 1973. Atmospheric and Cloud Structures of Jovian Planets. Icarus. 20**,** 465-476.

Westlake, J., et al., 2011a. Titan's thermospheric response to various plasma environments. Journal of Geophysical Research: Space Physics (1978-2012). 116.

Westlake, J. H., et al., 2011b. Titan's thermospheric response to various plasma environments. Journal of Geophysical Research-Space Physics. 116**,** A03318.

Wilson, E. H., Atreya, S. K., 2004. Current state of modeling the photochemistry of Titan's mutually dependent atmosphere and ionosphere. Journal of Geophysical Research-Planets. 109**,** E06002.

Wilson, E. H., Atreya, S. K., 2009. Titan's Carbon Budget and the Case of the Missing Ethane. Journal of Physical Chemistry A. 113**,** 11221-11226.

Wong, M. H., Atreya, S. K., Kuhn, W. R., Romani, P. N., Mihalka, K. M., 2015. Fresh clouds: A parameterized updraft method for calculating cloud densities in one-dimensional models. Icarus. 245**,** 273-281.

Wong, M. H., Mahaffy, P. R., Atreya, S. K., Niemann, H. B., Owen, T. C., 2004. Updated Galileo probe mass spectrometer measurements of carbon, oxygen, nitrogen, and sulfur on Jupiter. Icarus. 171**,** 153-170.

Wyngaard, J. C., 1992. Atmospheric turbulence. Annual Review of Fluid Mechanics. 24**,** 205-233.

Yelle, R., Cui, J., Müller-Wodarg, I., 2008a. Methane escape from Titan's atmosphere. Journal of Geophysical Research. 113**,** E10003.

Yelle, R. V., Cui, J., Muller-Wodarg, I. C. F., 2008b. Methane escape from Titan's atmosphere. Journal of Geophysical Research-Planets. 113**,** E10003.

Yung, Y. L., 1987. An update of nitrile photochemistry on Titan. Icarus. 72**,** 468-472.

Yung, Y. L., Allen, M., Pinto, J. P., 1984. Photochemistry of the Atmosphere of Titan - Comparison between Model and Observations. Astrophysical Journal Supplement Series. 55**,** 465-506.

Zhang, X., Ajello, J. M., Yung, Y. L., 2010. Atomic carbon in the upper atmosphere of Titan. The Astrophysical Journal Letters. 708**,** L18.